Master's thesis

NTNU
Norwegian University of Science and Technology
Faculty of Information Technology and Electrical Engineering
Department of Engineering Cybernetics

Emma Horn Buøen
Sara Lund Ludvigsen

The Augmented Human

Development of BCI for RGB colour-based automation

Master's thesis in Cybernetics and Robotics
Supervisor: Marta Molinas
Co-supervisor: Andres Soler
June 2021

NTNU
Norwegian University of
Science and Technology

Emma Horn Buøen
Sara Lund Ludvigsen

The Augmented Human

Development of BCI for RGB colour-based automation

Master's thesis in Cybernetics and Robotics
Supervisor: Marta Molinas
Co-supervisor: Andres Soler
June 2021

Norwegian University of Science and Technology
Faculty of Information Technology and Electrical Engineering
Department of Engineering Cybernetics

NTNU
Norwegian University of
Science and Technology

Abstract

This thesis examines the possibility of classifying EEG signals produced by visual stimuli to red, green and blue (RGB) colours. A dataset of 31 subjects was analysed. The dataset was recorded at the NeuroImaging facilities at Aalto University in Helsinki by Andres Soler. It consists of EEG recordings with 64 channels where the participants were exposed to the RGB colours stimuli during one or two sessions of approximately 22 minutes each. Two different methods for classification have been explored. The first was based on EEG source reconstruction identifying the sources of the signals. When localised, the signals emitted from areas in the visual cortex were extracted. A Morlet wavelet transform was performed on the extracted signals, and the transformed signals were used as a base for further feature extraction. This method reached an average classification accuracy of 50% over all subjects, with 88% as the highest accuracy for an individual subject.

The second method used the EEG signals recorded from 8 channels located at occipital-parietal regions. A Morlet wavelet transform was performed on these signals and created a 3rd-order tensor for each epoch. The tensors were reshaped into a 2-dimensional matrix form for each epoch and then transformed into a covariance matrix. The covariance matrices were used as input to Riemannian based classifiers, classifying with an average accuracy of 75% over all subjects. 35% of the subjects and sessions used for RGB classification obtained an accuracy above 80% with the second method. The highest accuracy obtained for an individual subject was 93%. The lowest accuracy obtained was 54%. Hence, the EEG signal model based on the second methods was above the chance level for all subject, the chance level for three classes being 33%.

A cross-session experiment was conducted in order to investigate the robustness of transfer learning for Riemannian based classifiers. The result was an average of 4,6% variation in accuracy between the source set and target set for 86% of the subjects tested. This result supports the hypothesis that Riemannian classifiers are robust for transfer learning.

The obtained accuracy for RGB classification from EEG signals in this thesis surpasses all previous attempts. Average accuracy of 72% with the best subject-specific accuracy of 81% was the best result obtained previously to this thesis.

Abstrakt

Denne oppgaven undersøker muligheten for å klassifisere EEG signaler produsert av visuell eksponering av fargene rød, grønn og blå (RGB). Et datasett bestående av 31 subjekter ble analysert. Datasettet ble laget ved NeuroImaging anlegget ved Aalto Universitet i Helsinki av Andres Soler. Det består av EEG målinger med 64 elektroder der deltageren ble eksponert for RGB farger gjennom en eller to økter. Hver økt varte i omtrent 22 minutter. To forskjellige metoder for klassifisering har blitt utforsket. Den første identifiserer kildene til signalene. Når disse var lokalisert ble signaler fra den visuelle hjernebarken hentet ut. En Morlet bølgetransformasjon ble utført på de uthentede signalene, og de transformerte signalene var base for videre ekstraksjon av signalenes egenskaper. Denne metoden nådde en gjennomsnittlig klassifiseringsnøyaktighet på 50% over alle subjekter, med 88% som høyeste nøyaktighet for et individuelt subjekt.

Den andre metoden brukte EEG signalene registrert av 8 elektroder lokalisert ved bakhodelappen og isselappen. En Morlet bølgetransformasjon ble utført på disse signalene og lagde en 3.-ordre tensor for hver epoke. Tensorene ble omformet til en 2-dimensjonal matriseform for hver epoke, og videre transformert til en kovariansmatrise. Kovariansmatrisen ble brukt som input til Riemann-baserte klassifikatorer som kategoriserte signalene med en gjennomsnittlig nøyaktighet på 75% over alle subjekter. 35% av subjekter og økter brukt til RGB-klassifisering klassifiserte med en nøyaktighet på over 80% med den andre metoden. Høyeste nøyaktighet oppnådd for et individuelt subjekt var 93%. Laveste nøyaktighet oppnådd var 54%. Det viser at EEG signalmodellen basert på den andre metoden var over sjansenivå for alle subjekter, siden sjansenivå er 33% for tre klasser.

Et eksperiment på tvers av økter ble gjennomført. Hensikten var å undersøke robustheten til overført læring for Riemann-baserte klassifikatorer. Resultatet viste et gjennomsnitt på 4,6% variasjon i nøyaktighet mellom økten som ble brukt til trening og økten som ble brukt til predikering for 86% of subjektene testet. Dette resultatet støtter opp under hypotesen om at Riemann-klassifikatorer er robuste for overførbar læring.

Den oppnådde nøyaktigheten for RGB-klassifikasjon fra EEG-signaler i denne oppgaven overgår alle tidligere forsøk. Gjennomsnittlig nøyaktighet på 72%, med beste subjektspesifikke nøyaktighet på 81%, var det beste resultatet som var oppnådd før denne oppgaven.

Acknowledgements

Throughout the research, implementation and writing of this thesis, we have received invaluable assistance. First, we want to thank our supervisor Professor Marta Molinas for proposing this project and thus introducing us to the field of brain-computer interfaces. We are truly grateful for the support and guidance of Andres Soler. He took the time to introduce us to EEG signal processing thoroughly and provided us with a dataset and relevant literature. He has always made himself available for our questions, and we are incredibly grateful for his patience, support and advice. This thesis could not have been written without him.

Sara would like to acknowledge her family for their support, especially her grandparents, for never failing to assist her with food, transport and company whenever needed. Additionally, she would like to acknowledge her roommates for keeping her spirits high whilst writing a thesis during a pandemic. Finally, she must express her gratitude towards her co-author for an excellent partnership and continuous motivation.

Emma would like to thank her parents and sister for their support during this project. She also wants to thank her grandmother for her fascination with the topic and her words of encouragement. Last but not least, she wishes to express her gratitude to her co-author, Sara, who has kept her motivated all year whilst being an excellent partner.

Furthermore, we both want to express our gratitude to the faculty of Engineering Cybernetics for providing us with the tools and resources needed throughout our studies and to complete this Master's degree.

Figure 1: The two authors

Preface

This is a Master Thesis completed during the spring semester of 2021. It concludes a Master of Technology at the Department of Engineering Cybernetics, Norwegian University of Science and Technology (NTNU) for both authors. The project was proposed and supervised by Professor Marta Molinas and Andres Soler. The latter was also responsible for introducing the tools for source reconstruction and creating the dataset used throughout the thesis.

Parts of chapter 2 and section 3.5 are updated versions of our Semester project "Online Classification of EEG Signals from Imagery Movement" (NTNU, 2020)[1]. The combination of features described in section 3.4.2 and section 3.4.3 was a consequence of performing the analysis in section 3.3. It obtained the highest accuracy when classifying and is our original work. Choice of energy, fractal and statistical features were based on work by Sara Åsly in [2]. They were applied in the model with the best performance on source reconstructed signals. All results obtained in chapter 4 are our original work.

The RGB classification and transfer learning results have been submitted to the 14th International Conference on Brain Informatics (BI2021) as S. Ludvigsen, E. Buøen, A. Soler and M. Molinas, "Searching for unique neural descriptors of primary colours in EEG signals: a classification study", and we hope to see it published during the summer. This paper can be found in appendix C.

We had no prior knowledge about EEG signals or the brain's workings and the visual system before starting this project. Hopefully, this master thesis conveys the experience and knowledge we have gained this year.

Trondheim, June 2021
Emma Horn Buøen & Sara Lund Ludvigsen

List of Tables

List of Figures

Contents

Chapter 1

Introduction

The ability to see colours is an important part of the sensory system. In the animal kingdom, distinguishing colours is critical when identifying food, predators and mates, three of the most important aspects of animal life. In humans with normal colour vision, the visual system converts visual stimuli into chemical and electrical stimuli. The human brain then processes these stimuli. [3]

1.1 Background

The brain activity caused by exposure to a visual cue can be recorded as electrical signals. Electroencephalography (EEG) is a method for measuring these signals. EEG recordings can be either invasive or non-invasive. Invasive EEG signals are recorded with surgically implanted electrodes in the head, while non-invasive signals are made with sensors placed on the scalp. In a medical setting, EEG recordings can be used to diagnose a condition and monitor the brain's health. The signals from an EEG recording can, for example, be used to investigate epilepsy or locating damaged areas after a head injury. Non-invasive EEG is a favoured method for analysing the state of the brain because it is inexpensive and has a high temporal resolution. There is a lower risk associated with non-invasive methods than invasive methods. A problem with non-invasive EEG recordings is that it is difficult to know the exact location of the electrical source because the signal has to be measured at the scalp. Additionally, due to volume conduction the signals registered by the electrodes are the mix of multiple source activities. [4]

A brain-computer interface (BCI) allows a user to control a computer with its brain. Due to advances in the medical field, more patients survive severe injuries to the central nervous system. Some of these patients have an active mind but a paralysed body. In other words, they are suffering from locked-in syndrome [5]. The goal of a BCI system is to allow the user to communicate

with its surroundings, through a computer, without using its muscles [6]. Before controlling a computer with signals from the brain, the brain signals must be recorded and analysed. Furthermore, the features that best represent the action performed (e.g. seeing the colour red or imagining raising the left hand) needs to be extracted from the signal. With these features, an EEG signal model can be trained to classify the actions. This classification model can then be used to control the computer based on the action performed.

A BCI system can be controlled with several neural actions. Extensive research on the classification of imagined movements and visual stimuli is available [7]. However, less research exists on the classification of RGB colours from EEG signals. If it is possible to discriminate the primary colours based on brain signals, these neural actions can be used as input in a BCI system. An advantage of using colours cues and not imaginary movement as input is that the processing in the brain is quicker when processing colours. The ability to imagine movement is a skill that not everyone has, and it requires concentration and training. Colours are already a part of our communication system, and several actions are associated with colours. For example, the colours of the traffic lights signals stop, go and be careful. There are numerous uses for a BCI system that uses RGB colours as input. For locked-in patients, it can increase independence, for example, by opening a door when the patient looks at a green sign and closing it when looking at a red one. It can also switch lights on and off. The ability to perform these simple actions will lead to more control over the patients' environment and simplify daily operations.

Problem Formulation

The purpose of this thesis is to assess the feasibility of using the EEG response from exposure to the primary colours as input in a brain-computer interface. In order to do so, an EEG signal model that can distinguish between colours needs to be built using machine learning algorithms. Furthermore, for the model to be applicable in a BCI system, it needs to classify online. Therefore, there is a focus on the complexity of the EEG signal model. Moreover, transfer learning across sessions needs to be explored and evaluated.

Related Work

[7] **F Lotte et al. "A review of classification algorithms for EEG-based brain–computer interfaces: a 10 year update". In: *Journal of Neural Engineering* 15.3 (Apr. 2018), p. 031005. DOI:** 10.1088/1741-2552/aab2f2**. URL:** https://doi.org/10.1088%5C%2F1741-2552%5C%2Faab2f2 has provided valuable information and sources to this thesis. It describes how state-of-the-art EEG-based BCIs have changed from 2007 to 2017. The main results of this review were as follows:

> *" [...] Transfer learning can also prove useful although the benefits of transfer learning remain unpredictable. Riemannian geometry-based methods have reached state-of-the-art performances on multiple BCI problems and deserve to be explored more thoroughly, along with tensor-based methods. Shrinkage linear discriminant analysis and random forests also appear particularly useful for small training samples settings. On the other hand, deep learning methods have not yet shown convincing improvement over state-of-the-art BCI methods."*

[8] **Lars-Erik Bjørge and Trond Emaus. "Identification of EEG-based signature produced by visual exposure to the primary colours RGB". MA thesis. NTNU, July 2017**
In this thesis, experiments were conducted on 10 participants using an open-source BCI. The participants were placed in a completely dark room and visually exposed to the primary colours. The data was decomposed with an Empirical Mode Decomposition (EMD), and the resulting Intrinsic Mode Functions (IMFs) were studied for patterns that could be used for separating the colours. The differences in frequency response were significant for each subject but not as evident across subjects.

[9] **Alejandro Torres-García, Luis Moctezuma, and Marta Molinas. "Assessing the Impact of Idle State Type on the Identification of RGB Color Exposure for BCI". in: Feb. 2020. DOI:** 10.5220/0008923101870194
Machine learning algorithms are applied in this paper to classify between idle state and RGB colour exposure. EEG signals from 18 subjects were recorded, and characteristics in the signals were extracted using two different methods. The first method was based on discrete wavelet transform, and the second on EMD. Training and testing were done using two different classifiers, support vector machine (SVM) and random forest (RF). The highest accuracy was 95% and was achieved by using EMD-based features.

[2] **Sara Åsly. "Supervised learning for classification of EEG signals evoked by visual exposure to RGB colors". MA thesis. NTNU, June 2019. DOI:** 10.13140/RG.2.2.13412.12165
This thesis aims to classify EEG signals produced by visual stimuli to the RGB colours. The dataset was recorded in-house with 17 participants. Dry electrodes were positioned on the subjects scalp at positions Fp1, Fp2, AF3, AF4, PO3, PO4, O1 and O2 according to the international 10-20 system. Two methods for classification were explored—the first used IMFs obtained from EMD as the base for feature extraction. The features were used as input for machine learning algorithms and obtained an average accuracy of 45%. The highest accuracy obtained for a subject-specific EEG signal model was 63%. When classifying between idle state and RGB colours, the EEG signal model reached an accuracy of 99%. The second method used a neural network and reached an average accuracy of 46% when classifying all subjects.

[10] **Mahima Chaudhary et al. "Understanding Brain Dynamics for Color Perception using Wearable EEG headband". In: *Proceedings of 30th Annual International Conference on Computer Science and Software Engineering 2020* (Aug. 2020)**
For the experiment described in this paper, a wearable EEG headband was used to collect EEG signals from eight participants. They used dry electrodes placed at positions AF7, AF8, TP9 and TP10 according to the international 10-20 system. The band power from the raw EEG was obtained by continuous Morlet wavelet transform. Spectral power features, statistical features, and correlation features were extracted from the band power. A reduction in the data dimension was performed with techniques such as Forward Feature Selection and Stacked Autoencoders. The highest average accuracy was 72% and achieved using Forward Selection and a RF classifier. The highest overall accuracy obtained was 81%.

Previous attempts have been made to identify neural descriptors of the RGB colours in EEG signals, but to the knowledge of the authors, no attempts have been made to classify them using Riemannian geometry. It has, however, been tried for Steady-state visually evoked potential (SSVEP) classification with promising results.

[11] **Emmanuel K. Kalunga et al. "Online SSVEP-based BCI using Riemannian geometry". In: *Neurocomputing* 191 (2016), pp. 55–68. ISSN: 0925-2312. DOI:** https://doi.org/10.1016/j.neucom.2016.01.007**. URL:** https://www.sciencedirect.com/science/article/pii/S0925231216000540
This article provides a review of the state-of-the-art in SSVEP-based BCI in 2016. A classification experiment is performed comparing state-of-the-art classifiers to Riemannian based classifiers in an offline setup. It claims to be the first to conduct an experiment using a Riemannian geometry classifier to classify SSVEP in an online scenario. The purpose was to differentiate between the three frequencies, 13, 17 and 21Hz, and a resting state. The results obtained from offline classification shows that the Riemannian classifiers outperformed the state-of-the-art with a 90% accuracy against 88%. In the online setup, the Riemannian classifier achieved an accuracy of 80% average.

What Remains to be Done?

From the literature presented, the highest average accuracy obtained classifying between the RGB colours is 72%, with 81% as maximum accuracy. Higher accuracy is required for practical use. To the knowledge of the authors, no one tried using Riemannian geometry for classifying between the RGB colours, which according to [7] is the current state-of-the-art for many BCI designs. A common problem in BCI models is the limited training data available. Transfer learning

can help solve this issue and should be further explored. Colour recognition in an online setting has not yet been tried.

1.2 Objectives

The main objectives of this thesis are:

O1: Find the EEG features that represent the characteristics of each primary colour.

O2: Create a general EEG signal model that can classify which colour was presented to the subject.

O3: Classify the EEG epochs across different recording sessions.

1.3 Approach

The dataset was imported into python with the `MNE`[12] library. For all subjects, each channel was plotted, and bad channels were removed from the dataset. The signals were then filtered, and the sources were extracted from the EEG signals using forward and inverse modelling. Several features were extracted, from the sources and sensors, and analysed, using the `pyRiemann`[13] and `MNE-features`[14] libraries. Using various combinations of features and channels, classification was performed on all subjects, with the `pyRiemann`[13] and `sklearn`[15] libraries. The authors focused on the classifiers that were described as state-of-the-art in [7]. EEG signal models which trained on one session and tested on the other were created and evaluated.

1.4 Contributions

The contributions of this master thesis are:

- An EEG signal model which separates RGB colours from another with an average accuracy of 75%, based on the EEG signals alone.
- A cross-session transfer learning experiment where 86% of the subjects tested showed an average variation of 4,6% compared to the source set. These results support the statement that Riemannian-based classifiers are robust for the session to session transfer learning.
- Evaluation of RGB colour separation from EEG source reconstructed signals.

1.5 Limitations

During the initial analysis of the signals from the subjects, some were noticed by the authors because they had more distinct characteristics that separated the colours better than other subjects. This favouritism of some subjects can have caused an unwanted bias towards using these features, and some subjects were discarded as poor performing. An even more extensive analysis of these subjects could have shown other features that distinguish the colours well.

No attempt to balance the dataset between three classes after rejecting some epochs was performed, so the chance level is not precisely 33% for all subject.

1.6 Outline

This thesis is divided into five chapters. In chapter 2, theoretical background on the activity of the brain, generation of EEG signals, and the visual system will be provided. Chapter 3 described the materials used for recording the dataset, and the methods of preprocessing, source localisation, feature extraction, classification and transfer learning. The results are presented in chapter 4. A discussion of the results, choice of parameters and future work can be found in chapter 5. Acronyms are explained in appendix A, and in appendix B, further plots of confusion matrices and ROC curves to supplement the results are included. A paper written by the authors and submitted to the 14th International Conference on Brain Informatics is included in appendix C.

Chapter 2

Background

This chapter explores the pathway of a visual signal in the eye and brain, from the light hits the eye until it is processed in the occipital and temporal lobes. This chapter [1] aims to present the background information that is necessary to understand the RGB experiments described in later chapters.

2.1 Brain signals

The brain uses electrical signals to control and monitor the functions of the body. The signals of interest in this project are mainly located in the occipital lobe, illustrated in fig. 2.1.

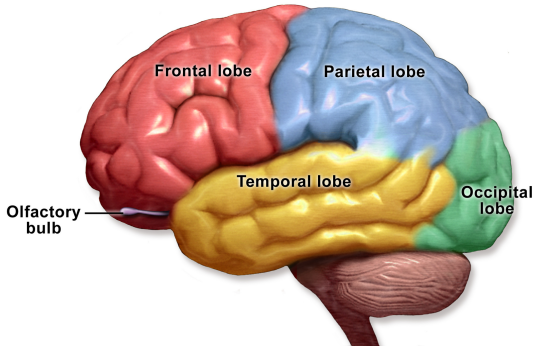

Figure 2.1: The lobes of the brain. The area associated with vision is located in the occipital lobe. Image source: [16]

[1] Note that this is an updated version of the background in the authors' previous work in [1]

2.1.1 Neural activity

The brain and spinal cord make up the central nervous system (CNS). The CNS is the part of the nervous system that controls the functions of the body and mind, e.g. thoughts, awareness and movements. Neurons are an essential part of the central nervous system because they respond to stimuli. When they notice a stimulus, they enable communication within the nervous system by transmitting information over long distances. A neuron is made up of three parts:

1. The cell body (soma), which contains the nucleus.
2. The dendrites, which are connected to the axons and dendrites of other cells, and receives stimuli from them, or relays stimuli to them.
3. The axon, which transmits electrical signals from the cell body to other neurons.

In the human brain, each neuron cell is connected to approximately ten thousand neuron cells [4]. An illustration of the body of a neuron can be seen in fig. 2.2.

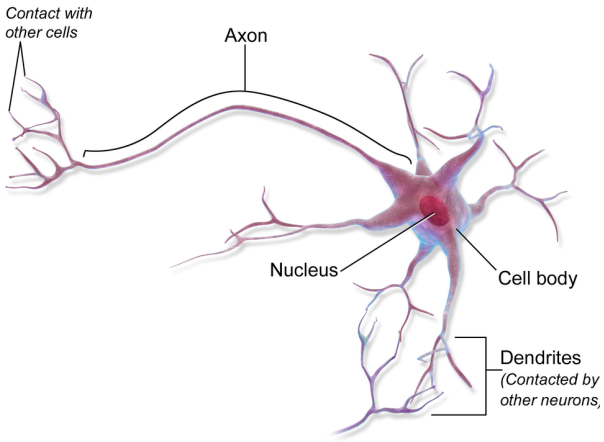

Figure 2.2: The body of a neuron cell. Image source: [16]

Post-Synaptic Potentials

All activity in the central nervous system is related to the transfer of synaptic currents between the synapses of axons and dendrites. In a resting state, the membrane potential can be recorded to be negative 60-70 mV. Changes in this potential appear when different synaptic activities occur. The synapses in the brain are divided into two categories, *excitatory* and *inhibitory* synapses. Potentials that travels along a fibre that ends with an excitatory synapse will cause a depolarisation of the membrane potential, indicating an excitatory postsynaptic potential (EPSP). If the fibre end in an inhibitory synapse, the potential will cause a hyperpolarisation of the membrane potential, also known as an inhibitory postsynaptic potential (IPSP). After an

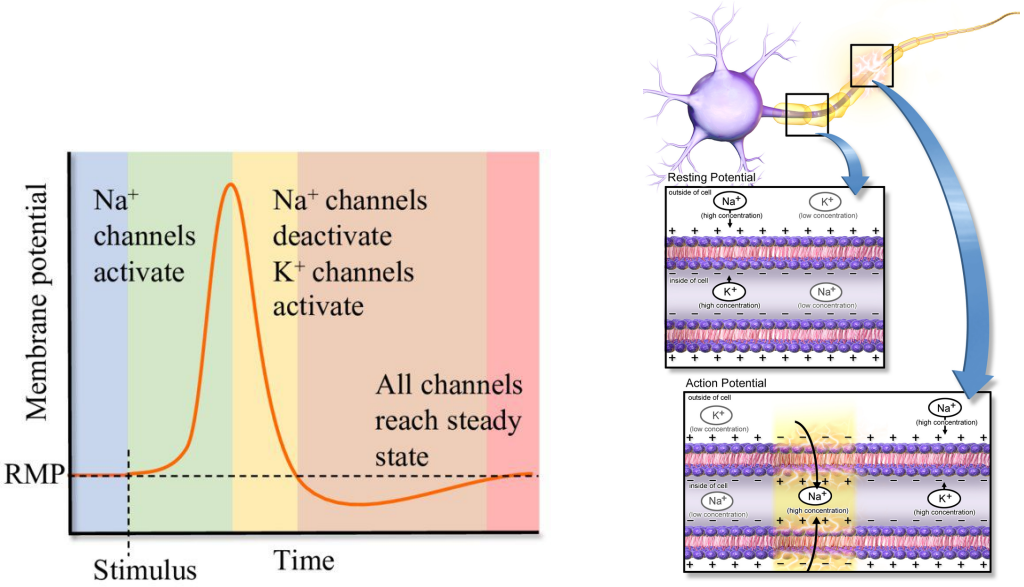

(a) The spike of the action potential compared to the resting membrane potential (RMP). Image source: [17]

(b) A resting potential and an action potential in the axon of a neuron. Image source: [16]

Figure 2.3: Illustrations of an action potential compared to a resting potential.

IPSP has been generated, a change in the membrane potential will occur.

Action Potentials

If more than one potential travels along with the fibre in a short time frame, their potentials will be summed. When there are enough EPSPs to increase the voltage above a certain threshold, the neuron will generate a pulse. This pulse is known as an action potential (AP), and it is a short-lived change in the potential of the membrane. The chemical process of an action potential, the exchange of ions, is illustrated in fig. 2.3b. The gates of the sodium (Na+) channels open when the nerve cell receives a stimulus through its dendrites. The potential needs to be driven from -70 to -55 mV in order for the process to continue. If it does, additional voltage dependant gates of the sodium channels will open. The influx of sodium ions in the cell interior increases the membrane potential further, to +30 mV. This process is called depolarisation, and the time interval marked with green in fig. 2.3a marks this part of the process. After the membrane potential depolarisation, the gates of the sodium channels close, and the gates of the potassium (K+) channels open. These changes cause the membrane potential to repolarise (see the yellow time interval in fig. 2.3a). As seen in fig. 2.3a, the repolarisation undershoots the resting potential, making it difficult to receive other stimuli until the resting potential is reached, assuring the

signal is travelling in one direction. [4]

2.1.2 EEG generation

An electroencephalography (EEG) signal is a measurement of the brains electric activity from the scalp. Synaptic currents are produced when a neuron is activated. These currents induce a magnetic field and an electrical field. The electrical field induced by the activation of a single neuron is too small to be recorded at the scalp. When a group of neurons are activated simultaneously, and in the near vicinity, the electrical field can be detected with electrodes through the layers of the head. About 10^7 neurons must be activated at the same time to create an electrical field large enough to be recorded through all the layers of the head [18]. An EEG signal is the result of the measurement of the electrical field. [4]

Event-related potentials (ERPs) are potentials in the brain that are generated as a response to sensory, affective and cognitive events [18]. Visually evoked potentials (VEPs) refer to the potentials caused by visual stimulus. They are recorded from the occipital lobe, which is the part of the brain involved in receiving and interpreting visual signals [19].

Figure 2.4 illustrates the different layers of the head through which that the electrical field is measured. Due to the different properties of the layers, as shown in table 2.1, the EEG signals are nonlinear. The signals are also non-stationary. In other words, the statistics of the signal such as mean and variance vary with time and can be observed e.g. during the change in alertness and wakefulness, during eye blinking, transitions between various ictal states, and in the ERP signals [18].

When recording an EEG signal, the system either uses dry electrodes or wet electrodes. Wet EEG systems are commonly used in clinical or research applications. When using wet electrodes, a conductive gel is applied to the electrodes. It reduces the impedance of the signal but increases the application time, as it is time-consuming to apply the gel to each electrode. In a dry EEG system, no conductive gel is applied. As a result, EEG signals recorded with a dry set of electrodes usually have significantly higher impedance values [20]. The impedance for each electrode should be below $5k\Omega$ [4], but this is difficult to obtain with dry electrodes.

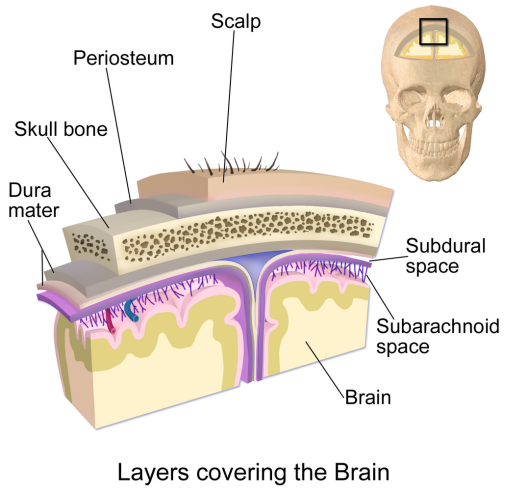

Figure 2.4: An illustration of the layers covering the brain. Image source: [16]

Table 2.1: The thickness and resistance of three layers of the head [4].

Layer	**Thickness** [cm]	**Resistance** [Ω]
Scalp	0.2 - 0.5	300 - 400
Skull	0.3 - 0.7	10k - 25k
Cortex	0.1 - 0.3	50 - 150

2.1.3 Brain rhythms

The bands of frequencies of the electrical fields in the brain are referred to as brain rhythms. There are five primary brain rhythms characterised by their frequency bands and the state of the brain for which these bands are associated [4]. The bands, frequencies and association are listed in table 2.2.

Table 2.2: Brain rhythms [4].

Name	**Frequency band** [Hz]	**Associated with**
Delta (δ)	0.5 - 4	Deep sleep
Theta (θ)	4 - 7.5	Drowsiness
Alpha (α)	8 - 13	Relaxed awareness
Beta (β)	14 - 26	Active thinking
Gamma (γ)	> 30	Detecting brain diseases

2.2 Colour vision

2.2.1 How humans see colours

When light hits the eye, it travels through the lens to the retina at the back of the eye. Light sensing cells known as photoreceptor cells are found in the retina. There are two types of photoreceptor cells, rods and cones. The cones are responsible for colour vision. Humans are trichromats, and therefore have three different cones in the retina. The photons of the light activate the cones when they are hit by light. The three different kinds of cones absorb light of different wavelengths, as can be seen in fig. 2.5. When the light activates the signalling system in the cones, the energy from the light is transformed into action potentials in the neural cells. The signal is then sent to the brain through the optic nerve. This is illustrated in fig. 2.6.

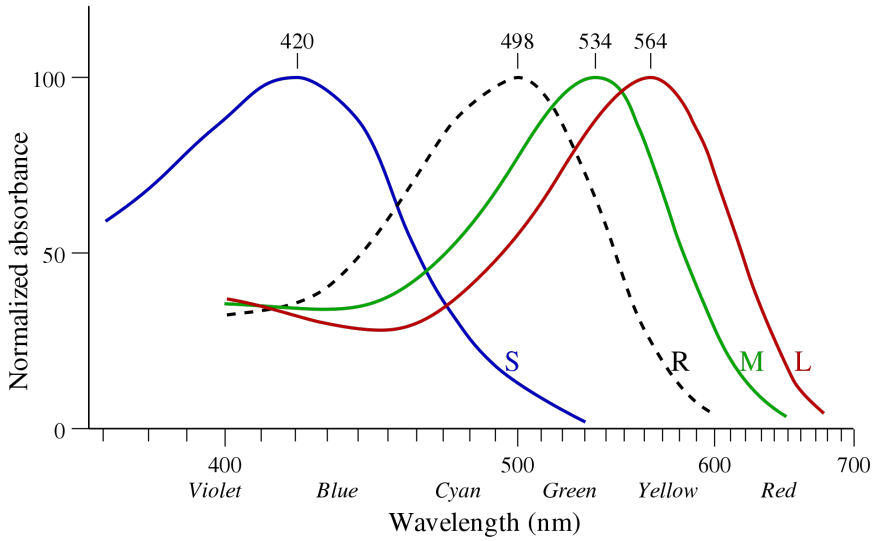

Figure 2.5: The wavelengths absorbed by the rod (dashed black) and the three different kinds of cones. The majority of the cones are of the long type (red). About a third of the cones are of the medium type (green), and only about ten percent of the cones are of the short type (blue) [21]. Image source: [22]

2.2.2 Visual pathway

The action potential formed by the excitation of the cone in the retina travels through the optic nerve, through the lateral geniculate nucleus (LGN) to the primary visual cortex (V1) in the occipital lobe of the brain. From the primary visual cortex, visual information splits into two pathways. Information relating to the movement and location between objects in the view of the eye navigates along the dorsal stream to the parietal lobe. Information that describes the form of the object, like the colour, takes the path along the ventral stream to the temporal lobe.

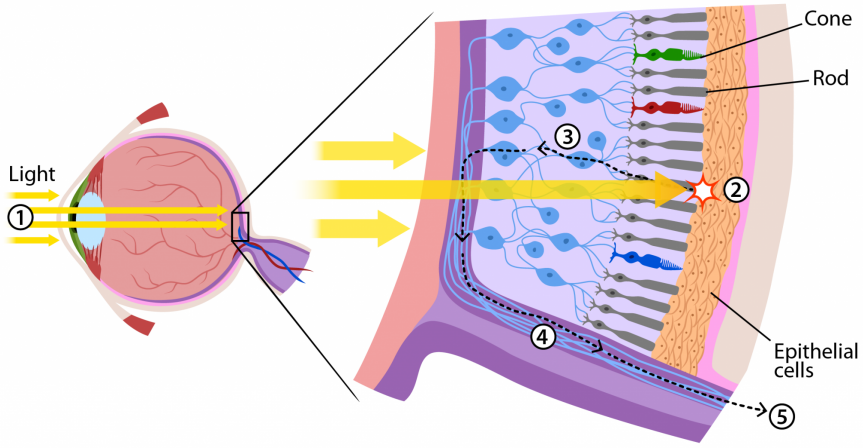

Figure 2.6: Light enters the eye (1) and activates the rods in the retina (2). The light is transformed into action potentials in the neural cells (3), and travels through the optical nerve (4) to the brain (5). Image source: [23]

The two streams of visual information are illustrated in the right brain in fig. 2.8.

In [24], it is stated that the occipital lobe is separated in distinct areas, as demonstrated in 2.8, with specific attributes to the vision such as motion, orientation and colour. Furthermore, the attributes processed in separate areas are also perceived individually. It implies that if the area that processes and perceives a specific attribute is damaged, this will not affect the remaining areas. Moreover, the book refers to cases when the whole of the visual brain is damaged (including the primary visual cortex V1) except V4. The patient can still see and distinguish colours but not bind the colours to surfaces. Most interesting to this thesis is the colour centre V4, where the wavelength- or colour-selective cells are indifferent to the shape and motion of the stimuli presented. The colour centre is also referred to as V8 in some publications [24].

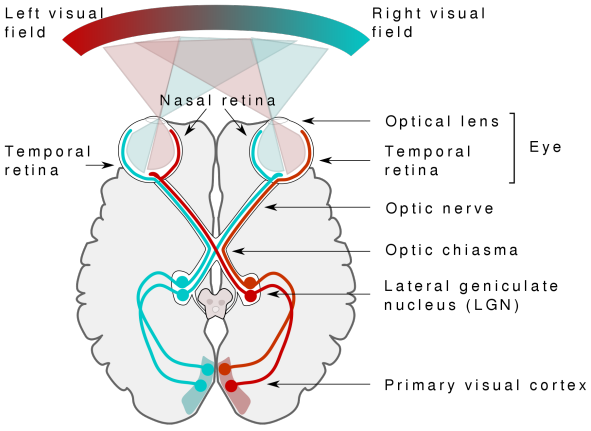

Figure 2.7: The visual path from the retina to the primary visual cortex. Image source: [25]

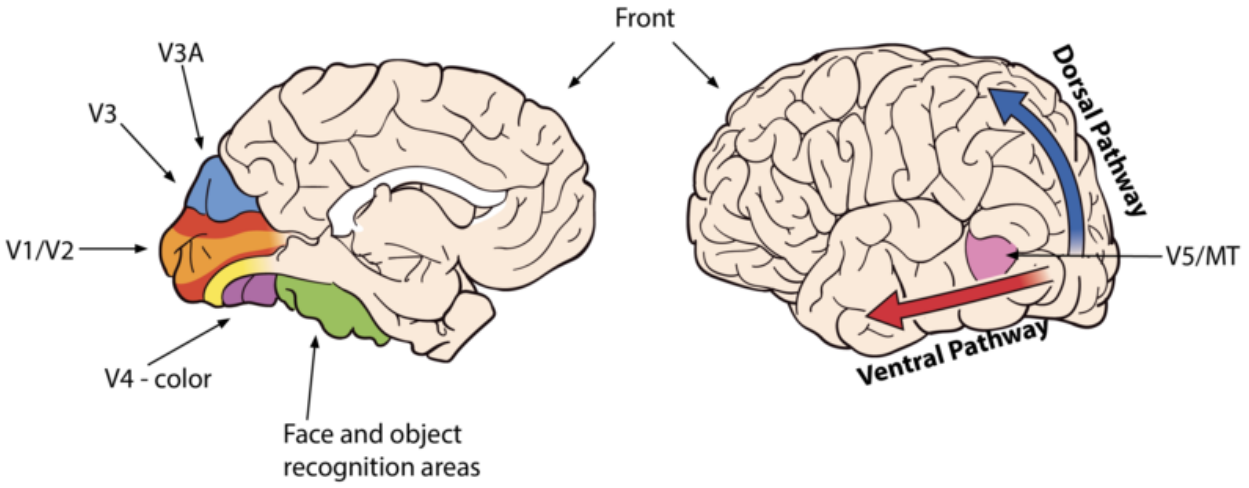

Figure 2.8: An illustration of the regions of the occipital lobe and their functions. The dorsal pathway takes the signal from the primary visual cortex to the parietal lobe, and the ventral pathway connects the primary visual cortex to the temporal lobe. Image source: [26]

2.2.3 Event related potential (ERP) components

Specific components in the signals appear as a response to the brain transforming information from sensory stimuli to the appropriate behaviour [27]. These components are illustrated in fig. 2.9. C1 is the immediate response to visual stimuli, which have a latency of approximately 50-70ms, and can have both negative and positive polarity. P1 and N1 are the following components with latency between 90-200ms. P1 is related to sensory and perceptual processing, while N1 is related to expert recognition and visual discrimination. N2 and P3 are associated with the categorisation of the visual stimuli and the working memory.

Notice how the signal in fig. 2.9 is flipped with negative polarity upwards. It is a one-time case and will not reappear in this thesis.

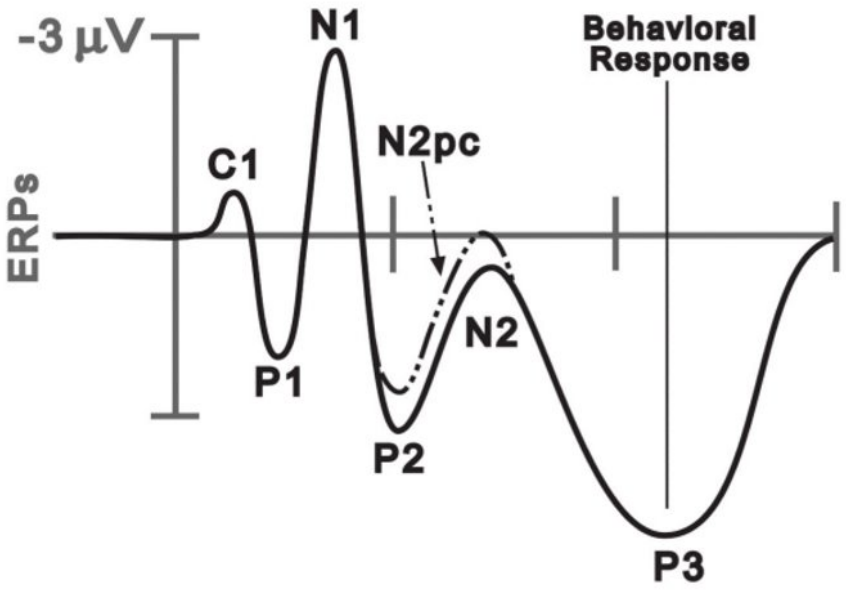

Figure 2.9: ERP component response to sensory stimuli. Image source: [18]

2.3 EEG recording and measurement

Using EEG recordings when analyzing the activity of the brain has many advantages. The first is that the equipment is relatively cheap and easier to use than the machine used to make a magnetoencephalography (MEG) recording. The second good reason to use EEG is that there is no need for an invasive medical procedure, unlike the electrocorticography (ECoG) method, where the brain is monitored with electrodes placed directly on the exposed cortex. Compared to functional magnetic resonance imaging (fMRI), the temporal resolution is high. A limitation of the EEG measurement is that the spatial resolution is low, meaning that it is difficult to know the location of the source of a signal. In addition, an EEG signal is vulnerable to noise. Electronic devices close to the subject, the subject blinking or moving its head, can be sources of noise and corrupt the signal. [4]

Chapter 3

Materials and Methods

The raw EEG signals are recorded as described in section 3.1. Section 3.1.4 explains how the raw signal is filtered, shifted and cropped, and which threshold is used to reject epochs. Source localisation was evaluated, and the method is described in section 3.2. An analysis of the signals is provided in section 3.3. In section 3.4, the features that are extracted from the signal are described. Theory about the classification algorithms used in this thesis is found in section 3.5. Finally, the method of transfer learning is described in section 3.6.

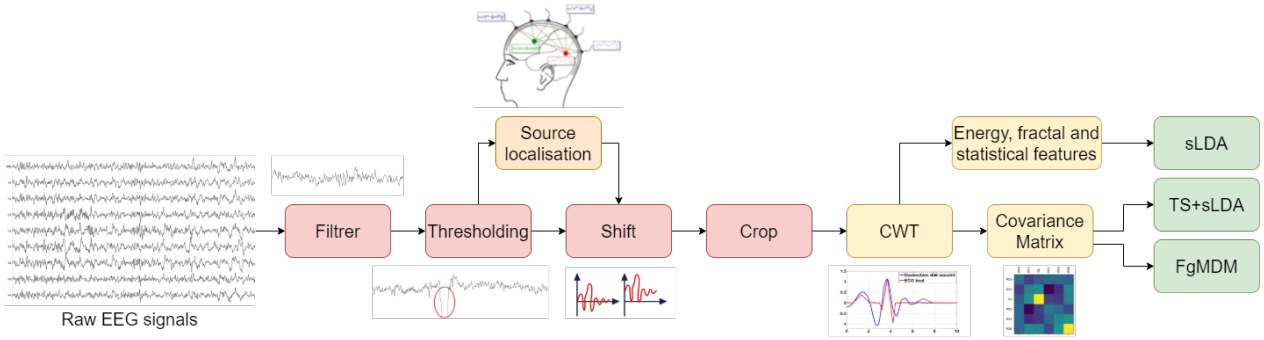

Figure 3.1: Flowchart of the EEG signals

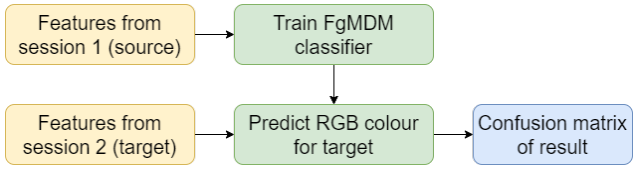

Figure 3.2: Flowchart of the EEG signals in a transfer learning setting

3.1 Dataset

3.1.1 Equipment and functionality

The dataset was recorded at the NeuroImaging facilities at Aalto University in Helsinki by Andres Soler. The recording was situated in a high-end 3-layered magnetically shielded room, and the EEG recordings were taken simultaneously as magnetoencephalography (MEG) measurements were recorded with the MEG Core [28]. However, only the EEG recordings were used in this thesis. The cap used for the EEG recordings was a 64-channel cap from antNeuro (ANT Neuro, Netherlands https://www.ant-neuro.com/) [29], consisting of four EOG channels to detect blinks, movement and other muscular interferences. The 60 remaining electrodes were all EEG channels, and their placement is illustrated in fig. 3.4.

3.1.2 Procedure

When fitting the cap, the electrodes were dry and then infused with conductive gel. Before beginning the experiment, all electrodes were measured to have an impedance below $5k\Omega$. The subjects were placed in front of a screen inside the high-end 3-layered magnetically shielded room. The screen randomly showed the RGB colours for 1.3 seconds each, with a grey screen in-between. The colour code used for the three colours was (FF0000), (008000) and (0000FF) according to hex code. The green colour (00FF00) is bright and was therefore toned down to (008000), because high light exposure could make the participants turn their eyes in another direction. The length of time the grey screen was presented varied to prevent the adaptation of the brain. All colours were presented in full-screen mode. During grey colour, a cross was presented in the middle of the screen. This cross was included to keep the focus of the subjects in the same area. The presentation of stimuli is illustrated in fig. 3.3.

At least 140 epochs of each colour were recorded for each session, with three breaks lasting for one minute each during the recording. Subjects were asked to try blinking only during the grey coloured screen.

A camera was placed in the room so the subjects could be observed from the outside. The experiment can be tiresome, and some participants seemed to fall asleep or constantly moved during recording. The data from these subjects have been excluded from the experiments conducted in this thesis.

Thirty-one subjects were recorded in total. The two channels Oz and O2, were flat in the first recording of subject 1-18 and subject 26 and did not record any brain activity. For this reason,

they were marked as bad. Some of these subjects were rerecorded the following week with all functioning channels. The remaining twelve subjects only had one recording.

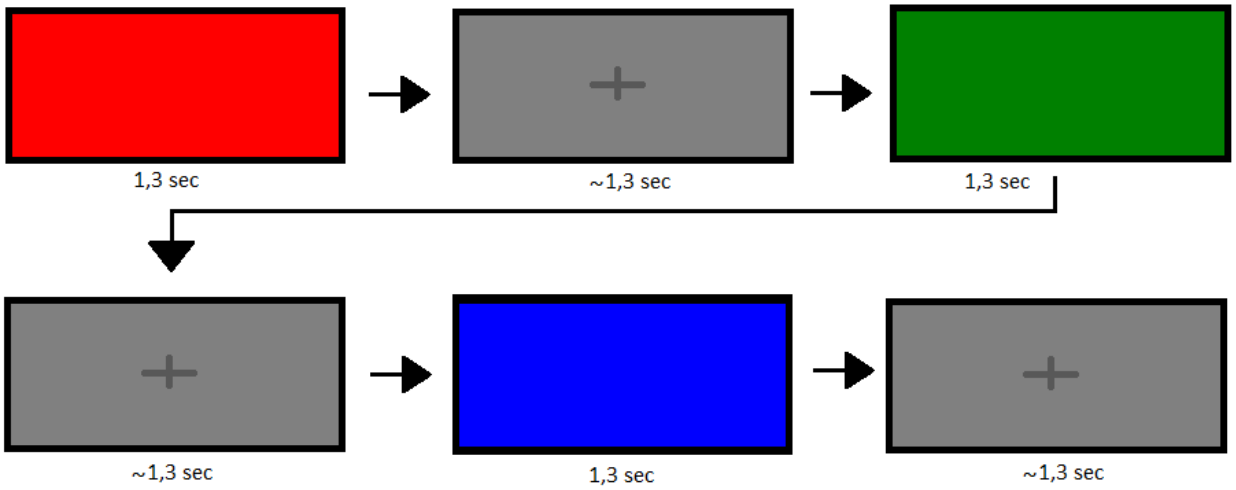

Figure 3.3: An illustration of the protocol used when recording data.

3.1.3 Resulting dataset

The following requirements were made for using the data for colour classification

1. None of the channels placed at the visual cortex are marked as bad.
2. The subject had a correct behaviour during recording (e.g. looked at the screen and kept its eyes open).
3. After pre-processing the data (see section 3.1.4), and removing bad epochs, at least 60 epochs of each colour remains.

The final dataset used for classification is shown in table 3.1

Table 3.1: The number of epochs for each subject and session that fulfil all three criteria.

Subject	Session	Red epochs	Green epochs	Blue epochs
2	2	132	135	134
6	2	134	137	133
7	2	107	106	99
8	2	105	102	94
11	2	119	126	118
13	2	131	128	130
14	2	120	120	113
15	2	98	95	90
16	2	115	125	125
18	2	139	139	139
20	1	132	136	136
21	1	71	57	63
24	1	95	106	89
25	1	107	91	91
26	2	114	112	121
28	1	134	133	131
30	1	109	109	109
31	1	137	135	133

The subjects with two recording sessions and a high enough accuracy were explored for the session to session transfer learning. Note that the first session has two back channels with a flat signal for all subjects. These subjects are listed in Table 3.2

Table 3.2: The number of epochs for the subjects that only fulfil criteria 2) and 3).

Subject	Session	Red epochs	Green epochs	Blue epochs
2	1	111	121	112
7	1	131	133	128
8	1	106	95	86
11	1	135	134	133
13	1	122	122	121
14	1	111	113	110
18	1	125	124	122
26	1	122	121	114

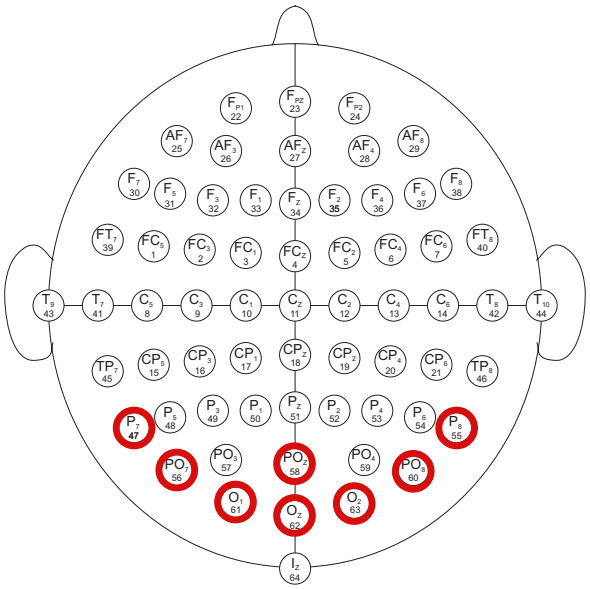

Figure 3.4: All channels. The selected channels are marked with red. Image source: [30]

3.1.4 Preprocessing

Bandpass and Notch filter

The mne.io.Raw class has built-in methods for filtering the raw signal. Two of those methods were applied to the dataset used in this thesis. First, the raw signal was filtered using a finite impulse response (FIR) filter between frequencies 0,1 Hz to 40,0 Hz, and the parameter `fir_design` was set to `firwin`. Second, a notch filter was applied to remove the utility frequency of 50 Hz. The source code for FIR filter and notch filter is found in the MNE python library [12]. A plot illustrating the signal before and after applying the filter is found in fig. 3.5.

EEG reference

When recording EEG signals, a reference electrode is used to measure the voltage between each electrode and the reference electrode. The voltage obtained in the reference is subtracted from the other channels. Therefore, the ideally placed reference channel can capture noise and interference of the signal, but no brain components. Typical placements of the reference are the earlobes, nose or collarbone. In this thesis, a virtual reference has been applied. The virtual reference is the average of all channels, not including channels marked as bad.

When using the method of virtual reference from the MNE library[12], the reference can be applied as a projection rather than subtracted from the data when recording. Furthermore, when applying the reference as a projection, it can be turned on and off. It also allows for marking additional channels as bad, and then it recomputes the reference. Another advantage of applying

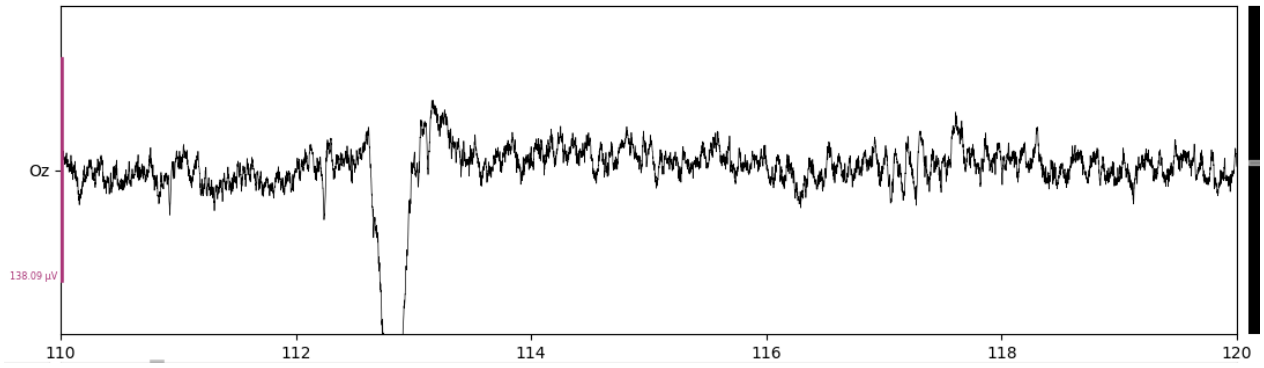

(a) The first ten seconds of the unfiltered signal from channel F3, subject 2 session 2.

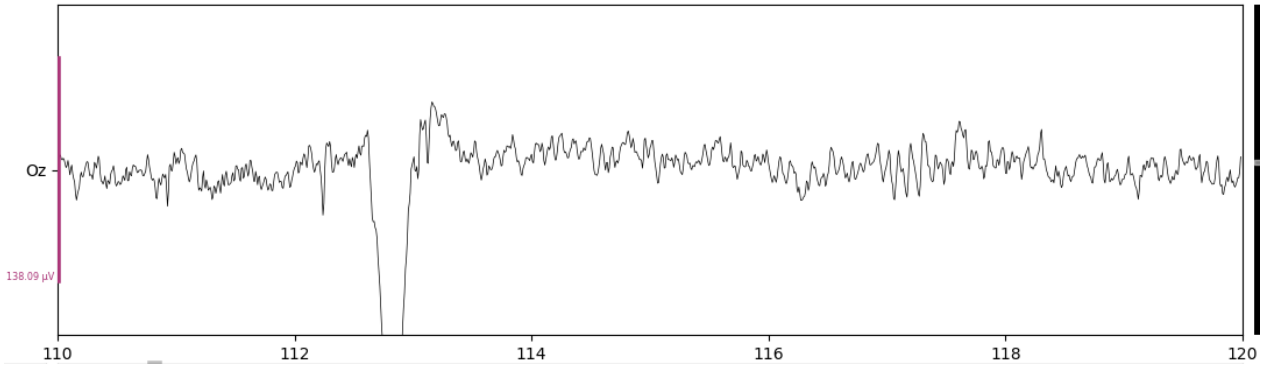

(b) The first ten seconds of the filtered signal from channel F3, subject 2 session 2.

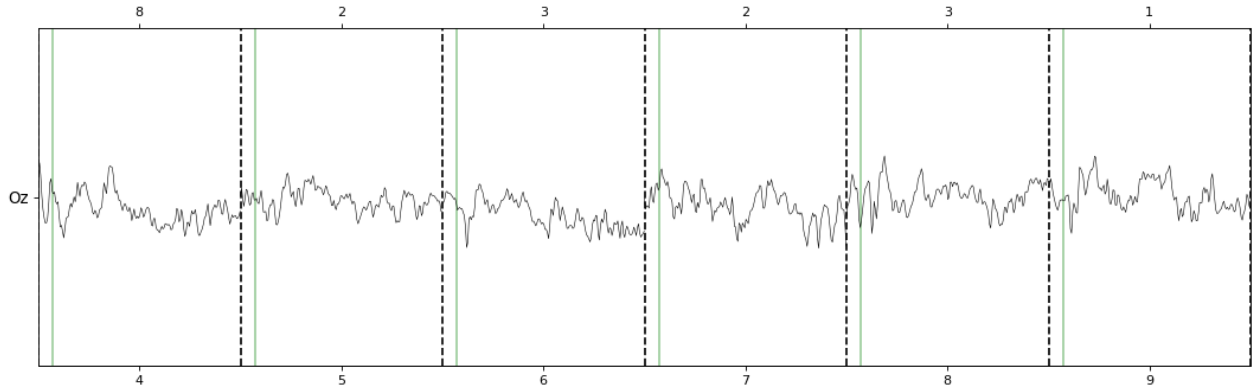

(c) The finished signal seperated into epochs, and epochs containing artifacts has been removed.

Figure 3.5: Parts of an EEG recording from channel F3.

the reference as a projection is the possibility of re-referencing to a more suitable reference at any given time.

Thresholding

When creating the epochs using MNE, an amplitude threshold criteria is available to reject epochs. The purpose of this is to remove all epochs containing blinks, eye movement, or other muscular interference. These interferences usually have a higher amplitude than the brain sig-

nals of interest and can corrupt the signals. This is illustrated infig. 3.5c, where the epoch containing the artefact observed in fig. 3.5a and fig. 3.5b between 112 and 114 seconds has been removed. This thesis set the threshold criteria to 150μV for EOG channels and 120μV for EEG channels.

Shifting the signal

A form of vertically shifting the epochs was necessary to re-adjust each epoch without corrupting the features of the data. First, the lowest voltage value in an epoch was detected. Then, the lowest value was added or subtracted (depending on the polarity) to all samples in the epoch. It was done for all epochs, and as a result, the epochs were shifted above zero for all samples.

Standard scaler

The standard scaler standardises the features by subtracting the mean and scaling to unit variance. The standard score z is

$$z = \frac{x - \mu}{\sigma} \tag{3.1}$$

where x is the sample, μ is the mean of the data in the training samples and σ is the standard deviation. [15]

Power transformer

The power transformer applies a power operation to the features to make the data more Gaussian-like. [15]

Artifact reparation with ICA

The authors are familiar with the Independent Component Analysis (ICA) method for repairing artefacts, and it was utilised to remove eye and muscular artefacts at one point. This method can reduce the number of epochs that are rejected due to blinking. However, it was concluded that there was no point in removing blinks from the signal because the goal was to find features representing the subject looking at various colours. It was, therefore, unnecessary to include epochs where the subject was blinking and thereby not looking at the colour.

3.2 EEG Source Localisation

3.2.1 Motivation

The electrical potentials in the brain can be modelled as electric dipoles. An electric dipole consists of two opposite electrical charges. As mentioned in section 2.1.1, the changes in electrical potentials are caused by the sum of postsynaptic graded potentials. These potentials create electric dipoles between the soma and dendrites from other neurons. From the EEG recordings, estimations of the position of the source of activity can be made. As mentioned in section 2.3, an EEG recording has a low spatial resolution because the measurements are taken outside the scalp. From section 2.2.2, the location of the colour centre is in the V4-area of the visual cortex in the occipital lobe. To find the activity that stems from this location could therefore be very effective when differentiating RGB signals. Figure 3.6 shows the signals that stem from two sources, and an example of how those signals appear when measured at the scalp. The signals from the sources overlaps in the EEG recordings. Forward and inverse modelling can disentangle the overlapping source time series.

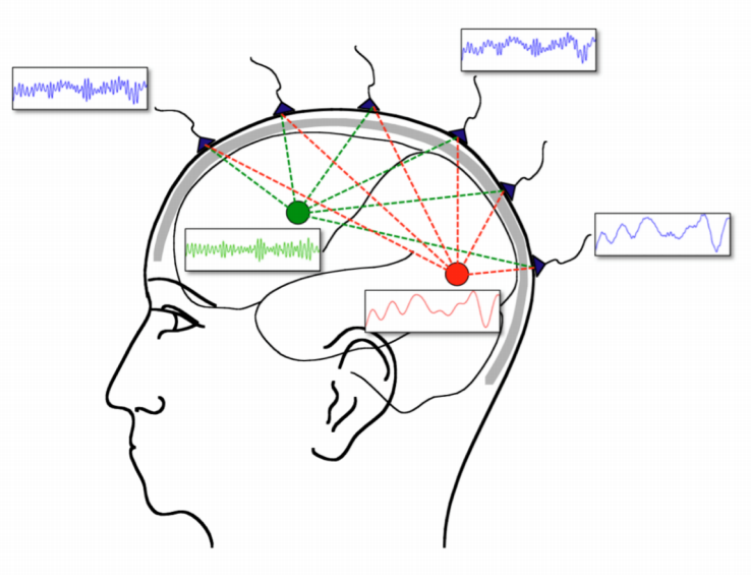

Figure 3.6: Two sources (red and green) with different time series. At the scalp, these time series (blue) are overlapping. Image source: [31].

3.2.2 Method

The forward and inverse problem

The purpose of the inverse problem is to identify the origin of the brain's electrical activity from the mixture of noisy signals recorded at the scalp. The solution to the forward problem is to gen-

erate EEG data from a known source signal, as illustrated in fig. 3.7. To estimate the location of the source, a model of the source and the head is required. A single dipole is the simplest model of the source [32]. The potential in an electric dipole decreases with the squared distance from the centre of the dipole. Its electric field is the most substantial parallel to its axis and weakest perpendicular to it. By utilising the characteristics of dipoles, the electrical fields created by theoretical dipoles can be predicted [33]. The least complicated head model is a sphere with layers, where each layer has a different conductivity, representing a layer of the head (see table 2.1). In this project, a more realistic model of the head has been used.

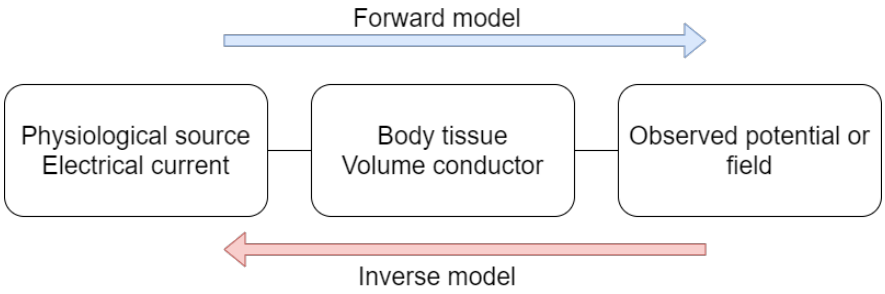

Figure 3.7: Physiological sources in the brain are causing electrical currents. The volume conductor is the tissue of the brain, skull and scalp that the electricity flows through. With electrodes, the potential can be measured. The forward model computes the observed potential from the electrical current at the source. The inverse model starts from the observed potential and calculates the source.

Boundary Element Method

The Boundary Element Method (BEM) creates surface models of the different layers of the brain. These surfaces are formed of triangular plane elements, and an example can be viewed in fig. 3.8. The BEM calculates the potential values from a given current source (dipole) at the volume boundary. When using the Boundary Element Method to create a model of the conductivity of the head, it is assumed that the regions between the interfaces (the cortex, skull and scalp) are homogeneous and isotropic [34].

It is shown in [34] that the potential values at the surface can be written as a set of linear equations:

$$\mathbf{X} = \mathbf{CX} + \mathbf{S} \tag{3.2}$$

where $\mathbf{X}$ is the column vector that denotes the wanted potential at every node, $\mathbf{C}$ is a square matrix, with elements that are determined by the geometry and electrical conductivity of the

model, and **S** a vector whose elements are the potential values in an infinite homogeneous medium due to a single source. Equation (3.2) can be solved for a particular **S** (a source) using an iterative solver. Because eq. (3.2) can be written as:

$$\begin{aligned} \mathbf{X}[\mathbf{I}-\mathbf{C}] &= \mathbf{S} \\ \Rightarrow \quad \mathbf{X} &= [\mathbf{I}-\mathbf{C}]^{-1}\mathbf{S} \end{aligned} \tag{3.3}$$

where **I** is the identity matrix, **X** can be found by a matrix multiplication of $[\mathbf{I}-\mathbf{C}]^{-1}$ and **S**. Once the inverse matrix is calculated, the forward solution for the potentials produced by a dipole can be calculated with a quick matrix multiplication, effectively reducing the number of computations necessary [32].

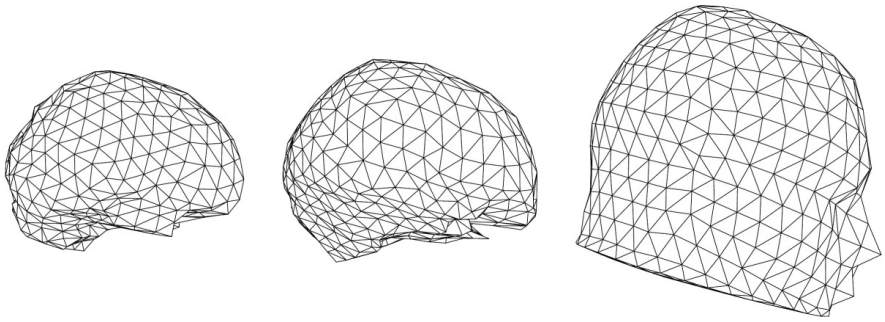

Figure 3.8: An example of the triangulated surfaces of the brain from the BEM. The first surface is between the skull and the brain, the second is the scalp-skull interface, and the third is between the scalp and air, also known as the outer surface. Image source: [34]

The BEM model is visualised in fig. 3.9a, and the BEM with the source model can be viewed in fig. 3.9b.

Inverse solution

In this project, a distributed source model was used to find the inverse model. When using this model, the position of the source is not estimated. Instead, a set of dipoles with known location are distributed in the cortex during modelling. For each dipole, its strength is estimated. From this, the data and noise can be perfectly explained. The distributed source model is a linear problem, but it has more unknown parameters than known measurements, meaning an infinite number of solutions exist. Additional constraints were required to find a unique solution and avoid over-fitting. With noise, the forward model is

$$\mathbf{X} = \mathbf{L}\mathbf{S} + \upsilon \tag{3.4}$$

where $\mathbf{L} = [\mathbf{I}-\mathbf{C}]^{-1}$ is the Lead-field matrix and υ is the noise. The constrains are:

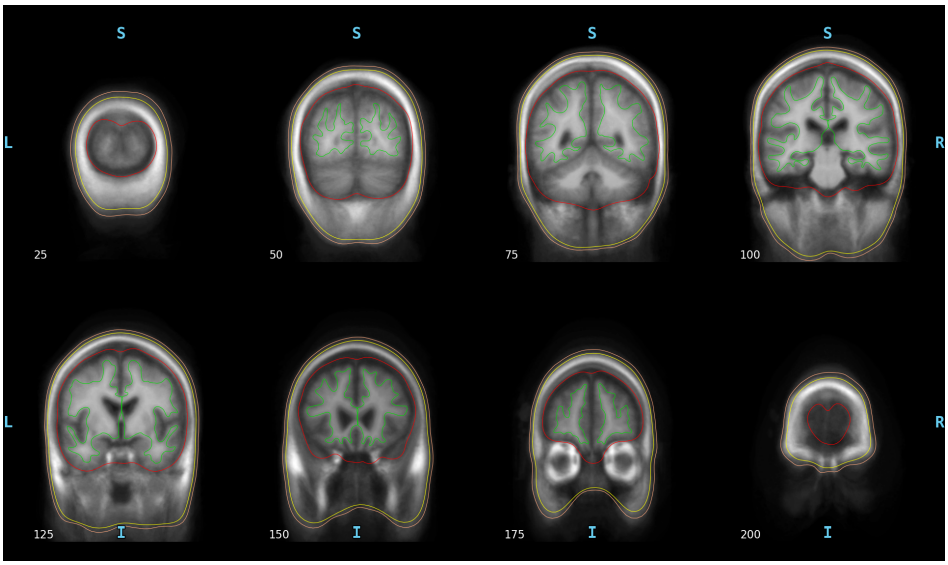

(a) Cross sections of layers of the BEM

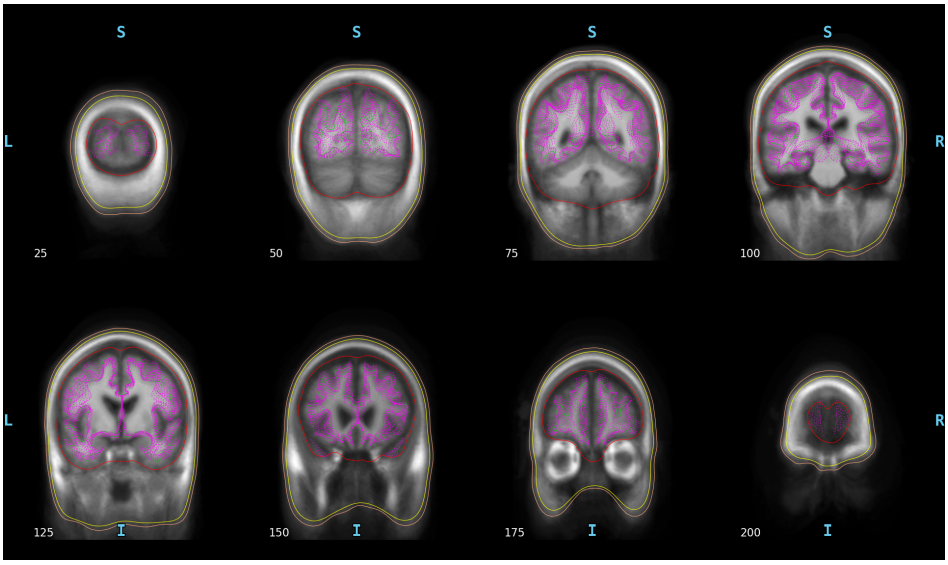

(b) Cross sections of the BEM with the sources in pink.

Figure 3.9: A visualisation of the BEM surfaces from the Freesurfer `fsaverage` subject. The 'S', 'I', 'L' and 'R' notations represents the Superior, Inferior, Left and Right views of the brain, respectively.

$$\min_{S}\{\left\|\mathbf{X}-\mathbf{LS}\right\|^{2}+\lambda\cdot\left\|\mathbf{DS}\right\|\} \tag{3.5}$$

where λ and $\mathbf{D}$ are regularisation parameters. [31]

When computing the inverse model, the `dSPM` method was used for noise normalisation. [35]

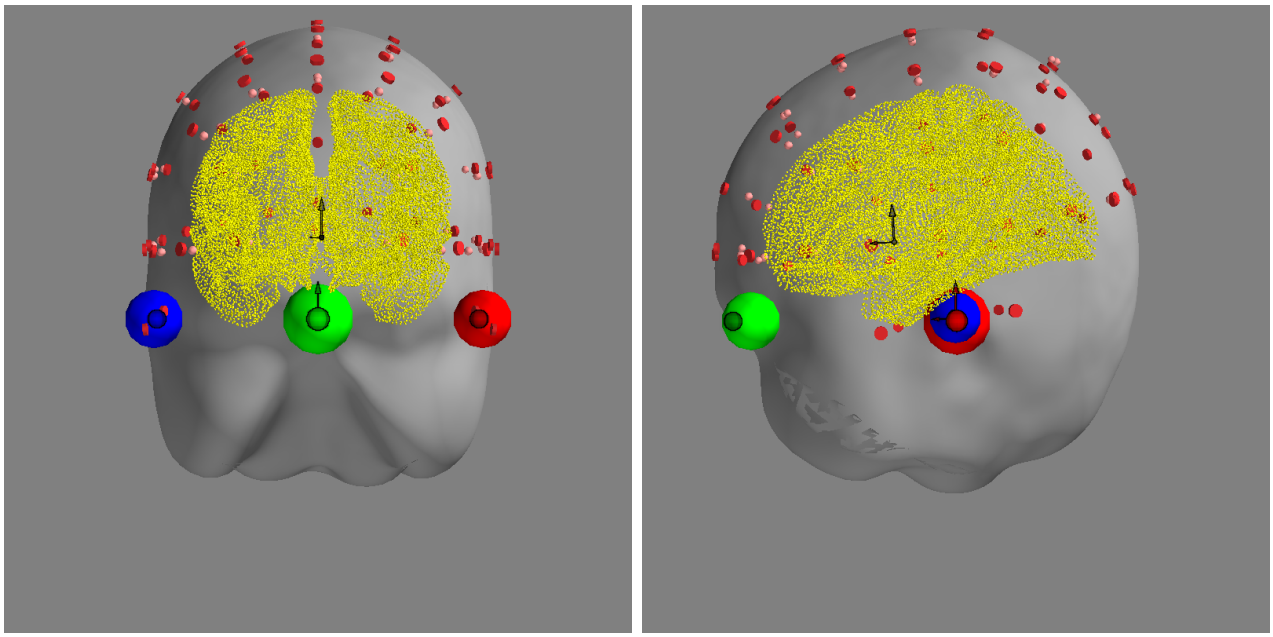

(a) Anterior view (b) Left lateral view

Figure 3.10: The head, sensor and source space (yellow) alignment for subject 21, when using the standard template MRI subject `fsaverage`. The original node locations are marked in pink, and the projected locations are red.

Atlas and labels

The Boundary Element Model and source space model used in this thesis are from `fsaverage` (FreeSurfer, https://surfer.nmr.mgh.harvard.edu/), which is based on an average of 40 subjects, both males and females ages 18 to 93. A plot of the sensor space, original node locations and projected node locations can be seen in fig. 3.10. The atlas used in this experiment is based on the `HCPMMP1` atlas from [36], and it is called `HCPMMP1_combined`. The `HCPMMP1` atlas contains 362 labels (from both hemispheres) that represent a small area each, while the `HCPMMP1_combined` atlas combines these labels into 46 labels representing larger areas. Because the boundary element model used in this thesis is based on an average of 40 subjects and not specifically created for each of the subjects recorded for this experiment, the decision to use the atlas with fewer labels (`HCPMMP1_combined`) was taken to reduce the likelihood for a response being outside the region of interest. The labels `Primary Visual Cortex (V1)-lh` and `Primary Visual Cortex (V1)-rh` were used. These labels are visualised on the brain in fig. 3.11. From these labels, the `pca_flip` mode was used to extract the signal. `pca_flip` applied singular value decomposition to the time courses, and the first right-singular vector represents the time course.

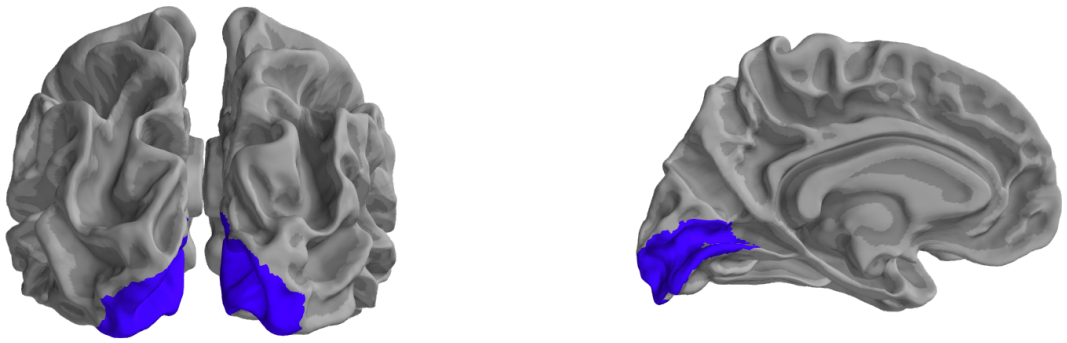

(a) Posterior view

(b) Left sagittal view

Figure 3.11: The locations of the `Primary Visual Cortex (V1)` labels used when extracting time courses from the sources.

3.3 Data analysis

In preprocessing, feature extraction and classification, it is helpful to understand the signal and what to look for in the signal. The approach used in this thesis was to visually inspect the signals for features and extract these features before classifying them. This section describes the features observed and compare features found for the different colours. It looks at the consistency of features in a session, similarities and differences across sessions, and compare signals produced across subjects. When analysing the signals from different subjects of the dataset used in this thesis, the most prominent trend between subjects is the lack of one. However, the signals produced by an individual subject have visible correlations, often even across sessions. The data from Subject 2 will be used in the rest of this section for analysis and illustrative purposes.

3.3.1 The averaged signal

First, the averaged of the signals was plotted for each colour and all channels, and it can be seen in fig. 3.12. The plots include topographic maps for some of the peaks in the averaged signal as well. It indicates similarities and differences between classes. The first impression of fig. 3.12 is that the signals are easily separable between classes, and the activity providing the highest amplitude is centred in the back channels. Some similarities between the classes are found. All colours have a negative peak at approximately 60 milliseconds in the back channels and a positive peak at approximately 100 milliseconds. These peaks are less prominent in the green average than in the red and blue averaged. From section 2.2.3, these can be identified as C1 and P1, and the following negative peak as N1. N1 is more easily spotted in the red averaged plot than in the green and blue averaged. The activity in the front channels appears to have a counter-reaction to the activity in the back channels. Although the peaks in the front channels are lower in amplitude, red and blue averaged seem to have a substantial and negative peak at approximately 200 ms. The green averaged seems to have a positive peak at approximately 150 ms. These observations, including all channels, should provide a strong foundation when separating colours.

3.3.2 Trending features

Features of interest need to have consistency throughout all epochs in a session. The next step is to see if the features found in the averaged signal are not just an arbitrary result from averaging. The left column in fig. 3.13 is the plotted image of all epochs of each class from the channel 'Oz', with the averaged response plotted below. The grey area around the averaged response illustrates the 95% confidence band. The first 300ms of most epochs show a strong trend resembling the averaged signal, especially for the red and blue epochs. Based on fig. 3.13, the peaks

of the signals should be utilised as a feature for classification. If looking at the plotted images from the frontal channel 'Fz' in fig. 3.13, it is clear that these do not show the same trends as the backchannel Oz. The amplitude of the VEPs in the averaged signal for Fz is much lower than in Oz. Furthermore, the confidence band is larger in Fz, and the consistency of a pattern is much less visible in the images of all epochs.

From section 3.3.1, it is clear that there is some activity in the frontal channels as well as the back channels. However, the signals obtained from the frontal channels do not seem to have an equally strong consistency in the VEPs as the signals from the back channels.

3.3.3 Features across sessions and subjects

From observing the dataset used in this thesis, the change from session to session is usually no more than a shift in the data, while the pattern does not differ dramatically. Illustrated in fig. 3.14. The red average is more or less identical between the two sessions, while the blue average has a double in amplitude in session two compared to session 1. There are some changes in amplitude for the green average, but the pattern is very similar across sessions.

The data between subjects, however, differ widely in both shape and amplitude. Illustrated in 3.14. The peaks C1, P1 and N1, can be identified for both subjects simultaneously, but their characteristics in amplitude are still quite different. Similarities and differences are also illustrated in the covariance matrices in fig. 3.16 with the average covariance between six channels.

3.3.4 Sources of brain activity

An advantage of source reconstruction described in section 3.2 is the possibility of localising activation. Classifying based on localisation of activation have proved useful in other BCI protocols such as motor imagery. In this project, the source reconstruction used signals from the 60 available EEG electrodes. Figure 3.17, fig. 3.18 and fig. 3.19 are 3D-plots of the average brain activation of subject 2 when exposed to red, green and blue respectively. It is important to emphasise that while this plotted average distinguishes the colours, the data used when classifying is noisier. The blue and orange beads represent the source of the highest activity in each hemisphere. Notice how the brain models have been rotated in order to visualise the beads properly. Figure 3.17 and fig. 3.19 were plotted using a posterior view, and fig. 3.18 was plotted using a ventral view. It is clear from these plots that the sources of activity are located similarly for all colours. The activation is focused in the visual cortex, except for activation produced by blue exposure, which seems to trigger some activity in the temporal lobe as well.

The plot produced by the activation is plotted underneath the brain model. The orange line represents the activation in the right hemisphere, and the blue line represents the left hemisphere. There are evident differences between colours in the plots created by the activation. It indicates that the activation itself is a better feature for classification than the location of the activation.

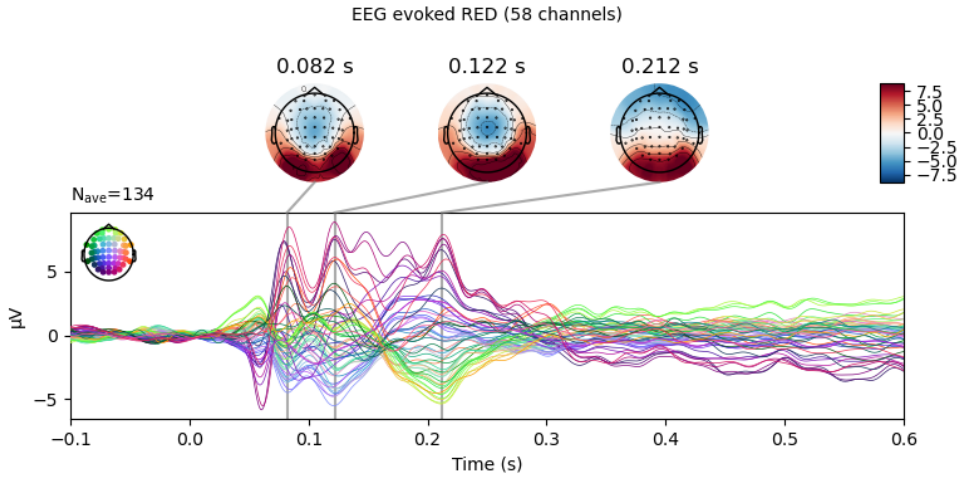

(a) A butterfly plot of the red evoked of all EEG channels used when recording Subject2.

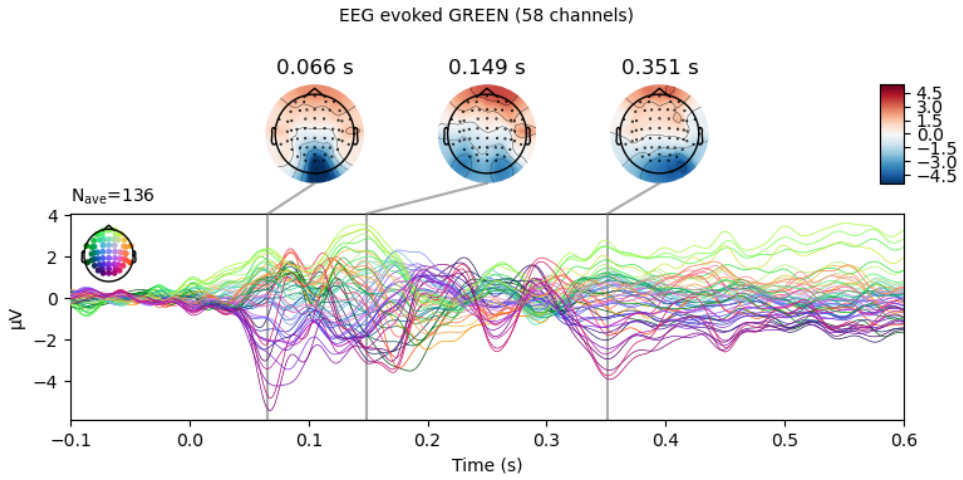

(b) A butterfly plot of the green evoked of all EEG channels used when recording Subject2.

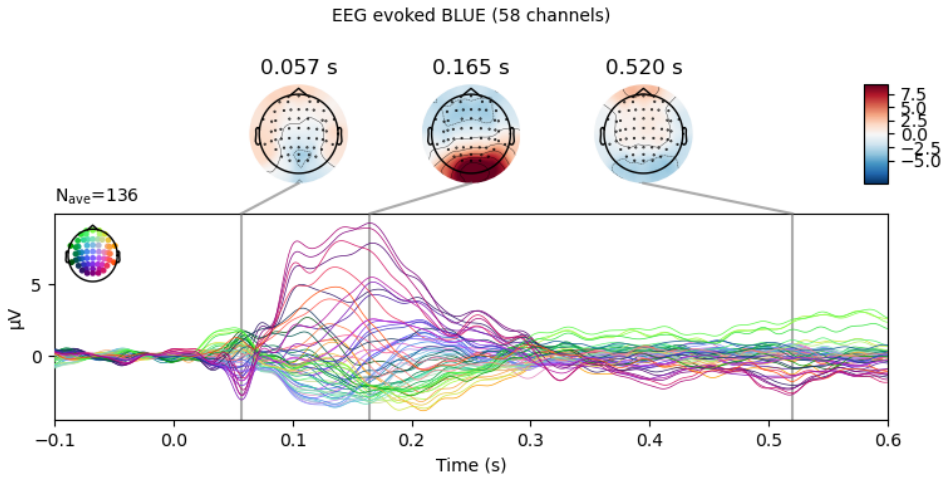

(c) A butterfly plot of the blue evoked of all EEG channels used when recording Subject2.

Figure 3.12: Butterfly plots for subject 2, session 2

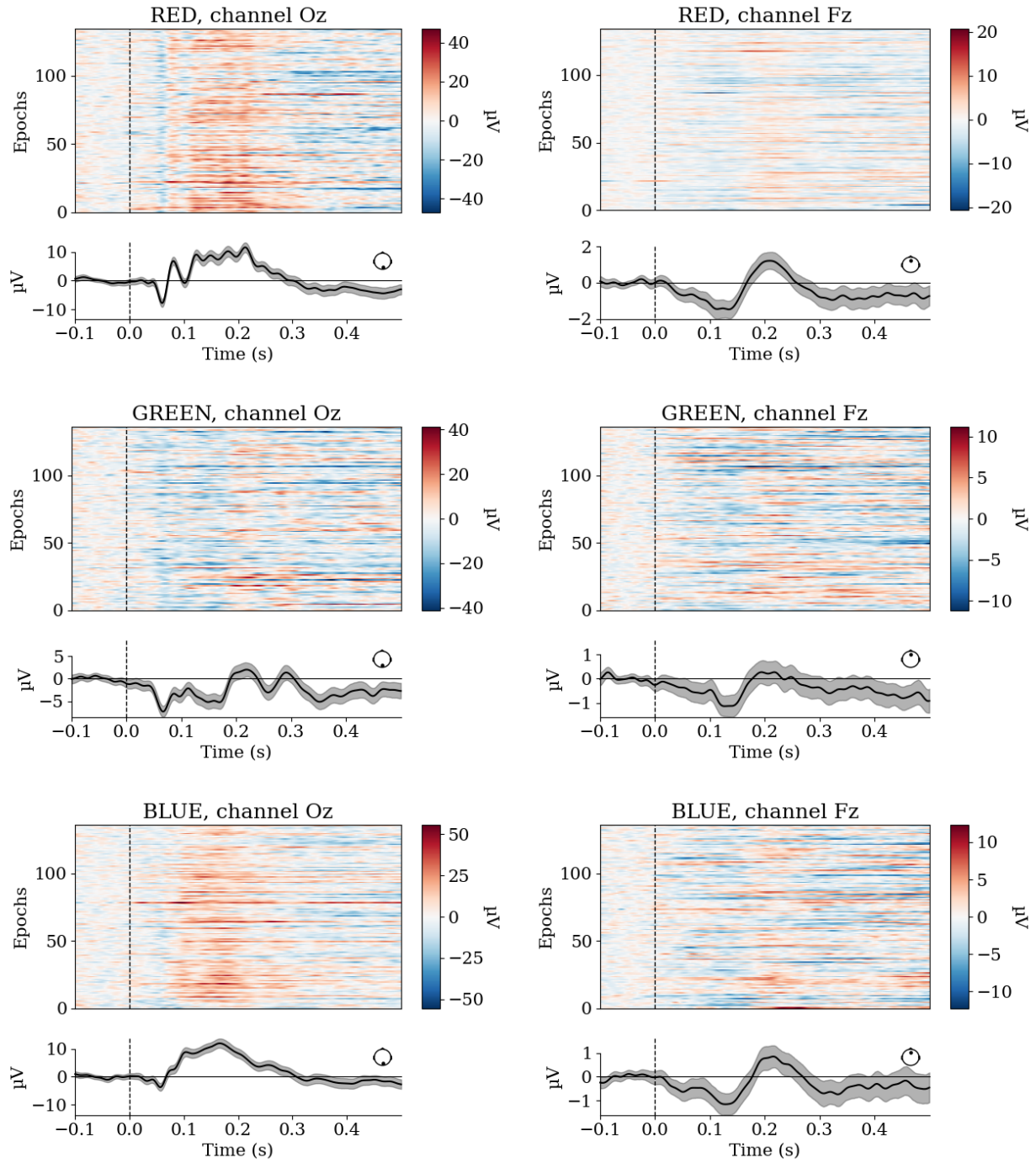

Figure 3.13: Plotted images for subject 2, session 2 from channels Oz and Fz. In the top plot, the amplitude of every epoch is plotted, and in the bottom, the average response is plotted. The x-axis represents time in both plots.

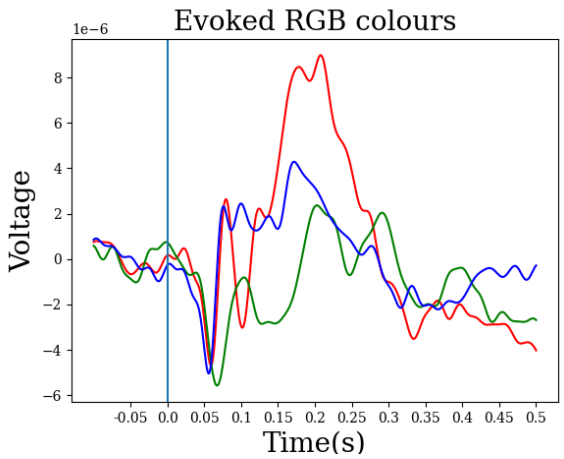

(a) Subject 2, session 1, channel POz

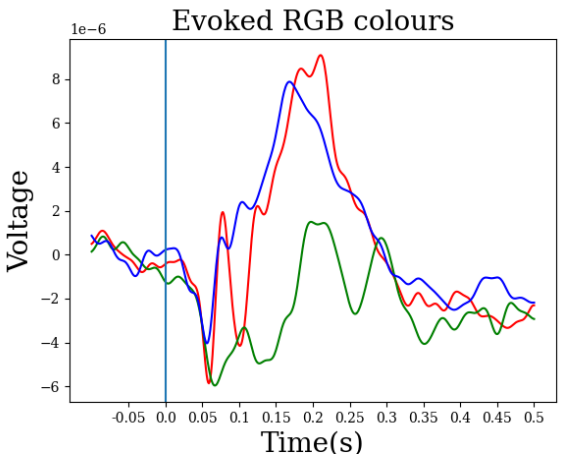

(b) Subject 2, session 2, channel POz

Figure 3.14: Cross-session evoked signals.

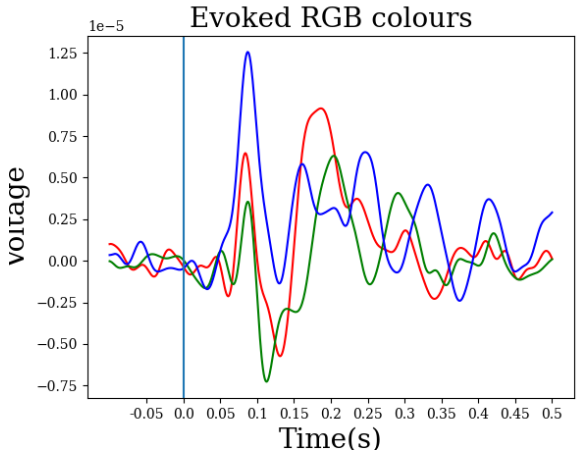

(a) Subject 7, session 2, channel POz

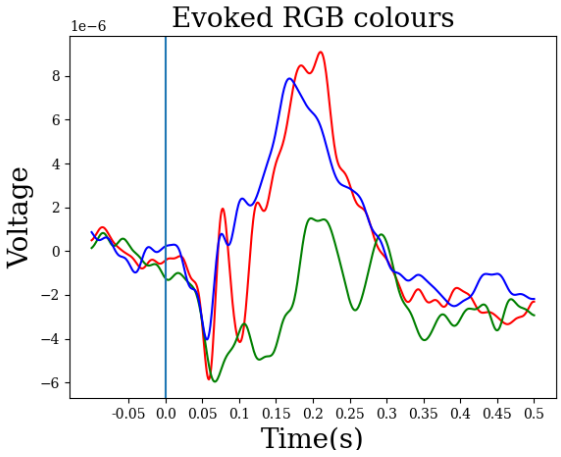

(b) Subject 2, session 2, channel POz

Figure 3.15: Cross-subject evoked signal

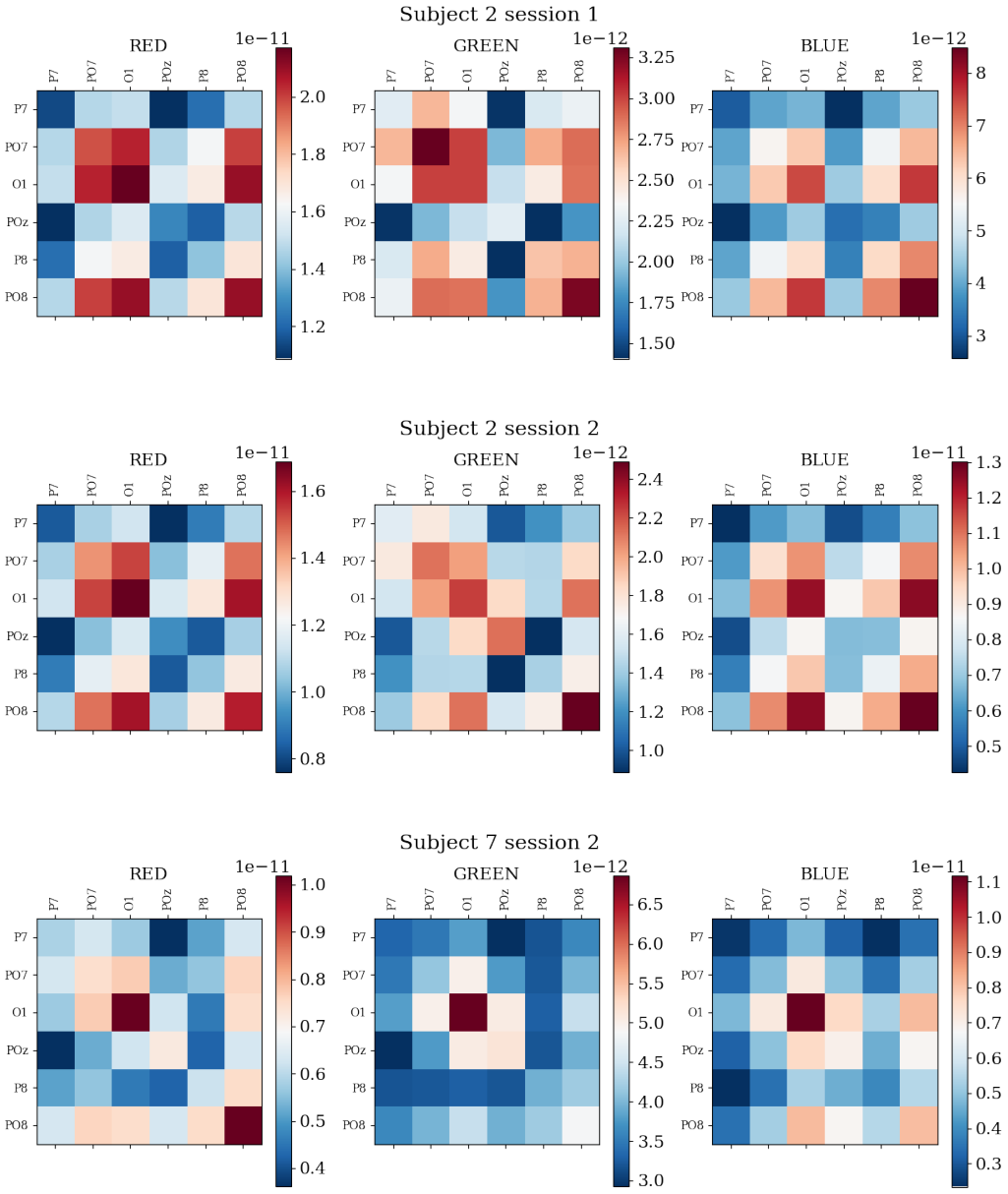

Figure 3.16: Covariance matrices for the evoked response to RGB stimuli for channels PO3, PO7, O1, POz, PO4 and PO8.

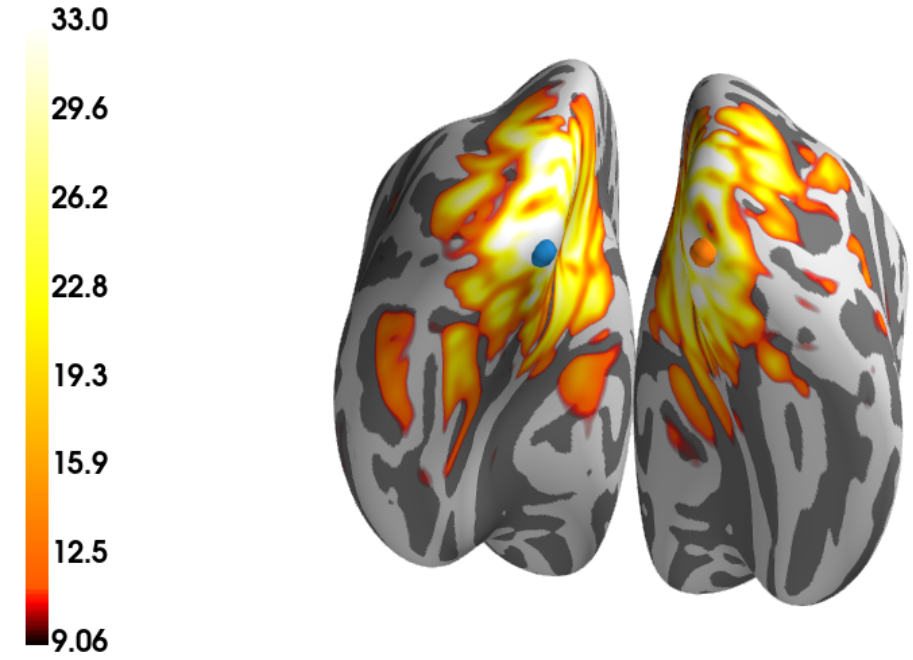

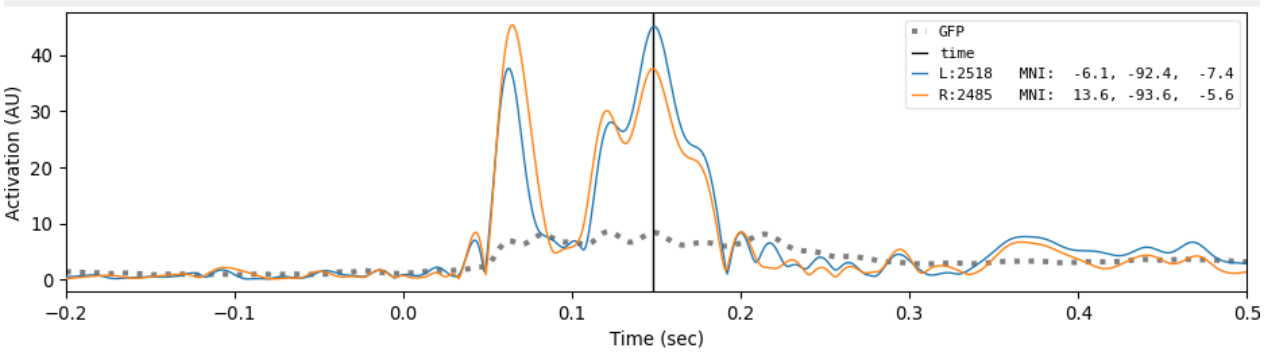

Figure 3.17: The activity of the brain in the source time course of the evoked red signal. This plot stems from subject 2 session 2.

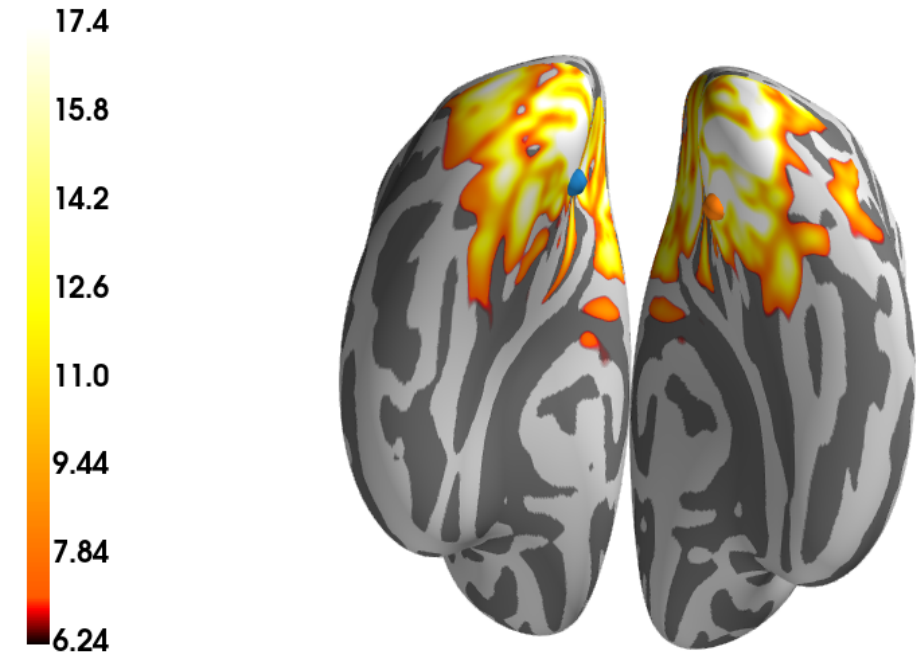

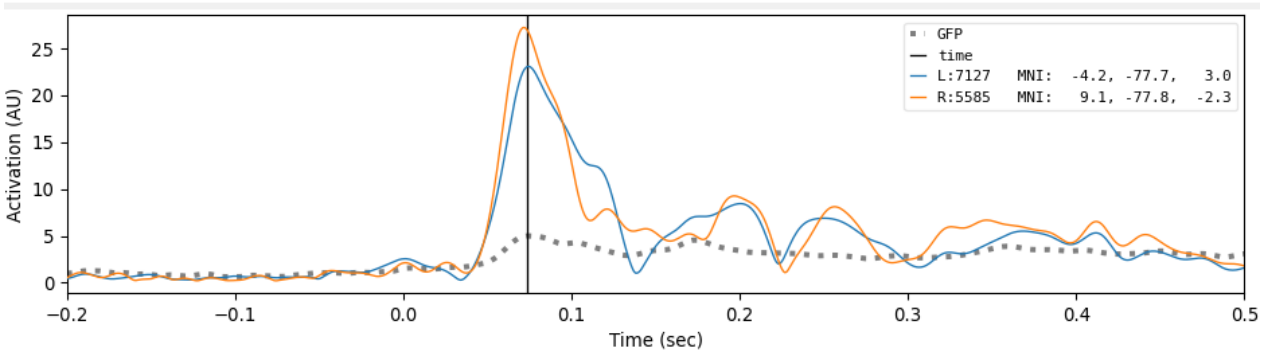

Figure 3.18: The activity of the brain in the source time course of the evoked green signal. This plot stems from subject 2 session 2.

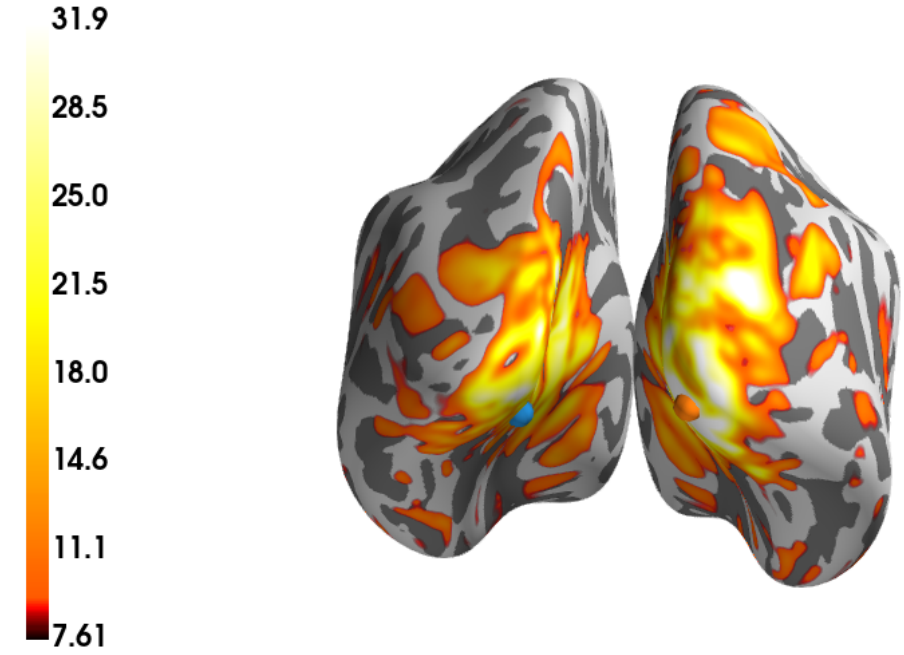

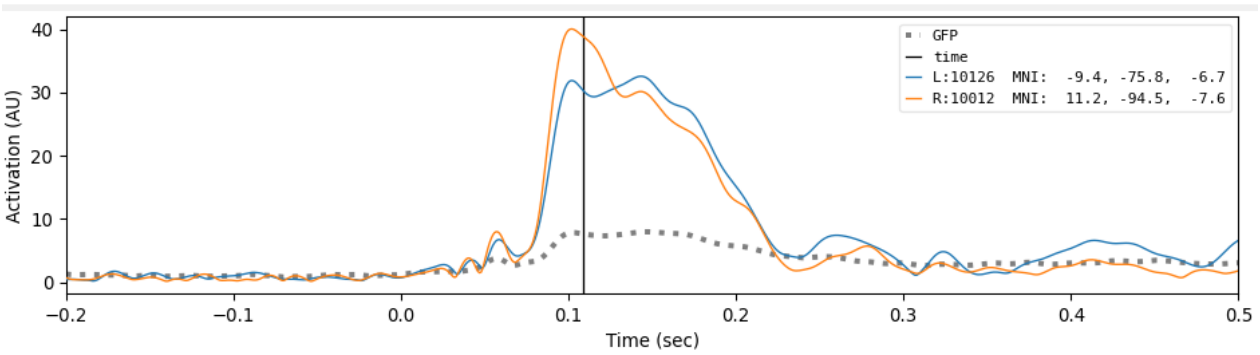

Figure 3.19: The activity of the brain in the source time course of the evoked blue signal. This plot stems from subject 2 session 2.

3.4 Data features

This section explores the features that best discriminate the RGB colours. These features are extracted from the signal and used as input to the classifiers in the next section.

3.4.1 Energy, Fractal and Statistical features

When extracting energy, fractal and statistical features from the EEG channels, the `MNE-Features` library [14] was used. This library extracts user-specified features from each channel in the recording. The plots in this section are just to illustrate the differences. The features that were used in the project has taken the energy, fractal dimensions, and statistical properties of each frequency from the continuous wavelet transform described in section 3.4.2 and in accordance with fig. 3.1.

Teager Kaiser Energy and DWT

The Teager Kaiser Energy Operator is defined as [37]:

$$\psi(g(t)) = \dot{g}(t) - g(t)\ddot{g}(t) \tag{3.6}$$

where $\dot{g}(t)$ and $\ddot{g}(t)$ are the first and second derivatives of $g(t)$, respectively.

The discrete wavelet transform (DWT) makes it possible to analyse a non-stationary signal in the time-frequency domain. It decomposes the signal into several levels, where each level contains the signal for a specific subset of frequencies. The DWT of a signal $g(t)$ is given by [37]:

$$DWT(m,n) = \int_{\infty}^{\infty} g(t) \frac{1}{\sqrt{|2^m|}} \varphi\Big(\frac{t-2^{mn}}{2^m}\Big) dt, \tag{3.7}$$

where 2^m is the translation parameter, 2^{mn} the dilation parameter and φ is the mother wavelet. In this project, the Daubechies wavelet with four vanishing moments (`db4`) wavelet was utilised.

This feature computed the Teager Kaiser Energy for each level of the DWT. The feature is visualised in fig. 3.20.

Fractal features

Fractal signals are signals that are similar at every scale. They can also be referred to as self-similar or scale-invariant. An object is fractal if it can be divided into statistically exact copies, and each shifting and scaling of the copy can make up the whole object [38]. An example of the fractal dimensions of the evoked signal for each colour can be viewed in fig. 3.21.

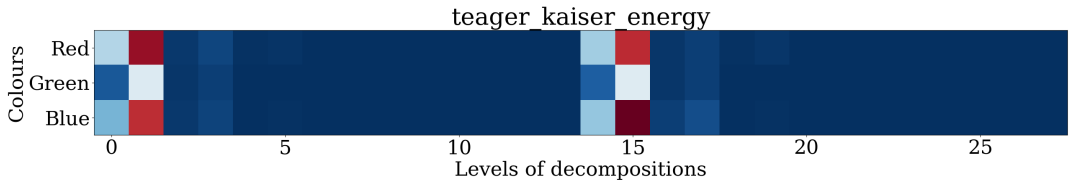

Figure 3.20: The Teager Kaiser Energy of the EEG source reconstructed evoked signal of subject 2 session 2.

Higuchi Fractal Dimension

The first step of Higuchi's algorithm for calculating fractal dimension in the time-domain is to divide the signal $(x(1), x(2), ..., x(N))$ into segments of k time series x_m^k as follows:

$$x_m^k = \left\{ x(m), x(m+k), x(m+2k), ..., x\left(m + \left\lfloor \frac{N-m}{k} \right\rfloor\right)\right\}, \qquad \text{for } m = 1, 2, ..., k \tag{3.8}$$

where k is the time interval between points, $\lfloor a \rfloor$ is the integer part of a, and m is the initial time. For every x_m^k that is created, the average length is computed as:

$$L_m(k) = \frac{\sum_{i=1}^{\lfloor (N-m)/k \rfloor} \left| x(m+ik) - (x(m+(i-1)k) \right| (n-1)}{\left\lfloor \frac{N-m}{k} \right\rfloor k} \tag{3.9}$$

The sum of the average lengths $L(k)$ is calculated as follows:

$$L(k) = \sum_{m=1}^{k} L_m(k). \tag{3.10}$$

The Fractal Dimension by the Higuchi algorithm is the slope of the least square best fit of the linear function through the data points $\left(\ln(L(k)), \ln(1/k)\right)$. [39]

Katz Fractal Dimension

The Katz algorithm for calculating the fractal dimension of a signal in the time-domain is:

$$KFD = \frac{\log_{10}(n)}{\log_{10}\left(\frac{d}{L}\right) + \log_{10}(n)}, \tag{3.11}$$

where L is the length of the signal, n is the number of steps in the curve, and d is the estimated diameter between the first point of the sequence (p_0) and the point furthest away. In other terms, $d = \max(\text{distance}(1, i))$, where i is the point with the largest distance to p_0. [39]

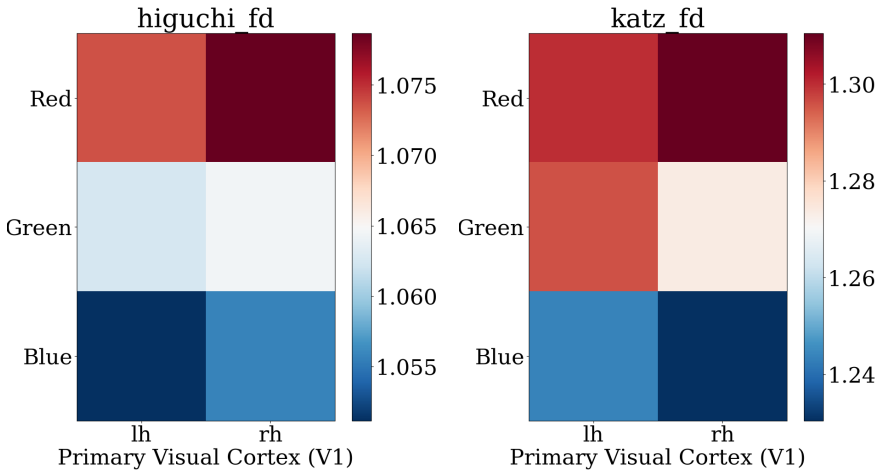

(a) Higuchi fractal dimension (b) Katz fractal dimension

Figure 3.21: The fractal dimensions of the EEG source reconstructed evoked signal of subject 2 session 2.

Statistical features

The maximum, minimum and median value of the signal were used as features. The skewness and kurtosis of the signal were also used. Skewness and kurtosis both describe the probability distribution of the signal. Skewness is a measure of the asymmetry of the distribution of the signal. If the skewness is zero, the data is normally distributed. If it is positive, the mass of the distribution is to the left and the right if it is negative. Kurtosis is a measure of the outliers. A high kurtosis corresponds to more extreme outliers. The statistical features are plotted in fig. 3.22

3.4.2 Continuous Wavelet Transform

The Continuous Wavelet Transform (CWT) is a decomposition of a signal where sections of the signal are compared with a wavelet. The CWT of a signal is found by the following steps:

1. A section of the signal is compared with a wavelet. The correlation between the wavelet and the section is calculated.

2. The wavelet is shifted to the next section of the signal, and the correlation is again calculated.

3. The correlation between the wavelet and all sections of the signal is calculated. Then, the wavelet is scaled, and the previous steps are repeated for the scaled wavelet.

4. This procedure is followed for all scales of the wavelet.

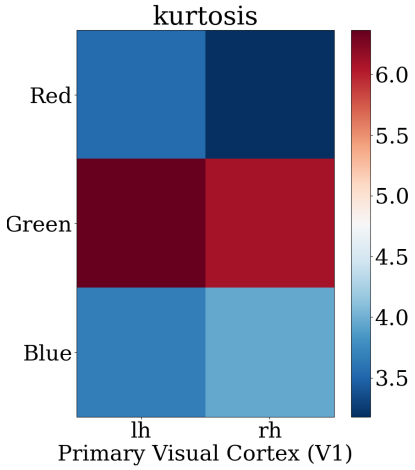

(a) Kurtosis

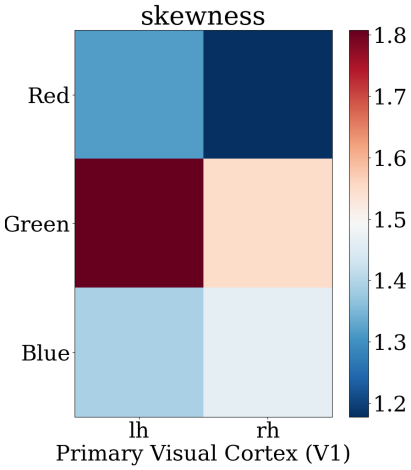

(b) Skewness

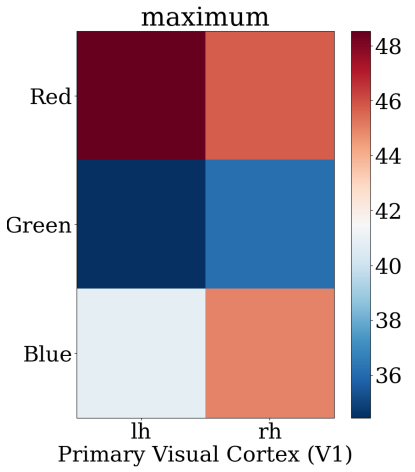

(c) Maximum

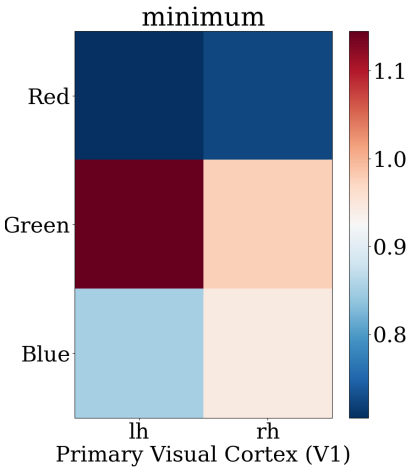

(d) Minimum

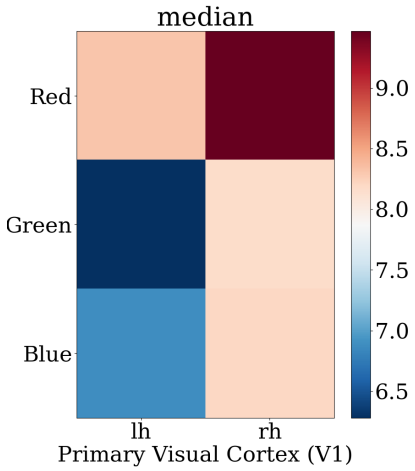

(e) Median

Figure 3.22: The statistical features of the EEG source reconstructed evoked signal of subject 2 session 2.

The following convolution expresses the calculation of the correlation:

$$CWT(a,b) = \frac{1}{|a|^{1/2}} \int_{-\infty}^{\infty} x(t)\psi\Big(\frac{t-b}{a}\Big)dt \tag{3.12}$$

where $x(t)$ is the signal, a is the scale, b is the shift and ψ is the wavelet applied, also called the mother wavelet.

In this thesis, the mother wavelet used was a complex Morlet wavelet. It was applied using the MNE time-frequency API, with a shape according to eq. (3.17), calculated as follows

$$\text{oscillation} = \exp(2j\pi ft) \tag{3.13}$$

$$\text{Gaussian envelope} = \exp\Big(\frac{-t^2}{2\sigma^2}\Big) \tag{3.14}$$

$$w(t,f) = \text{oscillation} * \text{Gaussian envelope} \tag{3.15}$$

The normalisation factor is given by

$$A = (\sqrt{0.5}\|w\|)^{\frac{-1}{2}} \tag{3.16}$$

and multiplied to the wavelet, giving the full expression

$$w(t,f) = A\exp(2j\pi ft)\exp\Big(\frac{-t^2}{2\sigma^2}\Big) \tag{3.17}$$

In this case, σ was given by $(n_c)/(2\pi f)$, number of cycles (n_c) were set to 0.5, the frequencies explored were $f = [2,5,8,11,14,17,20,23]$Hz. These frequencies include parts of the Delta and Beta bands and the entirety of the Theta and Alpha bands defined in section 2.1.3. An example of a Morlet wavelet used and a resulting average power plot is illustrated in Figure 3.23. The CWT constructed a 3rd-order tensor for each epoch: (8-channels, 8-frequencies, 400-timepoints).

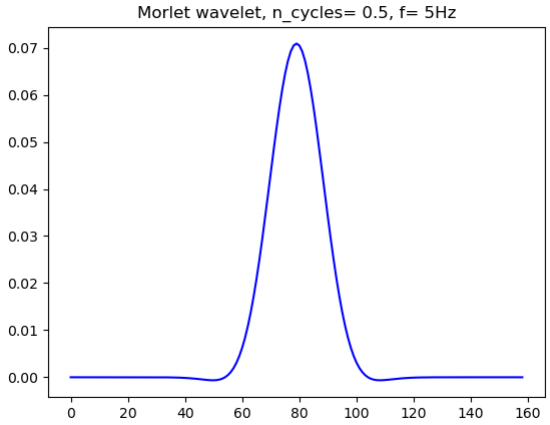

(a) An illustration of the Morlet wavelet

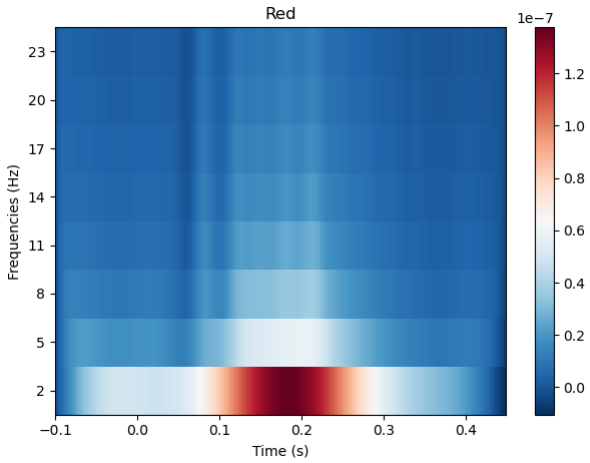

(b) The averaged power plot of a signal after applying CWT with Morlet wavelets similar to the one shown in a)

Figure 3.23: Morlet wavelet and power plot

3.4.3 Covariance matrix

In this project, a covariance matrix was used to calculate the similarities between time-frequency representations. After a signal was transformed by a CWT, the output was a 3rd-order tensor of shape (8, 8, 400) for each epoch. The input for most of the classifiers used in this thesis (e.g. Riemannian classifiers) require a 2-dimensional covariance matrix as input. The tensors were therefore reshaped into a matrix with shape (64, 400). It resulted in a (64, 64) covariance matrix used as a feature. The covariance matrix was calculated as in Equation (3.18):

$$\mathbf{CVM} = \begin{bmatrix} Cov((ch_1,2Hz),(ch_1,2Hz)) & \dots & Cov((ch_1,2Hz),(ch_8,23Hz)) \\ Cov((ch_1,5Hz),(ch_1,2Hz)) & \dots & Cov((ch_1,5Hz),(ch_8,23Hz)) \\ \vdots & \ddots & \vdots \\ Cov((ch_2,2Hz),(ch_1,2Hz)) & \dots & Cov((ch_2,2Hz),(ch_8,23Hz)) \\ Cov((ch_2,5Hz),(ch_1,2Hz)) & \dots & Cov((ch_2,5Hz),(ch_8,23Hz)) \\ \vdots & \ddots & \vdots \\ Cov((ch_8,23Hz),(ch_1,2Hz)) & \dots & Cov((ch_8,23Hz),(ch_8,23Hz)) \end{bmatrix} \tag{3.18}$$

where $Cov((ch_2,2Hz),(ch_1,2Hz))$ is the covariance between channel 2 with frequency decomposition 2 Hz, and channel 1 with frequency decomposition 2 Hz. The covariance is defined as

$$Cov(X,Y) = E[(X - E[X])(Y - E[Y])] \tag{3.19}$$

$$E[X] = \int_{-\infty}^{\infty} x f(x) \tag{3.20}$$

By design, the covariance matrix is symmetric, and if enough data is used to estimate it, it will also be positive definite [40]. The variance of each channel and frequency decomposition can be found on the diagonal of the matrix. A covariance matrix was calculated for each epoch.

3.5 Classifiers

This section[1] explains the methodology behind the classification algorithms used in this thesis. The purpose of the classifier is to predict the class correctly when given a set of data. The classes to predict in this project are red, green and blue, also known as the RGB colours. It is a multiclass problem, where the data given to the classifier are features extracted from EEG signals. In this project, Riemannian classifiers have been the main focus due to their generalisation capabilities, and high performance [7]. Only supervised methods were utilised, meaning that the training set of data had known classes, and the model was able to evaluate its own performance. It contrasts with unsupervised learning algorithms, where the data is categorised into classes based on similarities and differences without any knowledge of true classes. Both logistic regression and linear discriminant analysis with shrinkage were applied in combination with the Riemannian tangent space classifier.

3.5.1 Multiclass logistic regression

Logistic Regression (LR) is a machine learning algorithm that classifies data into categories. In this project a logistic regression algorithm from scikit-learn was used [15]. Since this is a supervised algorithm, a part of the data is first forwarded through the algorithm, then compared to the true classification. Afterwards, a loss function is calculated, and the algorithm is updated with parameters that reduce the loss for future classifications. Another part of the data is forwarded through the procedure again to enhance the algorithm further.

In order to classify data with logistic regression, the posterior probabilities need to be calculated. They are given by a softmax transformation of the features, and in [41] defined as:

$$p(\mathcal{C}_k|\phi) = y_k(\phi) = \frac{\exp(a_k)}{\sum_j \exp(a_j)}, \tag{3.21}$$

where $\mathcal{C}_k$ is the class k, ϕ is the feature vector and a_k is the activation, given by

$$a_k = \mathbf{w}_k^T \phi. \tag{3.22}$$

$\mathbf{w}_k$ is the parameter vector and represent the weight of each feature. When using the maximum likelihood to determine the weights $\{\mathbf{w}_k\}$, the derivatives of y_k with respect to all the activations a_j are required. They are found as

$$\frac{\partial y_k}{\partial a_j} = y_k(I_{kj} - y_j) \tag{3.23}$$

[1] Note that this is an updated version of the classification chapter in the authors' previous work in [1]

where I_{kj} are the elements of the identity matrix. The likelihood functions is given by

$$p\big(\mathbf{T}|\mathbf{w}_1,...,\mathbf{w}_K\big) = \prod_{n=1}^{N}\prod_{k=1}^{K} p\big(\mathcal{C}_k|\phi_n\big)^{t_{nk}} = \prod_{n=1}^{N}\prod_{k=1}^{K} y_{nk}^{t_{nk}} \tag{3.24}$$

where $y_{nk} = y_k(\phi_n)$, and $\mathbf{T}$ is an $N \times K$ matrix consisting of target variables with elements t_{nk}. The cross entropy loss function is obtained by taking the negative logarithm of the likelihood function (eq. (3.24)) [41]:

$$E(\mathbf{w}_1,...,\mathbf{w}_K) = -\ln p\big(\mathbf{T}|\mathbf{w}_1,...,\mathbf{w}_K\big) = -\sum_{n=1}^{N}\sum_{k=1}^{K} t_{nk}\ln y_{nk} \tag{3.25}$$

When the loss function was calculated, a limited-memory Broyden-Fletcher-Goldfarb-Shannon (lmbfgs) solver was used to recalculate the parameters of $\mathbf{w}$ to minimise the loss.

3.5.2 Linear Discriminant Analysis

The basic idea behind the Linear Discriminant Analysis (LDA) is to find the best linear transformation to discriminate between classes [42]. The classification can be performed in a transformed space such as the Euclidean and Riemannian tangent spaces. LDA can be used as a feature reduction technique and classifier but have only been applied as a classifier in the experiments conducted in this thesis. The solver used is a least-square solver that finds the x that minimise c in eq. (3.26)[15], where b and A denote the means of all classes and the covariance matrices for all classes, respectively. LDA is based on the assumption that the covariance for all the classes is identical [43]. Predictions based on LDA are obtained from Bayes' rule for each training example (see eq. (3.27)), and the class k with the highest probability is chosen.

$$c = \|b - Ax\| \tag{3.26}$$

$$P(y = k|x) = \frac{P(x|y = k)P(y = k)}{P(x)} \tag{3.27}$$

sLDA

The LDA algorithm was further improved by Ledoit and Wolf in 2003 in [44]. The shrinkage technique is used as a means of regularising covariance matrices. The shrinkage transforms coefficients from the extremes towards more central values, thereby reducing estimation errors in the most sensitive areas. Therefore, it is beneficial when the training set has fewer samples than the number of features, and it improves the generalisation of the classifier.

3.5.3 Riemannian geometry-based classifiers

A topological manifold is a space that looks like a plane locally. A Riemannian manifold is a real smooth differential manifold, where each tangent space is equipped with an inner product. In order to measure distances and angles on a manifold, it has to be Riemannian. [45]
The Riemannian geometry-based classifiers are matrix classifiers. These methods of classifying utilize the Riemannian distance between symmetric positive-definite (SPD) matrices [46].

Riemannian Geometry

In order to classify in Riemannian space, we need a distance (also known as metric) and a mean function.

☞ **Metric (or distance)** is a non-negative, symmetric function that defines a distance between each pair of elements of a set. It is only equal to zero if the two elements are equal, and it obeys the triangle inequality. A set provided with a metric, is known as a **metric space** [47]

Mean (mono-dimensional), as defined in [47]

Let (S,d) be the metric space of positive real numbers endowed with metric d and $c_1,...,c_K$ be a set of K points in it. The **mean** of the set $c_1,...,c_K$ is a point x that minimises the dispersion $\frac{1}{K}\sum_k d^2(x,c_k)$.

Euclidean distance and mean

A simple example of a metric is the Euclidean distance. It is defined as

$$d_E(a,b) = \left|a-b\right|, \tag{3.28}$$

where a and b are points on the metric space S. The corresponding mean is the point m that solves the following minimisation:

$$\underset{m}{\operatorname{argmin}} \frac{1}{K}\sum_k d_E^2(m,c_k) = \underset{m}{\operatorname{argmin}} \frac{1}{K}\sum_k \left|m-c_k\right|^2 \tag{3.29}$$

This minimisation of the sample variance (the dispersion around the mean) gives the arithmetic mean:

$$m = \frac{1}{K}\sum_k c_k \tag{3.30}$$

The arithmetic mean is an appropriate descriptor of the expected value of the variance in symmetric distributions (e.g. Gaussian distributions) only. [47]

Geometric distance and mean

Another metric is the geometric[2] distance. It is defined as:

$$d_G(a,b) = \left|\log a - \log b\right| = \left|\log \frac{a}{b}\right| \tag{3.31}$$

The switch to the logarithmic transformed variance is common practice in the BCI field according to [47]. In contrast to the Euclidean distance (eq. (3.28)), the geometric distance (eq. (3.31)) is scale invariant and invariant under diversion. It is scale invariant because

$$d_G(xa,xb) = d_G(a,b), \quad \forall \quad a,b,x > 0 \tag{3.32}$$

and invariant under inversion since

$$d_G(a^{-1},b^{-1}) = d_G(a,b), \quad \forall \quad a,b > 0. \tag{3.33}$$

The geometric mean is the point g that solves the minimisation problem

$$\underset{g}{\operatorname{argmin}} \frac{1}{K}\sum_k d_G^2(g,c_k) = \underset{g}{\operatorname{argmin}} \frac{1}{K}\sum_k \left|\log g - \log c_k\right|^2. \tag{3.34}$$

The solution to eq. (3.34), and the geometric mean is:

$$g = \sqrt[K]{c_1 \cdot c_2 \cdot \ldots \cdot c_K} = \exp\left(\frac{1}{K}\sum_k \log c_k\right) \tag{3.35}$$

The geometric mean, which is inherited from the geometric distance, is an appropriate descriptor of the expected value of the variance in both symmetric and chi-squared distributions. When outliers are present in the data, the geometric mean deviates less from the distribution center than the Euclidean mean. [47]

[2] Also known as the log-Euclidean or hyperbolic distance.

Riemannian distance and mean

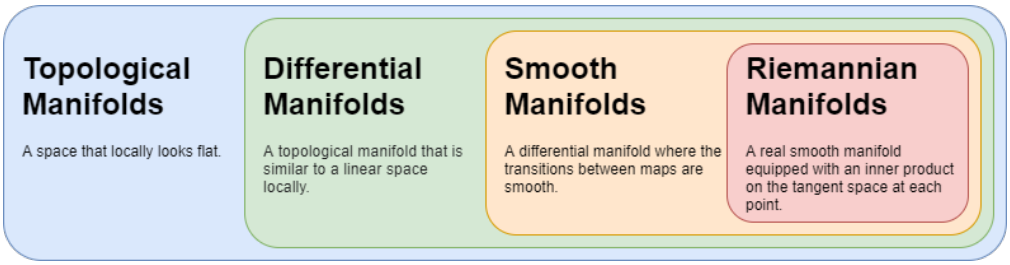

Figure 3.24: The types of manifolds, as described in [45]. The manifold inherits the characteristics of the manifolds to its left.

The set S of symmetric positive definite matrices is a differential manifold (see fig. 3.24), meaning that it is similar to a flat, linear space locally (see fig. 3.28). A tangent space is the space of SPD matrices at a point $\mathbf{P}$ on the manifold. As can be seen in fig. 3.24, a Riemannian manifold is a smooth manifold with an inner product on the tangent space at each point. The inner product at a point $\mathbf{P}$ is

$$\langle \mathbf{A}, \mathbf{B} \rangle_{\mathbf{P}} = \mathrm{tr}(\mathbf{P}^{-1}\mathbf{A}\mathbf{P}^{-1}\mathbf{B}) \tag{3.36}$$

where tr$(\cdot)$ is the trace operator. The norm associated with the inner product is

$$\|A\|_{2,\mathbf{P}} = \left\|\mathbf{P}^{-1}\mathbf{A}\right\|_2^2 = \left\|\mathbf{P}^{-1/2}\mathbf{A}\mathbf{P}^{-1/2}\right\|_2^2 \tag{3.37}$$

Equipped with the inner product (eq. (3.36)), it is possible to compute the length of a curve in the space of covariance matrices on the manifold. Given two symmetric positive matrices $\mathbf{C_1}$ and $\mathbf{C_2}$ on the manifold, there are several curves passing through the two points. The geodesic curve is the unique curve of minimal length that runs through these points. Because the manifold consists of symmetric positive matrices with an inner product on the tangent space a geodesic exists for any pair of points on the manifold. The Riemannian distance (δ_G) is defined as the length of the geodesic between $\mathbf{C}_1$ and $\mathbf{C}_2$:

$$\delta_G(\mathbf{C}_1, \mathbf{C}_2) = \left\|\mathrm{Log}(\mathbf{C}_1^{-1/2}\mathbf{C}_2\mathbf{C}_1^{-1/2})\right\|_F = \sqrt{\sum_{n=1}^{N} \log^2 \lambda_n} \tag{3.38}$$

where Log$(\cdot)$ is the matrix logarithm and λ_n are the N eigenvalues of $\mathbf{C}_1^{-1/2}\mathbf{C}_2\mathbf{C}_1^{-1/2}$. The Riemannian distance is invariant under congruence and invariant under inversion, which means that

$$\delta_G(\mathbf{X}\mathbf{C}_1\mathbf{X}^T, \mathbf{X}\mathbf{C}_2\mathbf{X}^T) = \delta_G(\mathbf{C}_1, \mathbf{C}_2) \tag{3.39}$$

and

$$\delta_G(\mathbf{C}_1^{-1}, \mathbf{C}_2^{-1}) = \delta_G(\mathbf{C}_1, \mathbf{C}_2). \tag{3.40}$$

Mean (multi-dimensional), as defined in [47]

Let $(\mathbf{S}_{++}(N), \delta)$ be the metric space of positive matrices endowed with metric δ and $\{\mathbf{C}_1, ..., \mathbf{C}_K\}$ be a set of K points in it. If there exists a unique point $\mathbf{X}$ for which the dispersion $\frac{1}{K}\sum_{k=1}^{K} \delta^2(\mathbf{C}_k, \mathbf{X})$ is minimal, then $\mathbf{X}$ is the mean of the points $\{\mathbf{C}_1, ..., \mathbf{C}_K\}$.

The geometric mean with the Riemannian metric δ_G yields the minimisation problem

$$\underset{G}{\operatorname{argmin}} \frac{1}{K} \sum_k \delta_G^2(\mathbf{C}_k, \mathbf{G}_m) \tag{3.41}$$

The invariance properties of δ_G guarantees that the geometric mean $\mathbf{G}_m$ exists and is unique, and ensures that the Riemannian[3] mean $\mathbf{G}_m$ has the properties congruence invariance and self duality. From the congruence invariance, it follows that

$$\mathbf{G}_m(\mathbf{X}\mathbf{C}_1\mathbf{X}^T, ..., \mathbf{X}\mathbf{C}_K\mathbf{X}^T) = \mathbf{X}\mathbf{G}_m(\mathbf{C}_1, ..., \mathbf{C}_K)\mathbf{X}^T \tag{3.42}$$

and the self-duality gives the following equality:

$$\mathbf{G}_m(\mathbf{C}_1^{-1}, ..., \mathbf{C}_K^{-1}) = (\mathbf{G}_m(\mathbf{C}_1, ..., \mathbf{C}_K))^{-1} \tag{3.43}$$

Unlike the arithmetic mean, the Riemannian mean has the determinant identity property, which means that

$$\det(\mathbf{G}_m(\mathbf{C}_1, ..., \mathbf{C}_K)) = \mathbf{G}_m(\det(\mathbf{C}_1), ..., \det(\mathbf{C}_K)). \tag{3.44}$$

[47]

The common concept of Riemannian geometry-based classifiers is that they utilize the multivariate nature of EEG recordings. Instead of representing the signal as a vector or a scalar, the variance and covariance of the channels in an epoch are represented in a covariance matrix. These matrices are then considered in a Riemannian manifold, where a metric, e.g. geodesic distance, is used to classify the epochs.

Minimum distance to mean

Minimum distance to mean (MDM) utilizes Riemannian distances between covariance matrices to classify each new epoch. Covariance matrices for each epoch are displayed as points on

[3] Also known as the Cartan, Karcher, Fréchet or geometric mean, or the center of mass of $\{\mathbf{C_1}, ..., \mathbf{C_K}\}$

the Riemannian manifold, as shown in fig. 3.25. The epochs in the training dataset are averaged to yield a category average (see fig. 3.26). When a never-before-seen epoch is classified, it is put in the category of the mean with the smallest Riemannian distance to itself [48]. This method has some limitations. For example, it does not take the variance of the class into account, which means that noise and other non-class related information can cause a significant distance between two matrices [46]. The method is described in alg. 1.

Algorithm 1: MDM classification [46]

Input: Ω a set of m SPD matrices $P_i \in P(n)$
Input: $\omega_i \in \{1,2\}$
Input: P_x a SPD matrix of unknown class
Output: ω_x the estimated class of test covariance matrix P_x
1: $P_{\Omega_1} = \mathfrak{G}(P_i)$ with $\{i|\omega_i = 1\}$ { Riemannian mean for class 1}
2: $P_{\Omega_2} = \mathfrak{G}(P_i)$ with $\{i|\omega_i = 2\}$ { Riemannian mean for class 2}
3: $d = \delta(P_x, P_{\Omega_1}) - \delta(P_x, P_{\Omega_2})$
4: **if** $d \leq 0$
5: $\quad \omega_x = 1$
6: **else**
7: $\quad \omega_x = 2$
8: **return** ω_x

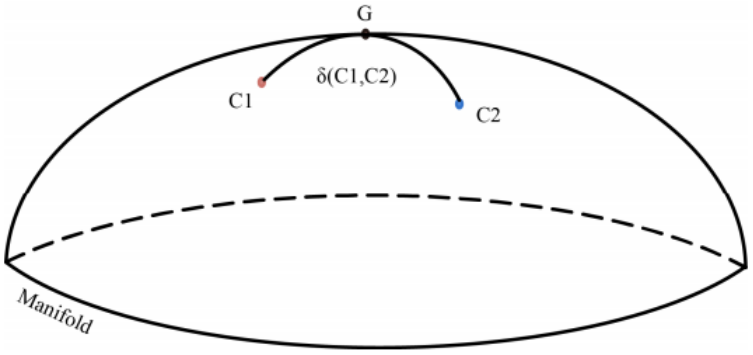

Figure 3.25: Covariance matrices represented as points on a Riemannian manifold. [48]

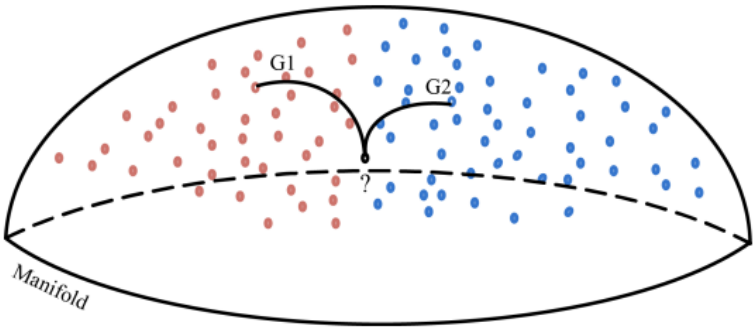

Figure 3.26: The covariance matrix of a never before seen epoch (marked '**?**') is classified in the category of the nearest category mean (marked '**G1**' or '**G2**') [48]. To relate this figure to alg. 1, $G_1 = P_{\Omega_1}$, $G_2 = P_{\Omega_2}$ and **?** $= P_x$.

Minimum Distance to Mean with geodesic filtering (FgMDM)

In order to overcome the limitation of the Riemannian MDM classifier, it was proposed in [46] to filter over the covariance matrices. Using an extension of the Linear Discriminant Analysis, the supervised FGDA (Fisher Geodesic Discriminant Analysis) algorithm [46], the method filter the data to remove irrelevant information. After projecting all covariance matrices to the tangent space, the FGDA algorithm maximises the scatter between classes while minimising the scatter within classes. The filters are then applied to the data. Finally, the LDA components are applied to the data, and the data is mapped back using the exponential operator. It is also possible to classify directly in the tangent space without mapping the data back to its original space. That is the topic of section 3.5.3.

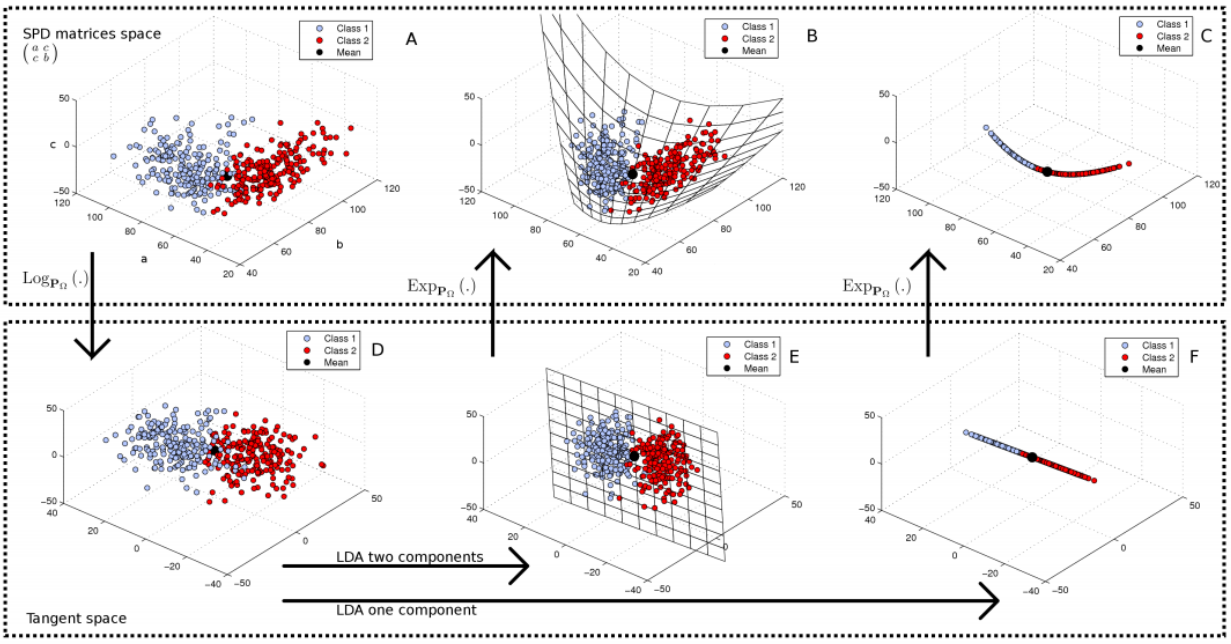

Figure 3.27: Riemannian Minimum Distance to Mean with Geodesic Filtering [46]. The data (fig A) is projected to the tangent space in fig D. After applying either one (fig F) or two (fig E) LDA components, the data is mapped back to the matrices space (fig B and fig. C).

Tangent Space

Classification algorithms like LDA, SVM and LR cannot be implemented directly in a Riemannian manifold. However, they can classify in the Tangent space of the geometric mean of all the epochs. Every Riemannian manifold contains a pair of mappings transporting points from the manifold to a tangent space and vice versa [45]. Therefore, the covariance matrix of each epoch can be mapped onto this tangent space. This method can be found in alg. 2. After the covariance matrix for each epoch in the training dataset was mapped to the tangent space, LR and LDA were used to classify the points relating to the covariance matrices in the tangent space. The upper(·) operator vectorizes the upper triangle of a symmetric matrix [49].

Algorithm 2: Tangent space mapping of covariance matrices [49]

Input: a set of I SPD matrices $P_i \in P(n)$
Output: a set of I vectors S_i
1: $P_{\mathfrak{G}} = \mathfrak{G}(P_i, i = 1...I)$ { Compute the Riemannian mean of the whole set }
2: for $i = 1$ to I do
3: $\quad S_i = \mathrm{upper}(P_{\mathfrak{G}}^{-\frac{1}{2}} \log_{P_{\mathfrak{G}}}(P_i) P_{\mathfrak{G}}^{-\frac{1}{2}})$
4: return S_i

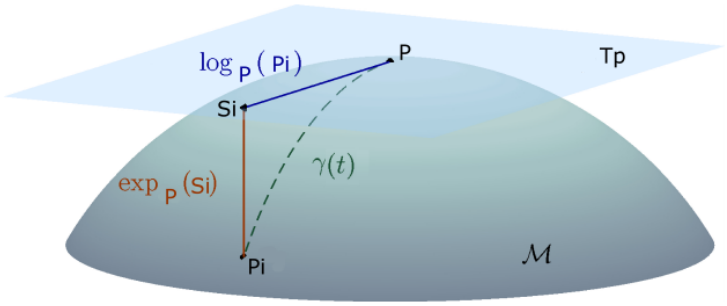

Figure 3.28: The tangent space (T_p) of a Riemannian manifold ($\mathscr{M}$)[46]. Relating this figure to alg. 2, $P = P_{\mathfrak{G}}$ and $S_i = S_i$

3.6 Transfer Learning

3.6.1 Motivation

Recording enough data to create an accurate BCI model can be both time and energy-consuming. When using a dataset for training and testing machine learning algorithms, it is assumed that the data used has the same feature space and the same probability distribution. It is usually not the case for brain-computer interfaces [7]. A change in data distribution usually occurs when a subject records data in several sessions at different times. The impedance and the position of the electrodes will inevitably vary from one session to another. For a BCI model to have any practical use, a new dataset must be recorded, and a new BCI model made every time the system is applied. It is impractical and motivates finding a way to reuse previous recordings.

From the analysis performed in section 3.3, it is evident that the similarities in signals are strongest cross sessions. For this reason, transfer learning cross sessions have been the focus of this section.

From observing the dataset used in this thesis, the change from session to session is usually no more than a shift in the data, while the pattern does not differ dramatically. It is illustrated in fig. 3.14. The data between subjects differ widely, also illustrated in fig. 3.14. These similarities and differences are additionally illustrated in the covariance matrices in fig. 3.16. For this reason, the authors of this thesis have focused on applying transfer learning cross sessions only.

3.6.2 Robustness and generalisation capabilities of Riemannian classifiers

As mentioned in section 2.3, an EEG recording is often contaminated with noise. It motivates the use of source separation techniques, where the measurement from the sensor is decomposed into source and noise. The noise is disregarded, and the source is fed through the BCI system. As mentioned in section 3.2, the EEG potentials can be described as a linear mixture of brain sources (see eq. (3.2) and eq. (3.3)), a simple forward model can be written as

$$\mathbf{x}(t) = \mathbf{A}\mathbf{s}(t), \tag{3.45}$$

where $\mathbf{x}(t)$ is the EEG signal, $\mathbf{s}(t)$ is the sources and $\mathbf{A}$ is an assumed invertible mixing matrix. The covariance matrices that are recorded at the sensors can therefore be expressed as

$$\mathbf{C}_1 = \mathbf{A}\mathbf{S}_1\mathbf{A}^T \qquad \text{and} \qquad \mathbf{C}_2 = \mathbf{A}\mathbf{S}_2\mathbf{A}^T. \tag{3.46}$$

Due to the congruence invariance property (eq. (3.39)), if the number of electrodes is the same as the number of sources, then

$$\delta_G(\mathbf{S}_1, \mathbf{S}_2) = \delta_G(\mathbf{A}\mathbf{S}_1\mathbf{A}^T, \mathbf{A}\mathbf{S}_2\mathbf{A}^T) = \delta_G(\mathbf{C}_1, \mathbf{C}_2). \tag{3.47}$$

In other words, the Riemannian distance between a pair of covariance matrices is the same in the sensor and source space when the dimensions of the spaces are equal. Even when the choice of number of components in the source space is less than the number of sensors, it is possible to find a projection that increases the separation of the classes. [47].

In EEG recordings, the difference in position and impedance of the electrodes across sessions leads to a mixing matrix that differs from session to session, for the same subject. If $\mathbf{S}_i$ and $\mathbf{S}_j$ are covariance matrices of two trials from the source space in the same sessions, then $\mathbf{C}_i = \mathbf{A}\mathbf{S}_i\mathbf{A}^T$ and $\mathbf{C}_j = \mathbf{A}\mathbf{S}_j\mathbf{A}^T$ are the corresponding covariance matrices in the sensor space. From another session, the source matrices $\mathbf{S}_i$ and $\mathbf{S}_j$ are the same, but the mixing matrix has changed due to the changes in position and impedance of the sensors. The mixing matrix for the second session is denoted $\tilde{\mathbf{A}}$, thus the covariance matrices in the sensor space are $\mathbf{Q}_i = \tilde{\mathbf{A}}\mathbf{S}_i\tilde{\mathbf{A}}^T$ and $\mathbf{Q}_j = \tilde{\mathbf{A}}\mathbf{S}_j\tilde{\mathbf{A}}^T$. The Riemannian distance between the covariance matrices in the source space are equal for both sessions, as shown:

$$\delta_G(\mathbf{C}_i, \mathbf{C}_j) = \delta_G(\mathbf{A}\mathbf{S}_i\mathbf{A}^T, \mathbf{A}\mathbf{S}_j\mathbf{A}^T) = \delta_G(\mathbf{S}_i, \mathbf{S}_j) = \delta_G(\tilde{\mathbf{A}}\mathbf{S}_i\tilde{\mathbf{A}}^T, \tilde{\mathbf{A}}\mathbf{S}_j\tilde{\mathbf{A}}^T) = \delta_G(\mathbf{Q}_i, \mathbf{Q}_j) \tag{3.48}$$

In cross-subject transfer learning, the source covariance matrix is different, and therefore the performance will not be as high when classifying across subjects.

Chapter 4

Results

All signals were preprocessed using a filter, average referencing, rejection criteria and shifting as described in section 3.1.4. After an analysis of the signals similar to the one described in section 3.3, the time interval with the most colour specific characteristics seemed to be from 50ms to 450ms after stimuli, and all epochs were cropped accordingly. For feature extraction, the signals were time-frequency decomposed using CWT with a Morlet wavelet as the mother wavelet, described in section 3.4.2. When classifying with a Riemannian method, described in section 3.5.3, the decompositions were used as input for a covariance matrix as described in section 3.4.3. When classifying with Linear Discriminant Analysis, only the real part of the decompositions was used, and the features described in section 3.4.1 were used as input for the classifier. The different combinations of preprocessing, features and classifiers are summarised in table 4.2. The parameters are shown in table 4.1. The channels used are marked with red in fig. 3.4. The method for extracting sources from the EEG signal has only been used to achieve the results in section 4.2.1. All other results are from classifying EEG signals.

4.1 About the results

There are four tables of results for this dataset. They are the results for classifying between three classes based on features from the EEG signals, three classes based on features from the EEG source reconstructions, two classes based on features from the EEG signals, and the results from transfer learning. All of which are further explained below. The accuracy and standard deviation are measured between 0 and 1, 1 being the highest accuracy possible. A result for receiver operating characteristics (ROC) is also included for three subjects in section 4.2.3 to illustrate the models' ability to recognise the colours.

None of the parameters has been specifically chosen or tuned for each subject and session. All results are based on a EEG signal model with the parameters listed in Table 4.1. Those are the

parameters that gave the best average result.

Table 4.1: Parameters

Filter	0.1 - 40 Hz
Reject criteria	EEG: 120e-6, EOG: 150e-6
Baseline	-0.1 - 0.0 sec
Crop	0.05 - 0.45 sec
Channels	P7, PO7, O1, POz, Oz, PO8, P8, O2
Frequencies used in Morlet decomposition	2,5,8,11,14,17,20,23
Number of cyclet in morlet wavelet	0.5

Table 4.2: Abbreviations in tables with results

Abbreviation	**Preprocessing**	**Features**	**Classifier**
TS+sLDA	Filter, shift[1]	CWT[2] + CVM[3]	sLDA[4]
TS+LR	Filter, shift [1]	CWT [2] + CVM [3]	LR [4]
FgMDM	Filter, shift [1]	CWT [2] + CVM [3]	FgMDM
stat+sLDA	Filter, shift [1], PT[5], SS[6]	EFS [7]	sLDA

4.1.1 Cross validation

To avoid over-fitting the classifier's parameters, the EEG signal model is tested on never-before-seen data. In other words, the dataset is split into a training set, used to train the classifier, and a test set, which is used when evaluating the data. When tuning the EEG signal model parameters to increase the test set's performance, information about the test set is learned. It can lead to a model that performs well on the test set but not on new data. This is known as over-fitting and leads to a poor generalisation of the EEG signal model. To avoid this, a part of the training data is used to make a new dataset, known as the validation set. The dataset used in this thesis was small and had few epochs of each colour. Splitting the dataset into three smaller sets would drastically reduce the number of epochs available for training a model. It could lead to an under-fitted model that depends highly upon which epochs make up which set. For this reason, the K-Fold cross-validation is used. The K-Fold cross-validation splits the training set

[1] Described in section 3.1.4
[2] Continuous wavelet transformation, described in section 3.4.2
[3] Covariance matrix, described in section 3.4.3
[4] in the Riemannian tangent space, see section 3.5.3
[5] Power transformer
[6] Standard Scaler
[7] Energy, Fractal and Statistical features described in section 3.4.1

into K divisions. For each division, or fold, the model is using $K-1$ folds as training data, and the least one as validation [15]. The performance of the classifier is the mean of the accuracy computed for each fold. The standard deviation increases with the number of folds. In these results, $K = 10$ because it is a good trade-off between accuracy and deviation.

4.1.2 Receiver operating characteristic

ROC stand for Receiver operating characteristics. It operates on two classes, negative and positive, but the visualisation (see fig. 4.1) only include true positives and false positives. False positives are plotted along the x-axis and true positives along the y-axis. Both axes run from 0.0 to 1.0, and the point (0.0, 1.0) is the best possible score. It indicates that all instances belonging to the class positive have been classified as such, and none of the instances belonging to class negative has been classified as positive. Thus, the point (1.0, 1.0) indicates that all class positive or negative instances have been classified as positive. Additionally, the classification threshold is included defining how sure the classifier must be to classify as positive. In fig. 4.1 the threshold is marked as points on the curve. A threshold of 0.8 provides no false positives but only a few true positives as well. While a more liberal threshold of 0.54 produces a much larger share of true positives and a few false positives. When the threshold increases, both true and false positives will always reach 1.0. Therefore, how well the classifier performs is often measured by how fast the ROC curve reaches a high value for true positives. In other words, how close the area under the curve is to 1.0. [50]

In section 4.2.3, the ROC curves for three subjects are plotted. Each colour has individually been assigned the class positive, and the performance on all colours has been plotted in the same plot. ROC curves for all subjects can be found in appendix B.3.

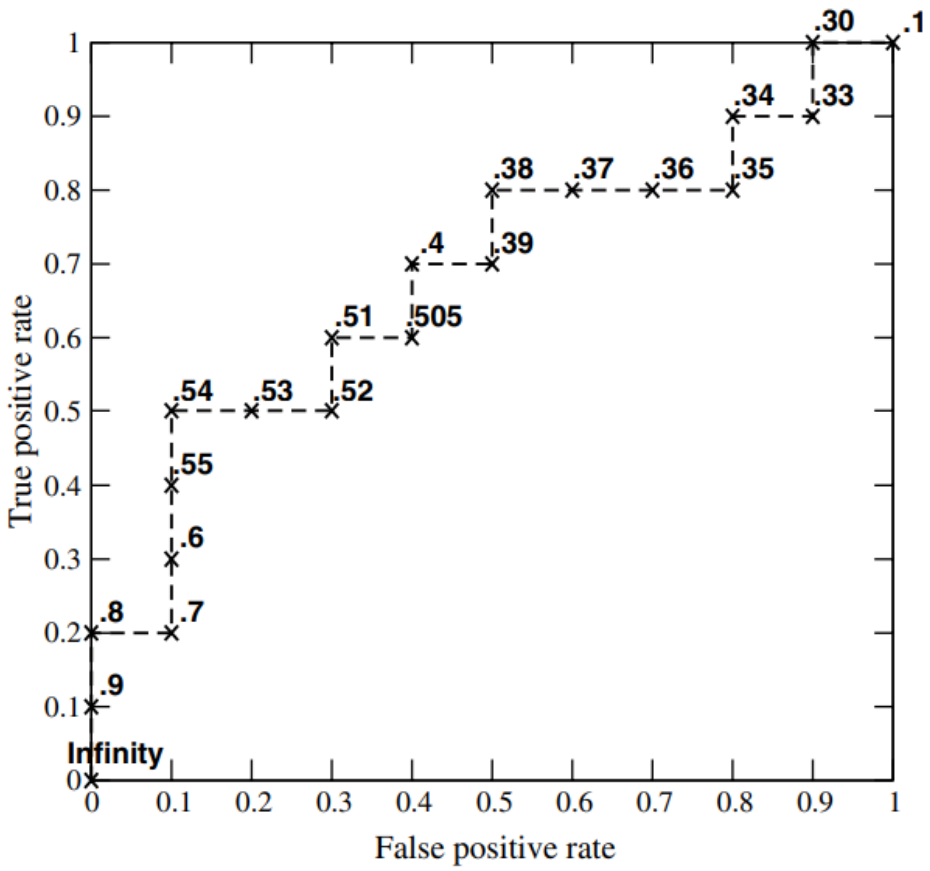

Figure 4.1: ROC curve example

4.2 RGB classification

The subjects and sessions selected for classification were selected as described in section 3.1. These sessions fulfil all three criteria for classifying. As earlier mentioned in chapter 3, and repeated here:

1. None of the channels placed at the visual cortex are marked as bad.
2. The subject had a correct behaviour during recording (e.g. looked at the screen and kept its eyes open).
3. After pre-processing the data (see section 3.1.4), and removing bad epochs, at least 60 epochs of each colour remains.

4.2.1 Three classes

The best result is obtained using a Riemannian FgMDM classifier with features based on the EEG signals as input. Tangent Space with sLDA classifier is almost equally good. Both average at

approximately 75%. The best accuracies are obtained using the data from subject 14, 2 and 13, with an accuracy of 93,42%, 92,55% and 92,34%, respectively. The lowest accuracy is obtained using the data from subject 15, 16 and 31, with an accuracy of 57,00%, 54,67% and 54,04%, respectively.

The best accuracy for EEG source localisation is obtained with a sLDA classifier on subjects 21, 13 and 14. It classify with an accuracy of 87,5%, 72,6% and 67,5%, respectively. The lowest accuracy is obtained by classifying subject 25, 28 and 16 with an accuracy of 35,5%, 35,5% and 32,1%, respectively.

Table 4.3: Result from the subjects and sessions that follow all three criteria. The table is sorted by the accuracies obtained by the FgMDM classifier.

Subject	**Session**	**TS+sLDA**	**std**	**TS+LR**	**std**	**FgMDM**	**std**	**stat+sLDA**	**std**
14	2	0,9342	0,0567	0,8921	0,0720	0,9342	0,0567	0,8158	0,0840
02	2	0,9255	0,0502	0,8835	0,0604	0,9255	0,0502	0,8364	0,0470
13	2	0,9234	0,0231	0,8697	0,0425	0,9208	0,0215	0,8772	0,0795
21	1	0,8864	0,0607	0,8530	0,0987	0,8959	0,0508	0,8621	0,0839
06	2	0,8514	0,0484	0,7695	0,0677	0,8515	0,0506	0,7991	0,0503
29	1	0,8267	0,0668	0,8014	0,0486	0,8294	0,0656	0,7067	0,0713
30	1	0,8158	0,0963	0,8058	0,1155	0,8158	0,0963	0,6086	0,0640
26	2	0,8023	0,0881	0,7616	0,0737	0,8023	0,0881	0,6610	0,0714
07	2	0,7813	0,1092	0,7063	0,0886	0,7813	0,1083	0,6906	0,0973
19	1	0,7599	0,0530	0,6881	0,0600	0,7632	0,0501	0,6285	0,0513
24	1	0,7564	0,0853	0,7102	0,0546	0,7564	0,0853	0,6397	0,1038
11	2	0,7578	0,1016	0,7147	0,1194	0,7550	0,0930	0,6880	0,0707
18	2	0,7512	0,0961	0,7273	0,0916	0,7512	0,0948	0,7034	0,0544
23	1	0,7432	0,1096	0,6757	0,1172	0,7459	0,1096	0,6378	0,0664
05	2	0,7318	0,0845	0,6988	0,1098	0,7318	0,0845	0,6017	0,0800
20	1	0,7153	0,0744	0,7056	0,0820	0,7104	0,0774	0,6935	0,0724
25	1	0,6675	0,1134	0,5822	0,0687	0,6705	0,1104	0,5666	0,1018
08	2	0,6543	0,0682	0,6286	0,1022	0,6514	0,0649	0,6200	0,0809
03	2	0,6351	0,0755	0,6058	0,0606	0,6351	0,0755	0,5442	0,0576
28	1	0,5754	0,0676	0,5504	0,0751	0,5754	0,0676	0,5902	0,0595
15	2	0,5483	0,0991	0,5480	0,0783	0,5451	0,0963	0,5700	0,1067
16	2	0,5463	0,0678	0,5223	0,0677	0,5410	0,0654	0,5467	0,0762
31	1	0,5307	0,0575	0,5257	0,0467	0,5404	0,0616	0,5381	0,0702
Average		**0,7443**	**0,0762**	**0,7055**	**0,0783**	**0,7448**	**0,0750**	**0,6707**	**0,0739**

Table 4.4: Results of the classifying when using EEG source localisation

Subject	Session	stat+sLDA	std	TS+sLDA	std	TS+LR	std	FgMDM	std
21	1	0,8749	0,0638	0,7865	0,0567	0,7818	0,0565	0,7940	0,0774
13	2	0,7262	0,0852	0,6282	0,0640	0,6180	0,0635	0,6080	0,0676
14	2	0,6750	0,1037	0,5875	0,0777	0,5725	0,0794	0,5675	0,0699
19	1	0,6627	0,0986	0,6408	0,0638	0,6513	0,0654	0,6326	0,0592
02	2	0,6290	0,1052	0,6493	0,0635	0,6591	0,0627	0,6541	0,0604
06	2	0,6188	0,0907	0,5537	0,1019	0,5662	0,1116	0,5663	0,0987
26	2	0,5947	0,0965	0,5237	0,1042	0,5105	0,0842	0,5079	0,0623
03	2	0,5675	0,0841	0,4962	0,0770	0,4810	0,0714	0,4860	0,0616
24	1	0,5667	0,1136	0,5113	0,1227	0,4952	0,1322	0,5191	0,1337
27	1	0,4900	0,1700	0,4800	0,2135	0,4600	0,1960	0,4700	0,2002
07	2	0,4859	0,0941	0,4405	0,1046	0,4314	0,1289	0,4344	0,1077
30	1	0,4853	0,0831	0,4497	0,1144	0,4339	0,1114	0,4655	0,1200
20	1	0,4551	0,0886	0,4306	0,0636	0,4111	0,0796	0,4358	0,0632
22	1	0,4385	0,0942	0,4338	0,1019	0,4753	0,1118	0,4755	0,1131
31	1	0,4301	0,0673	0,3919	0,0692	0,4182	0,0644	0,3894	0,0528
19	1	0,4196	0,1085	0,4137	0,0693	0,4107	0,0786	0,4281	0,0754
04	2	0,4136	0,0648	0,3324	0,0723	0,3460	0,0677	0,3330	0,0717
05	2	0,4123	0,0666	0,3952	0,1001	0,3986	0,1102	0,4089	0,0845
23	1	0,4040	0,0697	0,4142	0,0952	0,4061	0,1099	0,4090	0,1013
18	2	0,3979	0,0619	0,3784	0,0701	0,3785	0,0633	0,3736	0,0836
08	2	0,3955	0,0760	0,3610	0,0590	0,3671	0,0672	0,3812	0,0607
11	2	0,3895	0,0632	0,4500	0,0923	0,4763	0,0900	0,4447	0,0907
15	2	0,3866	0,1059	0,3697	0,0505	0,3842	0,0665	0,3548	0,0591
25	1	0,3547	0,0615	0,3009	0,0804	0,3198	0,0827	0,3009	0,0804
28	1	0,3345	0,0844	0,3448	0,0640	0,3350	0,0579	0,3546	0,0719
16	2	0,3207	0,0877	0,2683	0,0536	0,2606	0,0714	0,2787	0,0570
Average	-	**0,4973**	**0,0880**	**0,4628**	**0,0848**	**0,4634**	**0,0879**	**0,4644**	**0,0840**

4.2.2 Two classes

In table 4.5, the results from classifying between two colours are listed. Only the FgMDM classifier with features based on the EEG-signals is represented, classifying {Red vs Blue}, {Red vs Green}, {Green vs Blue} and {Red vs Green vs Blue}. {Red vs Blue} have the highest average accuracy of 88,0%, with subject 14, 02 and 13 as its best subjects. The lowest average accuracy when classifying between two colours are for {Green vs Blue} with an accuracy of 79,5%. The table is ordered according to highest score when classifying {Red vs Green vs Blue}.

Table 4.5: Results from classifying {Red vs Blue}, {Red vs Green}, {Green vs Blue} and {Red vs Green vs Blue} with the Riemannian FgMDM classifier.

Subject	Session	R vs B	std	R vs G	std	G vs B	std	R vs G vs B	std
14	2	0,9842	0,0194	0,9323	0,0477	0,9402	0,0545	0,9342	0,0567
02	2	0,9925	0,0151	0,9625	0,0379	0,9185	0,0432	0,9255	0,0502
13	2	0,9657	0,0269	0,9231	0,0644	0,9462	0,0353	0,9208	0,0215
21	1	0,9719	0,0344	0,8933	0,0734	0,9544	0,0613	0,8959	0,0508
06	2	0,9513	0,0341	0,9410	0,0295	0,8556	0,0560	0,8515	0,0506
29	1	0,9362	0,0439	0,9010	0,0706	0,8067	0,0750	0,8294	0,0656
30	1	0,8618	0,0581	0,6375	0,0942	0,8761	0,0512	0,8158	0,0963
26	2	0,8857	0,0619	0,8616	0,0708	0,8163	0,0684	0,8023	0,0881
07	2	0,8762	0,0680	0,8333	0,1055	0,8301	0,1187	0,7813	0,1083
19	1	0,8650	0,0741	0,8333	0,0532	0,8211	0,0586	0,7632	0,0501
24	1	0,8680	0,0816	0,8219	0,0920	0,8303	0,0914	0,7564	0,0853
11	2	0,9022	0,0490	0,8070	0,0914	0,8000	0,0930	0,7550	0,0930
18	2	0,9245	0,0523	0,8815	0,0515	0,7487	0,1284	0,7512	0,0948
23	1	0,9142	0,0696	0,7680	0,1324	0,7823	0,1273	0,7459	0,1096
05	2	0,9272	0,0525	0,8298	0,0898	0,7801	0,0797	0,7318	0,0845
20	1	0,8635	0,0497	0,7205	0,0894	0,8090	0,0665	0,7104	0,0774
25	1	0,8269	0,0725	0,7591	0,0789	0,7024	0,0838	0,6705	0,1104
08	2	0,8105	0,1119	0,8132	0,0824	0,7315	0,0822	0,6514	0,0649
03	2	0,8108	0,0732	0,7111	0,0831	0,7498	0,0556	0,6351	0,0755
28	1	0,7731	0,0591	0,6946	0,0562	0,6691	0,1015	0,5754	0,0676
15	2	0,7879	0,1018	0,6636	0,0830	0,6071	0,0667	0,5451	0,0963
16	2	0,7322	0,0852	0,6510	0,0803	0,6658	0,0808	0,5410	0,0654
31	1	0,8009	0,0837	0,6610	0,0916	0,6459	0,0840	0,5404	0,0616
Average		**0,8797**	**0,0599**	**0,8044**	**0,0761**	**0,7951**	**0,0767**	**0,7448**	**0,0750**

4.2.3 Receiver operating characteristics (ROC)

In order to evaluate how well the EEG signal model separates the RGB colours, the ROC has been calculated. The ROC for subject, 14, 16 and 31 are illustrated in fig. 4.2, fig. 4.3 and fig. 4.4 respectively. From subject 14 the signal model was able to separate all colours, and it is the

subject that obtained the highest score when classifying between three classes. From subject 31 the lowest score when classifying between three colours was obtained, but it is clear from the ROC that it is especially green that is difficult to distinguish. This result is supported by the results in table 4.5, where subject 31 classify with an accuracy of 80,1% when classifying {`Red vs Blue`}, opposed to classifying {`Red vs Green`} and {`Green vs Blue`} where it obtain an accuracy of 66,1% and 64,6%. Subject 16 is another subject that classified with poor accuracy. From its ROC, it is evident that it is no colours that are much easier to separate than others.

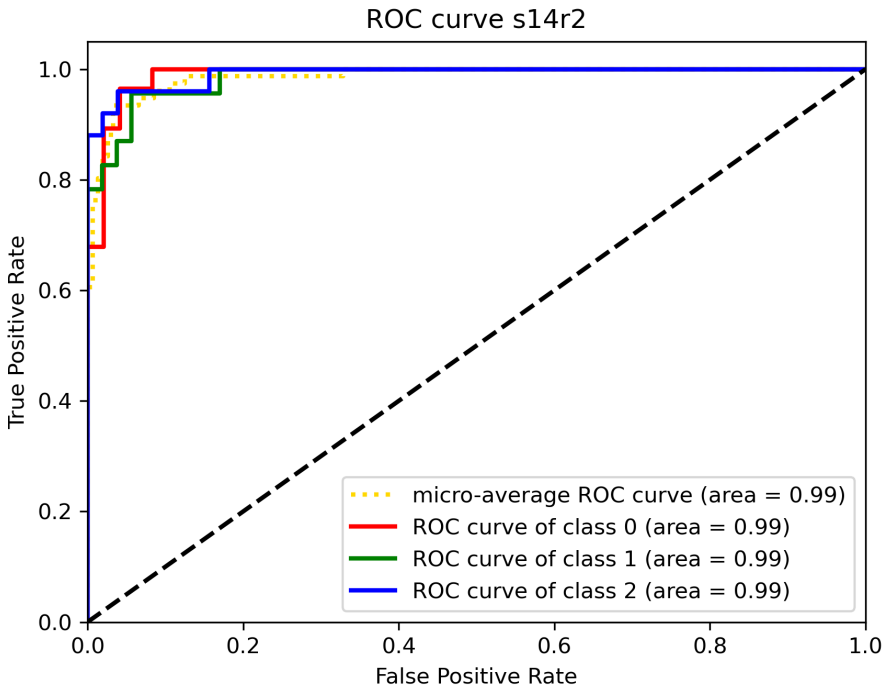

Figure 4.2: ROC curve for subject 14 session 2

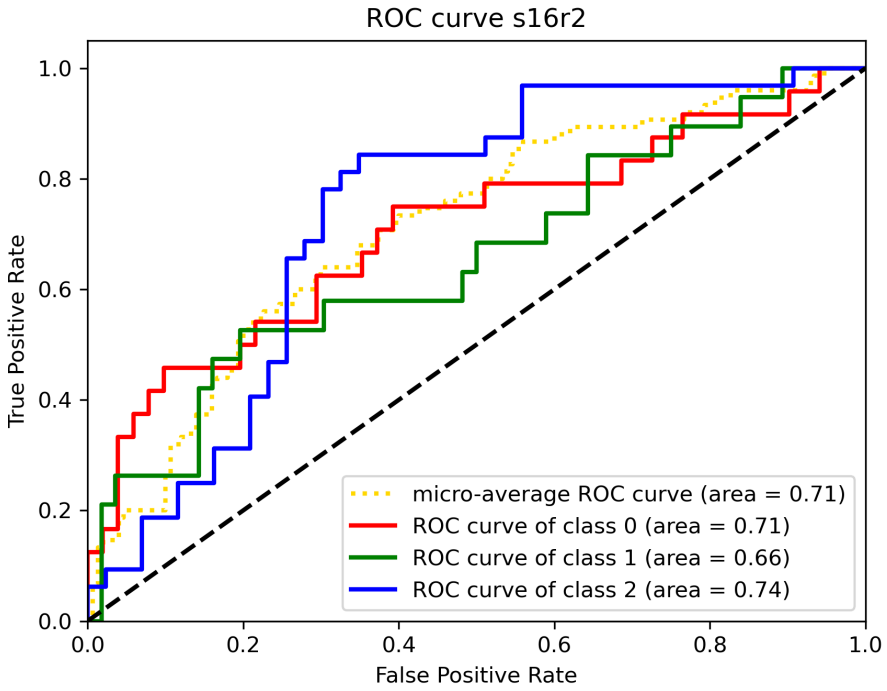

Figure 4.3: ROC curve for subject 16 session 2

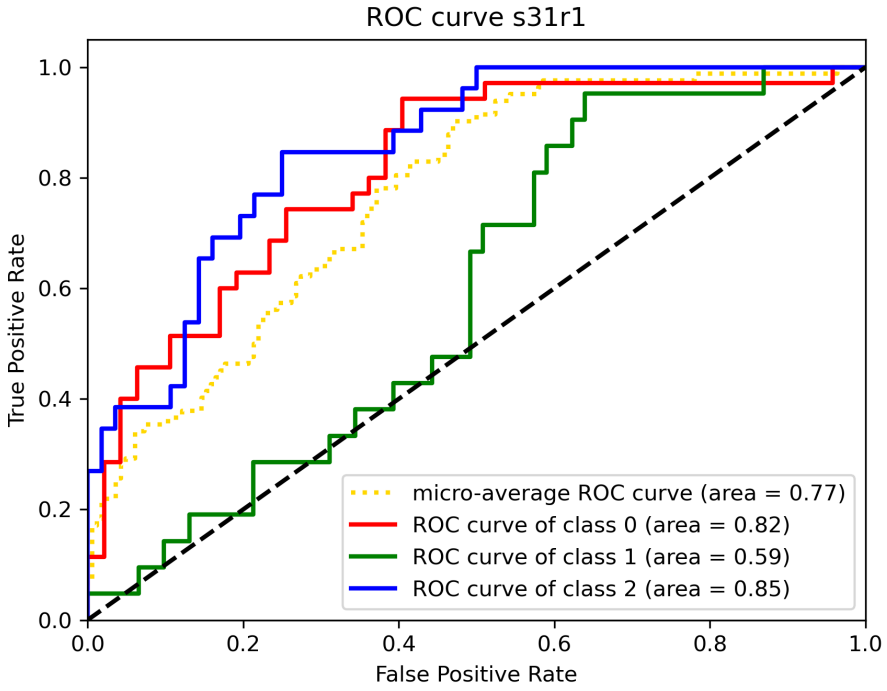

Figure 4.4: ROC curve for subject 31 session 1

4.2.4 Two sessions results

Table 4.6 is the results for those subjects that have two sessions. As mentioned in section 3.1, session 1 of these subjects had two flat channels over the visual cortex, Oz and O2. These channels are therefore excluded for all subjects and sessions in table 4.6. The remaining channels are [P7, PO7, O1, POz, PO8, P8]. Marked rows are subjects with both sessions reaching an accuracy above 60%.

Table 4.6: Result from the subjects with two sessions that fulfil criteria 2) and 3). Subjects marked blue have both sessions above 60%

Subject	Sess.	TS + sLDA	std	TS + LR	std	FgMDM	std	stat. sLDA	std
02	1	0,8416	0,0543	0,7883	0,0515	0,8417	0,0493	0,7202	0,0607
02	2	0,8016	0,0398	0,7795	0,0473	0,8142	0,0213	0,7719	0,0719
03	1	0,5647	0,0561	0,5384	0,0530	0,5647	0,0561	0,5300	0,0758
03	2	0,5526	0,0976	0,5688	0,0838	0,5526	0,0976	0,4878	0,0913
06	1	0,7625	0,0751	0,7267	0,0574	0,7625	0,0740	0,6820	0,0468
06	2	0,7348	0,0537	0,6980	0,0743	0,7398	0,0489	0,6876	0,0652
07	1	0,6342	0,1033	0,6267	0,0577	0,6493	0,1020	0,5814	0,0625
07	2	0,7125	0,0986	0,6813	0,0750	0,7156	0,0963	0,6219	0,0452
08	1	0,5559	0,0482	0,5147	0,0606	0,5471	0,0546	0,5882	0,0644
08	2	0,6343	0,0775	0,5857	0,0642	0,6400	0,0769	0,5400	0,0578
11	1	0,5709	0,0471	0,5363	0,0547	0,5857	0,0528	0,4712	0,0792
11	2	0,6422	0,1112	0,6021	0,1140	0,6447	0,0987	0,6127	0,0522
13	1	0,8135	0,0726	0,7979	0,0431	0,8188	0,0714	0,7331	0,0922
13	2	0,8697	0,0694	0,8108	0,0768	0,8722	0,0680	0,7982	0,1169
14	1	0,7126	0,0827	0,6774	0,0809	0,7125	0,0731	0,7145	0,0744
14	2	0,7342	0,1138	0,7105	0,1229	0,7289	0,1085	0,7158	0,0805
15	1	0,4232	0,0569	0,4634	0,0979	0,4232	0,0569	0,4817	0,0810
15	2	0,4999	0,0603	0,5032	0,0978	0,5030	0,0626	0,5412	0,0991
16	1	0,5209	0,0926	0,5449	0,0573	0,5209	0,0926	0,5665	0,0850
16	2	0,4844	0,0855	0,4792	0,0814	0,4925	0,0786	0,5035	0,0652
18	1	0,6327	0,0412	0,6252	0,0872	0,6379	0,0485	0,6692	0,0582
18	2	0,7202	0,0735	0,7323	0,0809	0,7154	0,0713	0,6697	0,0482
26	1	0,6414	0,0715	0,6183	0,0695	0,6439	0,0681	0,6184	0,0910
26	2	0,6230	0,0494	0,5926	0,0611	0,6203	0,0487	0,5927	0,0786

4.3 Transfer Learning

Cross session transfer learning was tested for the subjects in table 4.6 that had two sessions classifying with an accuracy above 60%. The results are shown in table 4.7. The average between the two sessions was taken for the subjects and is shown as `avg.accuracy`. The same procedure

was done for standard deviation, `avg.std`. In the columns specified as `s1 - s2`, the EEG signal model used session 1 as the source set and session 2 as the target set. The opposite for the column specified as `s2 - s1`. The last column, `diff.` specifies the difference between average accuracy and the highest accuracy of `s1 - s2` and `s2 - s1`.
The confusion matrices for each subject used for transfer learning is provided in appendix appendix B.2.

Table 4.7: Transfer learning results

Subject	**Avg. accuracy**	**Avg. std**	**s1 - s2**	**s2 - s1**	**diff.**
02	0,8216	0,0471	0,8119	0,7825	0,0097
06	0,7487	0,0644	0,7253	0,7044	0,0234
07	0,6734	0,1010	0,6000	0,5138	0,0734
13	0,8416	0,0710	0,7679	0,7402	0,0737
14	0,7234	0,09825	0,6474	0,5843	0,0760
18	0,6765	0,0574	0,3373	0,4698	0,2067
26	0,6322	0,0605	0,6066	0,6108	0,0214

Chapter 5

Discussion

In this chapter the choice of channels, number of classes and the combination of features that gave the best results will be discussed. Furthermore, the results from source localisation and transfer learning will be summarised and compared. Recommendations for further work and a conclusion is also included.

5.1 Choice of channels

The eight channels chosen are shown in table 4.1. From the data explored in section 3.3 it is evident that there is an activity not only in the channels over the visual cortex but also in the frontal and parietal lobes when the subject is presented with a stimuli. Logically, the accuracy should be higher if all channels were included since event-related potentials are found in all channels. Some attempts were made to classify using all channels in an early stage of the project. However, the results of these attempts were poor. There is a lack of consistency in the front channels. It might be the cause why the algorithm performed poorer when including these. Some of the parietal channels, P7 and P8, were used in the final EEG signal model. It was done to include the V4-location and the ventral pathway in the EEG signal model. It indicates that parietal activity is helpful when classifying RGB colours, but most activity is recorded in the occipital lobe. The eight channels that were chosen are marked in fig. 3.4. They were chosen based on the size of their responses when exposed to visual stimuli. These channels showed a consistently large response across epochs and subjects.

Adding more channels than the eight in table 4.1 decreased performance, but removing one of them had an even more significant impact. It is why subjects with bad channels among the eight chosen channels were not included in the main results. When comparing the sessions both in table 4.3 and table 4.6, some of the sessions have a 20% decrease in accuracy when excluding Oz and O2.

One of the significant advantages of only using eight channels is that this also gives fewer dimensions in the covariance matrix. When decomposing the data into eight frequencies, each added channels is equivalent to eight added dimensions in the covariance matrix. It increases computational time dramatically, and the number of frequencies used should be carefully considered before applying the method in an online setting.

5.2 Number of classes

Naturally, the RGB colours can be separated into three different classes. It means that the chance level is at 33% accuracy. If the EEG signal model reaches 66%, it could mean that it is no longer guessing classes and reaches the correct conclusion two out of three times. It could also mean that one of the colours are easier to identify than others, and that the EEG signal model recognises one of the classes every single time. In this case, 66% accuracy could mean that the algorithm can identify one class but can not separate between the two other classes.

Appendix B is added to this thesis with confusion matrices for each subject used for RGB classification showing how well the algorithm classifies each colour. Three tables are also included to describe how well the algorithm separates between two colours. These results should be considered, as separating between two colours in a BCI system could be useful as well. An example is subject 18. The EEG signal model classifies with an accuracy of 75% between all three colours but has an accuracy of 92% when classifying between `red and blue`.

In general, classifying `red vs blue` has higher average accuracy than `red vs green` or `blue vs green`. It indicates that, on average, it is more difficult to distinguish green than red and blue. Recalling fig. 2.5, the medium length waves are closest to the wavelength of the green colour. The overlap of the activation from the other cones are higher for the medium cones, and this could be why it is more difficult to distinguish the green colour from the red and blue colours.

5.3 An EEG signal model

The goal of this thesis was to create an algorithm with the same parameters for all subjects. When observing the signals, it was evident that they differed between subjects, and a greater accuracy could probably be attained if the parameters were customised for each subject. Since there is an unlimited combination of parameters when preprocessing, feature extracting and classifying, it is possible that there is a better combination for the signal models that performed

poorly. However, customising was tried for some subject-specific signal models that obtained poor results but did not increase or decrease the accuracy dramatically.

5.4 RGB classification results

The results in table 4.3 vary between 54% and 93% accuracy, with an average of approximately 75%. Hence, the EEG signal model manages to differentiate between colours to some degree for all subjects. This is considered a success for the authors of this thesis compared with previous results achieved in the area. It is evident from the results that it is possible to classify colours using EEG electrodes. Especially the subjects with a score above 90% provides the belief that this is a method that could be used in an everyday functional situation. However, it must be considered that these are results obtained from data recorded under well controlled conditions. In an online application, the electrodes should preferably be dry and cheap. Hence the data recorded will be of lower quality and prone to a lot more noise.

The highest average results obtained in this project were significantly higher than the results from [2], which achieved an accuracy of 45% when averaging the accuracy from the subject specific classification. While the visual exposure in the experiments was similar, several aspects separate these two projects. For one, the electrodes used in this thesis were wet, and this allowed an impedance below $5k\Omega$, while dry electrodes were used in [2]. It can be an explanation of why this thesis achieved a higher accuracy. The choice of channels used for feature extraction varies some. [2] had four of the eight channels on the frontal lobe and the remaining on the occipital lobe, while all channels in this project were placed on the occipital lobe or close to it. It was done because the response was observed to be higher in the channels on the occipital lobe. The best performing subject specific EEG signal model in [2] classified with an accuracy of 63%, and it was achieved with a nearest neighbour classifier. The highest accuracy for a subject in this project is 93.42%, and the EEG signal model is using several methods described as state-of-the-art in [7], which probably is why it performs so much better.

In [10], the average accuracy obtained was 72%, and the highest subject specific accuracy was 81%. These results are higher than the ones achieved in [2] but still lower than the results in this thesis. However, considering the reduced number of channels and the simple system used to record the signals, the results in [10] are impressive. They also applied a Morlet wavelet transform to their data. Their results and the ones obtained in this thesis give reason to believe this is a powerful feature to extract when classifying colours.

The authors of [11] do not classify RGB colours, but they use Riemannian based classifiers in

a visual experiment. The good results they obtained with Riemannian classifiers can be backed up with the results in this thesis. Not only does the Riemannian classifiers perform well in motor imaginary tasks, but for classifying visually evoked potentials as well.

5.5 Combinations of features

The combination of features that obtained the best results was transforming the signals into eight frequencies using CWT and Morlet wavelets as explained in section 3.4.2. It was probably the shape of the Morlet wavelet that made it easy to match with the interesting peaks explained in section 2.2.3. Many peaks showed a repetitive pattern in a session, and extracting these became the main focus when extracting features from the signals. CWT with a Morlet wavelet was also applied in [10]. The transformed signal was used as a base for feature extraction and showed promising results. In this thesis, a covariance matrix was created for the transformed signals instead of statistical and fractal features.

5.6 Low accuracy achieved when using EEG source localisation

Because the V4 area in the visual cortex is regarded as the location of the colour processing in the brain, sources extracted from this area were expected to yield high results. However, it was not the case, as the highest average accuracy was 50%. When comparing this result to the highest average accuracy in table 4.3, which is 75%, the difference between the best average classification for each method is 25%. This is a substantial difference in performance. For some subjects, the change in performance for the two methods is not as significant. For example, subject 21, where the model with EEG source localisation is only 2.1% worse than the accuracy obtained when not using sources. A reason for this can be that the model of the brain utilised in EEG source reconstruction is not explicitly created for each subject but created from an average, as described in section 3.2. The cause of the good result for subject 21 can be that the average model is similar to the actual head model of the subject. The deviations in the average model from the true head model of each subject can be the cause of the poor results obtained with this method. For example subject 14, achieves the highest accuracy of all the subjects when not using EEG source localisation but loses 26% with the use of sources. Not only is the performance poorer when localising sources but the complexity of the model is increased as well. From these results, EEG source localisation based on an average head model is not recommended for further use.

Table 5.1: Comparison of results with and without EEG source localisation

	With sources	Without sources, with channels	Difference
Best average accuracy	49.7%	74.5%	24.8%
Highest accuracy sub 21	87.5%	89.6%	2.1%
Highest accuracy sub 14	67.5%	93.4%	25.9%

5.7 Transfer learning results

Ideally, the accuracy of one session that has trained on the other should be close to the average accuracy of the two sessions when classified separately. At least within the standard deviation. Only seven subjects were fit for transfer learning, which is a small number to draw any absolute conclusions. The accuracy obtained varied depending on which session was the source data and which was the target data. The differences noted in table 4.7 are based on the best results. Subject 18 have a significant drop in accuracy. Despite this, the result are promising. The other six results are well above chance, and subject 2, 6 and 26 almost seem unaffected by transfer learning.

5.8 Future work

Testing an EEG signal model online

While there has been a focus on EEG signal models that can be used in an online scenario in this thesis, it has not been tested. There is, therefore, a need for this in the future.

EEG Source localisation with individual head model

Not using `fsaverage`, but instead creating the head model for each subject could yield better results. Creating a model based on sources can take several hours for participants, but once the model is created the sources can be used for online classification. The activity in the sources could also provide knowledge about which channels to use and which features to look for in an online BCI system.

Incremental learning

The parameters of adaptive classifiers are incrementally updated when new EEG data is made available [7]. This type of incremental classification can be beneficial when creating a classification model for a new subject. The classification model could be pre-trained on available data from other subjects. Then a few online sessions can be made to extend the model and calibrate

it to this specific subject, thereby removing the need for long recording sessions used to train the initial classification model. This method also allows the classifier to track changes in the signal and remain effective for EEG signals [7].

5.9 Conclusion

The first objective of this thesis was to find the EEG features that separate each RGB colour. Colour-specific features were found for each subject separately, but it was unsuccessful in finding features that could separate colours across subjects. One of the EEG signal models created was able to classify the RGB colours with an average accuracy of 75%. This model used the same methods and parameters on all subjects, thus satisfying the second objective of creating a general EEG signal model. The third objective was to classify the EEG epochs across different recording sessions. Cross session transfer learning was explored on seven subjects. It is difficult to draw a conclusion based on the results from seven subjects. However, the results obtained indicate that it is possible to use data recorded from previous sessions as a source set, classifying a target set recorded later. It is very promising considering how it could dramatically increase the data available for training a machine learning algorithm. It could also open the possibility of online applications.

To conclude, it is possible to differentiate RGB colours using data recorded from EEG electrodes. Using a Morlet wavelet transform and covariance matrix as features have provided good results for many of the subjects participating in the dataset. The Riemannian based classifiers gave the best results and showed promise for transfer learning as well. Better results could probably be obtained using a subject-optimised EEG signal model where the parameters are separately optimised for each subject. Still, the model created in this thesis could work as a base from which a more customised model could be made. However, a model based on the signals created by source reconstruction gave more inferior results but should not be excluded from future research. It is an exciting approach, and when creating subject-specific models of the head, it could provide more knowledge about the processing of colours in the human brain.

Bibliography

[1] Sara L. Ludvigsen and Emma H. Buøen. "Online Classification of EEG Signals from Imagery Movement". Semester project (unpublished). Norwegian University of Science and technology (NTNU), Department of Engineering Cybernetics, Dec. 2020.

[2] Sara Åsly. "Supervised learning for classification of EEG signals evoked by visual exposure to RGB colors". MA thesis. NTNU, June 2019. DOI: 10.13140/RG.2.2.13412.12165.

[3] Ellen J Gerl and Molly R Morris. "The Causes and Consequences of Color Vision". eng. In: 1.4 (2008), pp. 476–486. ISSN: 1936-6426.

[4] Saeid Sanei. "Brain Signals, Their Generation, Acquisition and Properties". In: *Adaptive Processing of Brain Signals*. John Wiley & Sons, Ltd, 2013. Chap. 1, pp. 1–36. ISBN: 9781118622162. DOI: https://doi.org/10.1002/9781118622162.ch1. eprint: https://onlinelibrary.wiley.com/doi/pdf/10.1002/9781118622162.ch1. URL: https://onlinelibrary.wiley.com/doi/abs/10.1002/9781118622162.ch1.

[5] A Kübler et al. "Brain-computer communication: unlocking the locked in". eng. In: *Psychological bulletin* 127.3 (2001), pp. 358–375. ISSN: 0033-2909.

[6] Luis Fernando Nicolas-Alonso and Jaime Gomez-Gil. "Brain computer interfaces, a review". eng. In: *Sensors (Basel, Switzerland)* 12.2 (2012), pp. 1211–1279. ISSN: 1424-8220.

[7] F Lotte et al. "A review of classification algorithms for EEG-based brain–computer interfaces: a 10 year update". In: *Journal of Neural Engineering* 15.3 (Apr. 2018), p. 031005. DOI: 10.1088/1741-2552/aab2f2. URL: https://doi.org/10.1088%5C%2F1741-2552%5C%2Faab2f2.

[8] Lars-Erik Bjørge and Trond Emaus. "Identification of EEG-based signature produced by visual exposure to the primary colours RGB". MA thesis. NTNU, July 2017.

[9] Alejandro Torres-García, Luis Moctezuma, and Marta Molinas. "Assessing the Impact of Idle State Type on the Identification of RGB Color Exposure for BCI". In: Feb. 2020. DOI: 10.5220/0008923101870194.

[10] Mahima Chaudhary et al. “Understanding Brain Dynamics for Color Perception using Wearable EEG headband”. In: *Proceedings of 30th Annual International Conference on Computer Science and Software Engineering 2020* (Aug. 2020).

[11] Emmanuel K. Kalunga et al. “Online SSVEP-based BCI using Riemannian geometry”. In: *Neurocomputing* 191 (2016), pp. 55–68. ISSN: 0925-2312. DOI: https://doi.org/10.1016/j.neucom.2016.01.007. URL: https://www.sciencedirect.com/science/article/pii/S0925231216000540.

[12] Alexandre Gramfort et al. “MEG and EEG Data Analysis with MNE-Python”. In: *Frontiers in Neuroscience* 7.267 (2013), pp. 1–13. DOI: 10.3389/fnins.2013.00267.

[13] A. Barachant and J-R. King. *pyRiemann v0.2.6*. Mar. 2020. DOI: 10.5281/zenodo.18982.

[14] J.-B. Schiratti et al. “An Ensemble Learning Approach to Detect Epileptic Seizures from Long Intracranial EEG Recordings”. In: *2018 IEEE International Conference on Acoustics, Speech and Signal Processing (ICASSP)*. 2018, pp. 856–860. DOI: 10.1109/ICASSP.2018.8461489.

[15] F. Pedregosa et al. “Scikit-learn: Machine Learning in Python”. In: *Journal of Machine Learning Research* 12 (2011), pp. 2825–2830.

[16] Blausen Medicine. *Medical Gallery of Blausen Medical 2014*. URL: https://en.wikiversity.org/wiki/WikiJournal_of_Medicine/Medical_gallery_of_Blausen_Medical_2014#Neurology. (accessed: 14.05.2021).

[17] Parul Verma et al. *Using Bifurcation Theory for Exploring Pain*. Sept. 2019. DOI: 10.1021/acs.iecr.9b04495.

[18] Geoffrey Woodman. “A brief introduction to the use of event-related potentials in studies of perception and attention”. In: *Attention, perception & psychophysics* 72 (Nov. 2010), pp. 2031–46. DOI: 10.3758/APP.72.8.2031.

[19] Sydney North Neurology & Neurophysiology. *Visual Evoked Potential (VEP)*. URL: https://sydneynorthneurology.com.au/visual-evoked-potential-vep/. (accessed: 19.05.2021).

[20] Julia W.Y. Kam et al. “Systematic comparison between a wireless EEG system with dry electrodes and a wired EEG system with wet electrodes”. In: *NeuroImage* 184 (2019), pp. 119–129. ISSN: 1053-8119. DOI: https://doi.org/10.1016/j.neuroimage.2018.09.012. URL: https://www.sciencedirect.com/science/article/pii/S1053811918307961.

[21] Bevil R Conway. “Color Vision, Cones, and Color-Coding in the Cortex”. eng. In: *The Neuroscientist* 15.3 (2009), pp. 274–290. ISSN: 1073-8584.

[22] Wikimedia. *Cone response*. URL: https://commons.wikimedia.org/wiki/File:Cone-response-en.png#/media/File:Cone-response-en.svg. (accessed: 14.05.2021).

[23] Arizona State University - Ask a biologist. *Rods and cones*. URL: https://askabiologist.asu.edu/rods-and-cones. (accessed: 15.05.2021).

[24] Friston Karl J. et al. *Human Brain Function*. Vol. 2nd ed. Academic Press, 2004. ISBN: 9780122648410. URL: http://search.ebscohost.com/login.aspx?direct=true&db=nlebk&AN=141534&site=ehost-live.

[25] Wikimedia. *Human visual pathway*. URL: https://en.wikipedia.org/wiki/Visual_system#/media/File:Human_visual_pathway.svg. (accessed: 14.05.2021).

[26] Lumen Learning. *How we see*. URL: https://s3-us-west-2.amazonaws.com/courses-images/wp-content/uploads/sites/855/2016/10/26200309/visualpathways.png. (accessed: 25.05.2021).

[27] Geoffrey F. Woodman. "A brief introduction to the use of event-related potentials in studies of perception and attention". In: *Attention, Perception, & Psychophysics* 72.8 (2010). DOI: 10.3758/bf03196680. URL: https://pubmed.ncbi.nlm.nih.gov/21097848/.

[28] *MEG Core*. Feb. 2020. URL: https://www.aalto.fi/en/aalto-neuroimaging-ani-infrastructure/meg-core.

[29] *asa*. URL: https://www.ant-neuro.com/products/waveguard/electrode-layouts.

[30] G Schalk et al. "BCI2000: a general-purpose brain-computer interface (BCI) system". eng. In: *IEEE transactions on biomedical engineering* 51.6 (2004), pp. 1034–1043. ISSN: 0018-9294.

[31] Simon Homölle. *Forward and Inverse Modeling of EEG and MEG data*. accessed 10.06.21. 2019. URL: https://www.fieldtriptoolbox.org/assets/pdf/workshop/toolkit2019/forward_inverse.pdf.

[32] B. Neil Cuffin. "EEG dipole source localization: Using inverse solutions for determining source locations". eng. In: *IEEE engineering in medicine and biology magazine* 17.5 (1998), pp. 118–122. ISSN: 0739-5175.

[33] Brian Litt. "Dipoles and the EEG". In: *American Journal of EEG Technology* 31.2 (1991), pp. 119–121. DOI: 10.1080/00029238.1991.11080363. eprint: https://doi.org/10.1080/00029238.1991.11080363. URL: https://doi.org/10.1080/00029238.1991.11080363.

[34] Hans Hallez et al. "Review on solving the forward problem in EEG source analysis". eng. In: *Journal of neuroengineering and rehabilitation* 4.1 (2007), pp. 46–46. ISSN: 1743-0003.

[35] Anders M. Dale et al. "Dynamic Statistical Parametric Mapping: Combining fMRI and MEG for High-Resolution Imaging of Cortical Activity". In: *Neuron* 26.1 (2000), pp. 55–67. ISSN: 0896-6273. DOI: https://doi.org/10.1016/S0896-6273(00)81138-1. URL: https://www.sciencedirect.com/science/article/pii/S0896627300811381.

[36] M.F Glasser et al. “A multi-modal parcellation of human cerebral cortex”. eng. In: *Nature (London)* 536.7615 (2016), pp. 171–178. ISSN: 0028-0836.

[37] Sahil Badani et al. “Detection of epilepsy based on discrete wavelet transform and Teager-Kaiser energy operator”. In: *2017 IEEE Calcutta Conference (CALCON)*. 2017, pp. 164–167. DOI: 10.1109/CALCON.2017.8280717.

[38] Cindy Goh et al. “Comparison of Fractal Dimension Algorithms for the Computation of EEG Biomarkers for Dementia”. In: *CIMED'05: Proc. Computational Intelligence in Medicine and Healthcare* (June 2005).

[39] R. Esteller et al. “A comparison of waveform fractal dimension algorithms”. In: *IEEE Transactions on Circuits and Systems I: Fundamental Theory and Applications* 48.2 (2001), pp. 177–183. DOI: 10.1109/81.904882.

[40] Alexandre Barachant et al. “Classification of covariance matrices using a Riemannian-based kernel for BCI applications”. In: *Neurocomputing* 112 (2013). Advances in artificial neural networks, machine learning, and computational intelligence, pp. 172–178. ISSN: 0925-2312. DOI: https://doi.org/10.1016/j.neucom.2012.12.039. URL: http://www.sciencedirect.com/science/article/pii/S0925231213001574.

[41] Christopher M Bishop. *Pattern recognition and machine learning*. eng. Information science and statistics. New York: Springer, 2006. ISBN: 0387310738.

[42] Tao Li, Shenghuo Zhu, and Mitsunori Ogihara. “Using discriminant analysis for multi-class classification: An experimental investigation”. In: *Knowledge and Information Systems* 10 (Nov. 2006), pp. 453–472. DOI: 10.1007/s10115-006-0013-y.

[43] Peter E. Hart Richard O. Duda and David G.Stork. *Pattern Classification*. 2nd ed. John Wiley & Sons, 2001. ISBN: 0471056693.

[44] Olivier Ledoit and M. Wolf. “Honey, I Shrunk the Sample Covariance Matrix”. In: *Capital Markets: Asset Pricing & Valuation* (2003).

[45] F. Yger, M. Berar, and F. Lotte. “Riemannian Approaches in Brain-Computer Interfaces: A Review”. In: *IEEE Transactions on Neural Systems and Rehabilitation Engineering* 25.10 (2017), pp. 1753–1762. DOI: 10.1109/TNSRE.2016.2627016.

[46] Alexandre Barachant et al. “Riemannian geometry applied to BCI classification”. In: *9th International Conference Latent Variable Analysis and Signal Separation (LVA/ICA 2010)*. Ed. by Vigneron et al. Vol. 6365. Series: Lecture Notes in Computer Science. Subseries: Theoretical Computer Science and General Issues. ISBN 978-3-642-15994-7, Softcover. Saint-Malo, France: Springer, Sept. 2010, pp. 629–636. DOI: 10.1007/978-3-642-15995-4_78. URL: https://hal.archives-ouvertes.fr/hal-00602700.

[47] Marco Congedo, Alexandre Barachant, and Rajendra Bhatia. “Riemannian geometry for EEG-based brain-computer interfaces; a primer and a review”. In: *Brain-Computer Interfaces* 4.3 (2017), pp. 155–174. DOI: 10.1080/2326263X.2017.1297192. URL: https://hal.archives-ouvertes.fr/hal-01570120.

[48] Feng Li et al. “Transfer Learning Algorithm of P300-EEG Signal Based on XDAWN Spatial Filter and Riemannian Geometry Classifier”. In: *Applied Sciences* 10.5 (2020). ISSN: 2076-3417. URL: https://www.mdpi.com/2076-3417/10/5/1804.

[49] Alexandre Barachant et al. “Multiclass Brain-Computer Interface Classification by Riemannian Geometry”. In: *IEEE transactions on bio-medical engineering* 59 (Oct. 2011), pp. 920–8. DOI: 10.1109/TBME.2011.2172210.

[50] Tom Fawcett. “An introduction to ROC analysis”. In: *Pattern Recognition Letters* 27.8 (2006). ROC Analysis in Pattern Recognition, pp. 861–874. ISSN: 0167-8655. DOI: https://doi.org/10.1016/j.patrec.2005.10.010. URL: https://www.sciencedirect.com/science/article/pii/S016786550500303X.

Appendix A

Acronyms

AP Action potential

BCI Brain-computer interface

BEM Boundary Element Method

CNS Central nervous system

CVM Covariance matrix

CWT Continuous wavelet transform

dSPM Dynamic statistical parametric mapping

DWT Discrete wavelet transform

ECoG Electrocorticography

EEG Electroencephalography

EMD Empirical mode decomposition

EPSP Excitatory postsynaptic potential

ERP Event-related potential

FgMDM Minimum distance to mean with geodesic filtering

fMRI Functional magnetic resonance imaging

ICA Independent component analysis

IMF Intrinsic mode function

IPSP Inhibitory postsynaptic potential

LDA Linear discriminant Analysis

LGN Lateral geniculate nucleus

LR Logistic regression

MDM Minimum distance to mean

MEG Magnetoencephalography

RF Random forest

RGB Red, green and blue

SPD Symmetric positive-definite

SSVEP Steady state visually evoked potential

SVM Support vector machines

VEP Visually evoked potential

Appendix B

Appendix

B.1 Confusion matrices results from RGB classification

Confusion matrices for each subject in table 3.1 using 80% of the dataset as source set, and 20% as target set. The models used are the same models that gave the results in table 4.3.

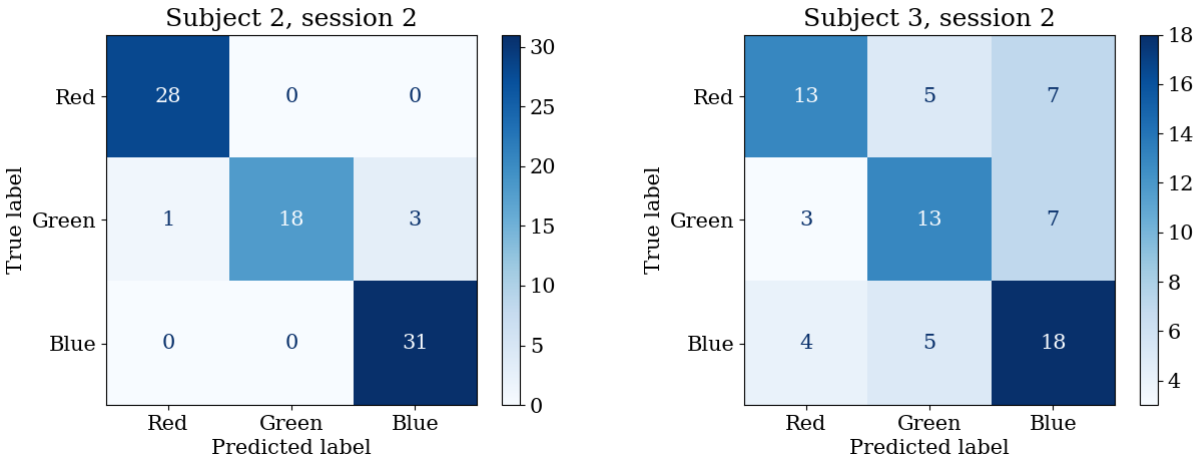

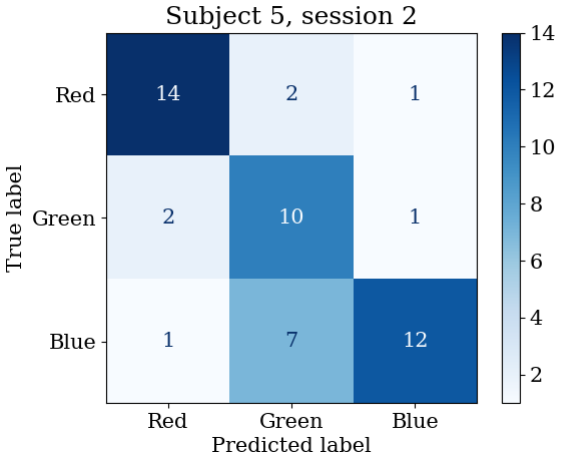
Subject 5, session 2
Red
Green
Blue
True label
14
2
1
2
10
1
1
7
12
Red
Green
Blue
Predicted label
14
12
10
8
6
4
2

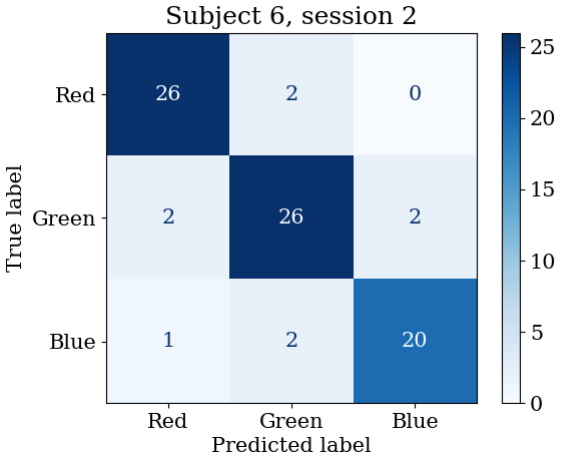
Subject 6, session 2
Red
Green
Blue
True label
26
2
0
2
26
2
1
2
20
Red
Green
Blue
Predicted label
25
20
15
10
5
0

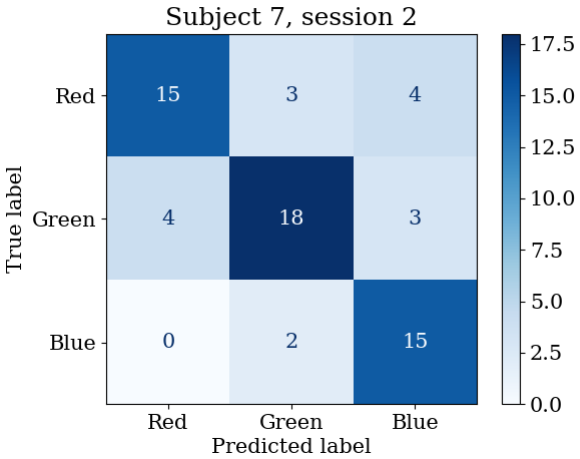
Subject 7, session 2
Red
Green
Blue
True label
15
3
4
4
18
3
0
2
15
Red
Green
Blue
Predicted label
17.5
15.0
12.5
10.0
7.5
5.0
2.5
0.0

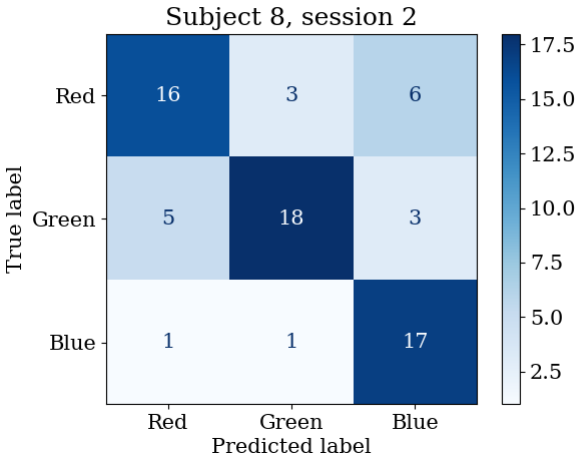
Subject 8, session 2
Red
Green
Blue
True label
16
3
6
5
18
3
1
1
17
Red
Green
Blue
Predicted label
17.5
15.0
12.5
10.0
7.5
5.0
2.5

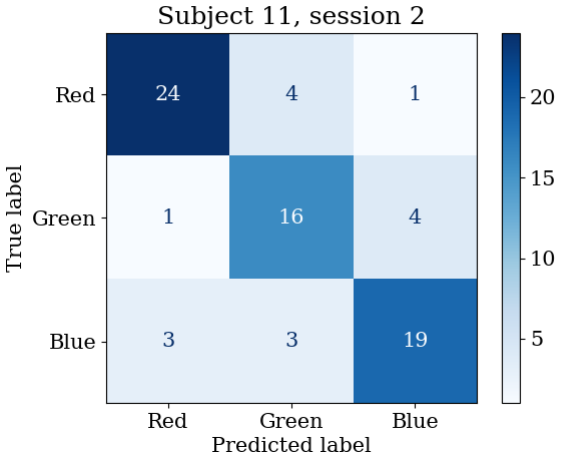
Subject 11, session 2
Red
Green
Blue
True label
24
4
1
1
16
4
3
3
19
Red
Green
Blue
Predicted label
20
15
10
5

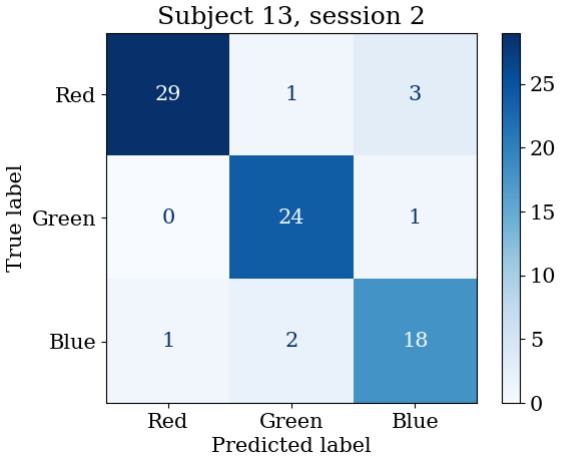
Subject 13, session 2
Red
Green
Blue
True label
29
1
3
0
24
1
1
2
18
Red
Green
Blue
Predicted label
25
20
15
10
5
0

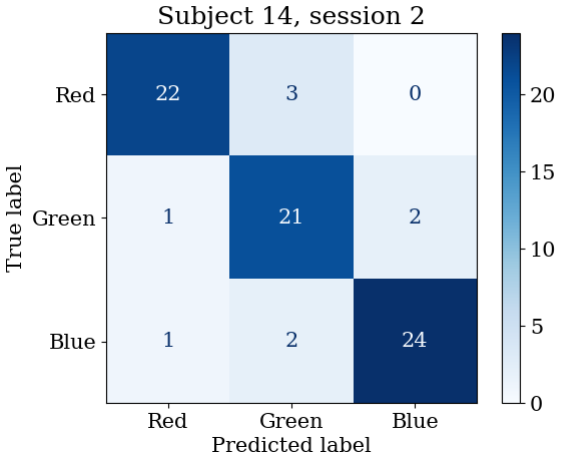
Subject 14, session 2
Red
Green
Blue
True label
22 3 0
1 21 2
1 2 24
Red
Green
Blue
Predicted label
20
15
10
5
0

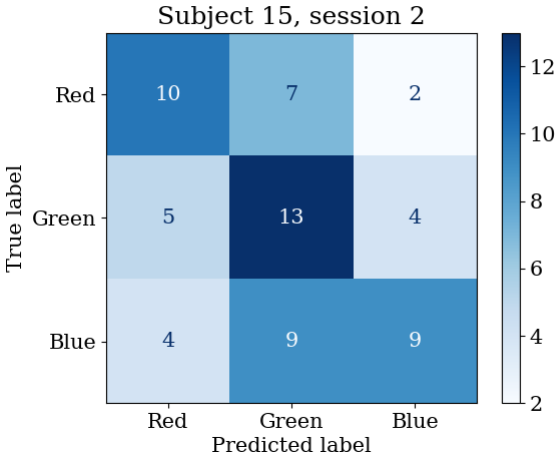
Subject 15, session 2
Red
Green
Blue
True label
10 7 2
5 13 4
4 9 9
Red
Green
Blue
Predicted label
12
10
8
6
4
2

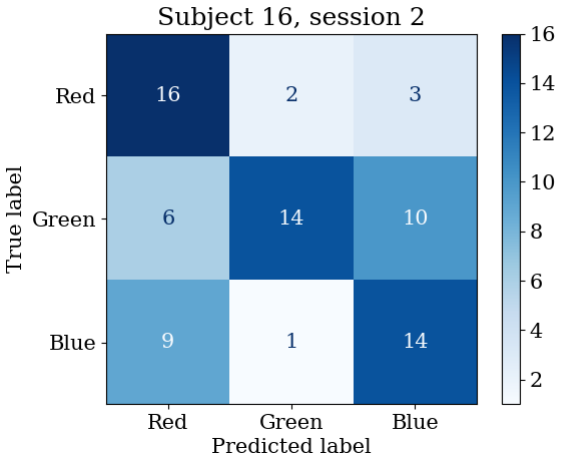
Subject 16, session 2
Red
Green
Blue
True label
16 2 3
6 14 10
9 1 14
Red
Green
Blue
Predicted label
16
14
12
10
8
6
4
2

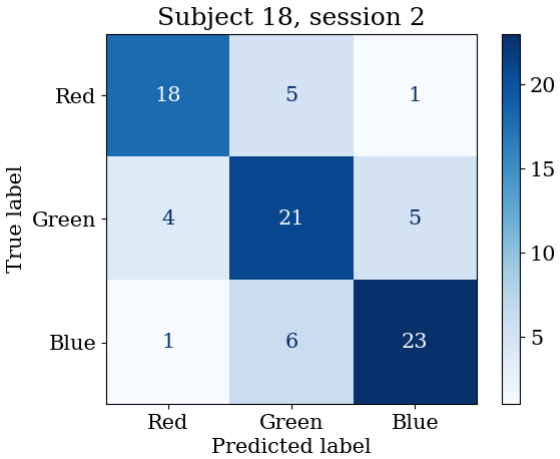
Subject 18, session 2
Red
Green
Blue
True label
18 5 1
4 21 5
1 6 23
Red
Green
Blue
Predicted label
20
15
10
5

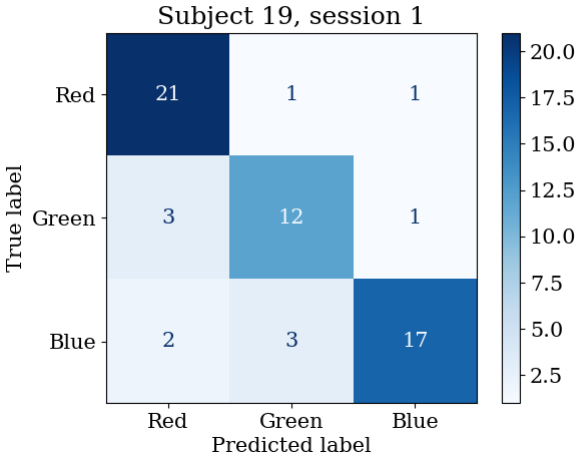
Subject 19, session 1
Red
Green
Blue
True label
21 1 1
3 12 1
2 3 17
Red
Green
Blue
Predicted label
20.0
17.5
15.0
12.5
10.0
7.5
5.0
2.5

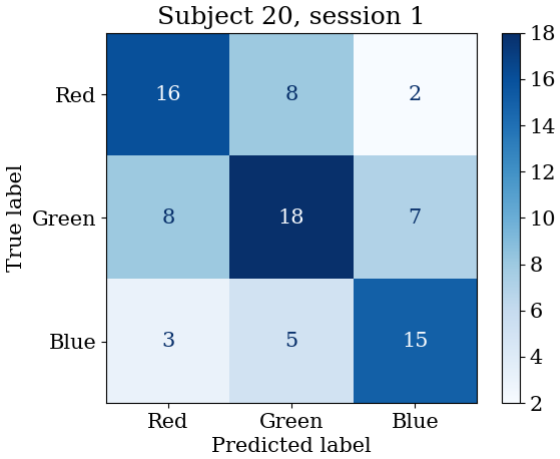
Subject 20, session 1
Red
Green
Blue
True label
16 8 2
8 18 7
3 5 15
Red
Green
Blue
Predicted label
18
16
14
12
10
8
6
4
2

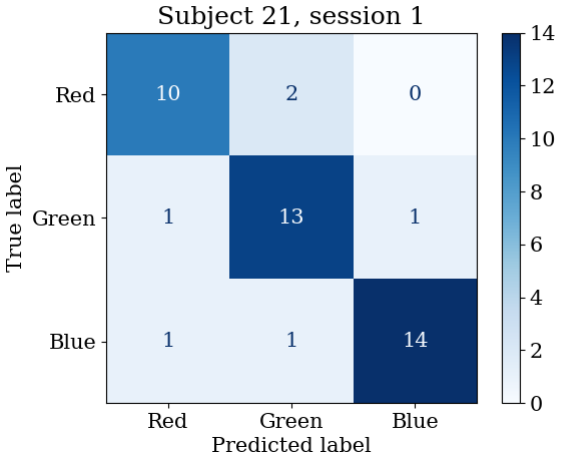
Subject 21, session 1
Red
Green
Blue
True label
Predicted label
10 2 0
1 13 1
1 1 14
14 12 10 8 6 4 2 0

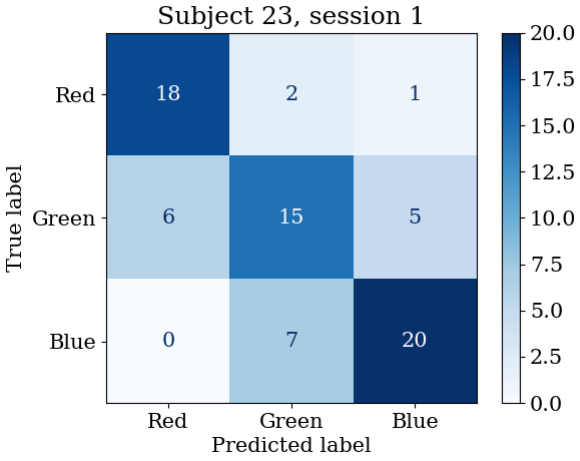
Subject 23, session 1
Red
Green
Blue
True label
Predicted label
18 2 1
6 15 5
0 7 20
20.0 17.5 15.0 12.5 10.0 7.5 5.0 2.5 0.0

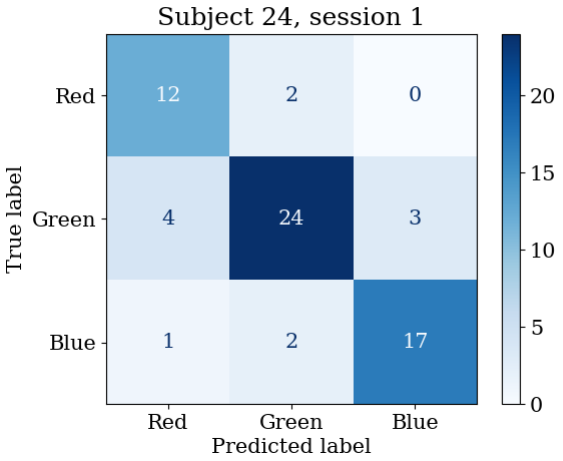
Subject 24, session 1
Red
Green
Blue
True label
Predicted label
12 2 0
4 24 3
1 2 17
20 15 10 5 0

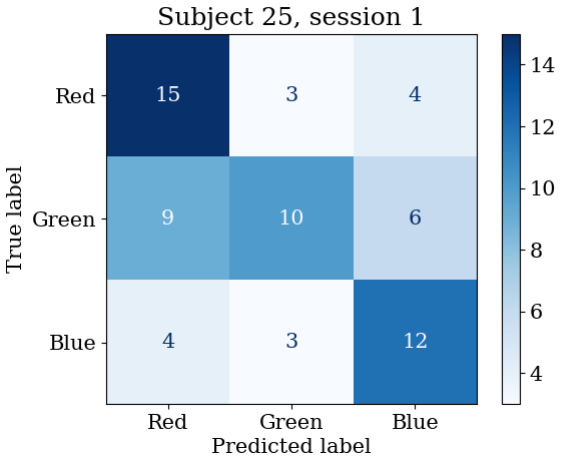
Subject 25, session 1
Red
Green
Blue
True label
Predicted label
15 3 4
9 10 6
4 3 12
14 12 10 8 6 4

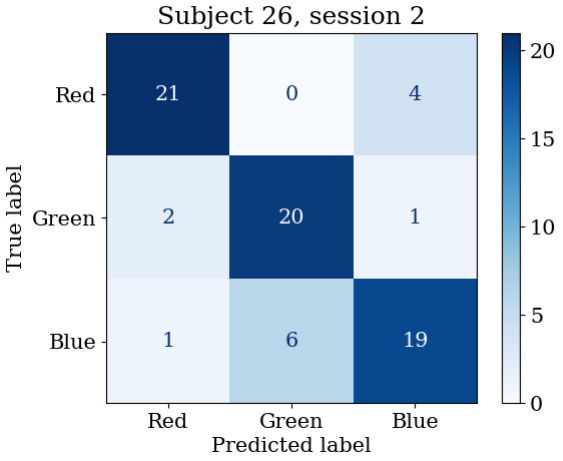
Subject 26, session 2
Red
Green
Blue
True label
Predicted label
21 0 4
2 20 1
1 6 19
20 15 10 5 0

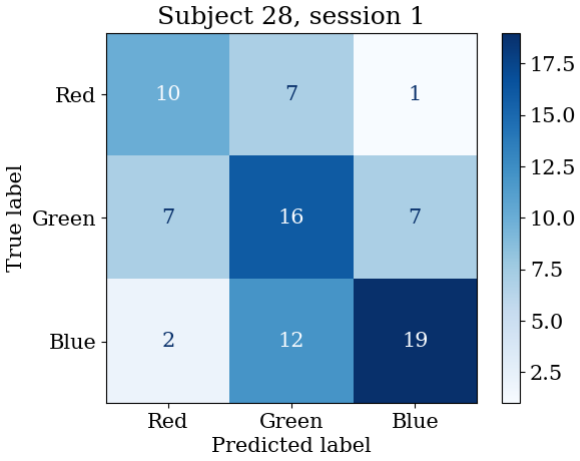
Subject 28, session 1
Red
Green
Blue
True label
Predicted label
10 7 1
7 16 7
2 12 19
17.5 15.0 12.5 10.0 7.5 5.0 2.5

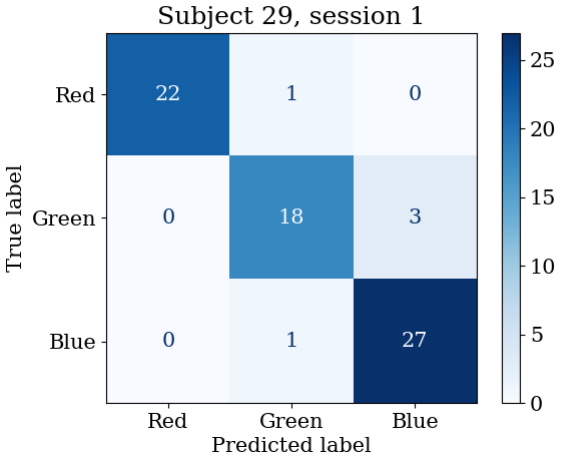
Subject 29, session 1
Red
Green
Blue
True label
22
1
0
0
18
3
0
1
27
Red
Green
Blue
Predicted label
25
20
15
10
5
0

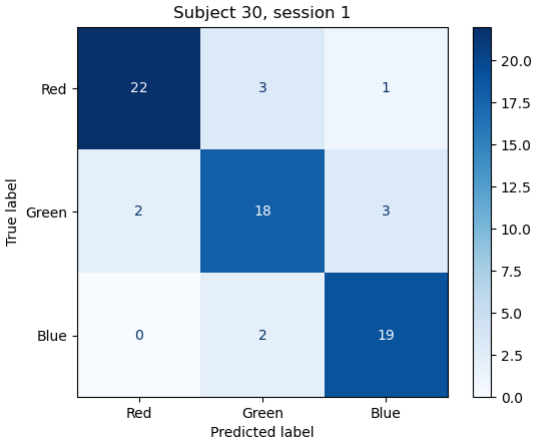
Subject 30, session 1
Red
Green
Blue
True label
22
3
1
2
18
3
0
2
19
Red
Green
Blue
Predicted label
20.0
17.5
15.0
12.5
10.0
7.5
5.0
2.5
0.0

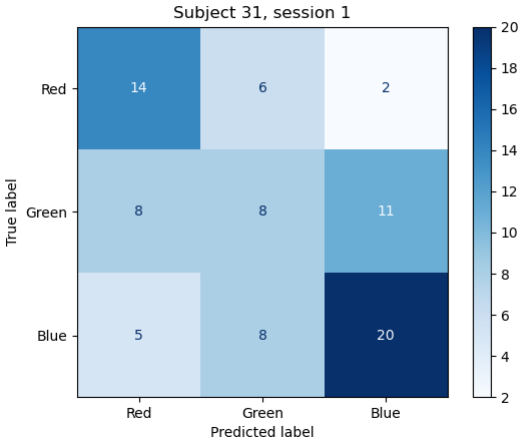
Subject 31, session 1
Red
Green
Blue
True label
14
6
2
8
8
11
5
8
20
Red
Green
Blue
Predicted label
20
18
16
14
12
10
8
6
4
2

B.2 Confusion matrices results from transfer learning

Confusion matrices for session to session transfer learning. One session is used as source set, and an other as target set. The matrices are created by the same EEG signal models that gave the results in table 4.7.

Subject 2

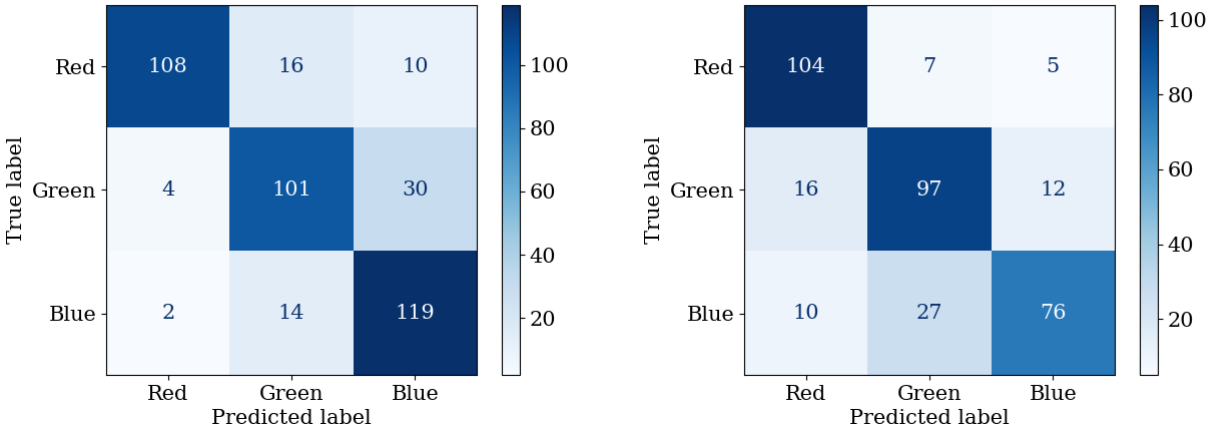

(a) Training on session 1, testing on session 2.

(b) Training on session 1, testing on session 2.

Figure B.12: Session to session classifying for subject 2.

Subject 6

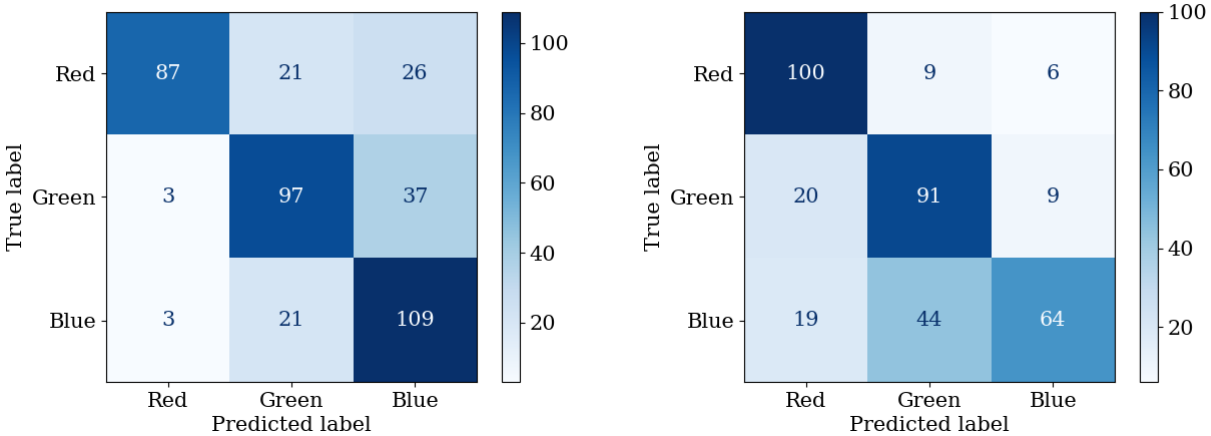

(a) Training on session 1, testing on session 2.

(b) Training on session 1, testing on session 2.

Figure B.13: Session to session classifying for subject 6.

Subject 7

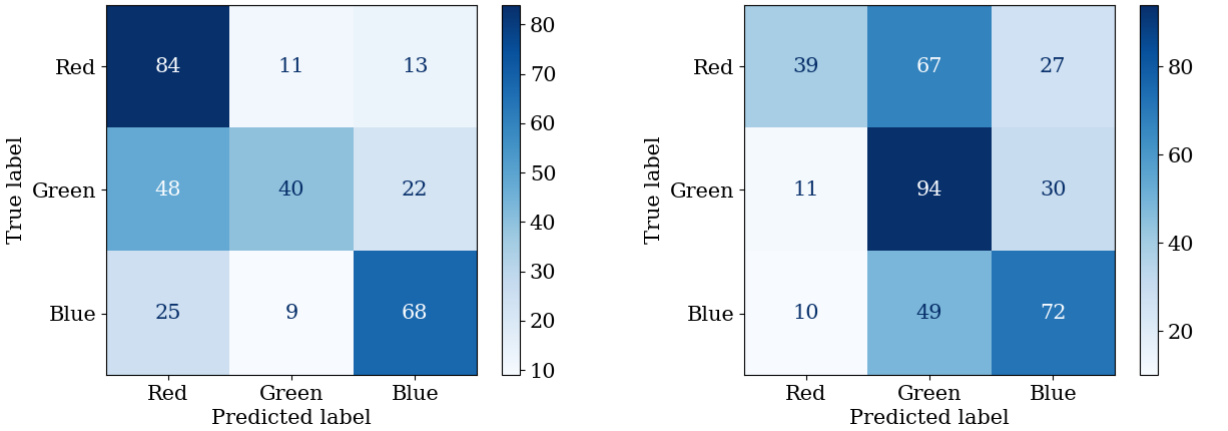

(a) Training on session 1, testing on session 2.

(b) Training on session 1, testing on session 2.

Figure B.14: Session to session classifying for subject 7.

Subject 13

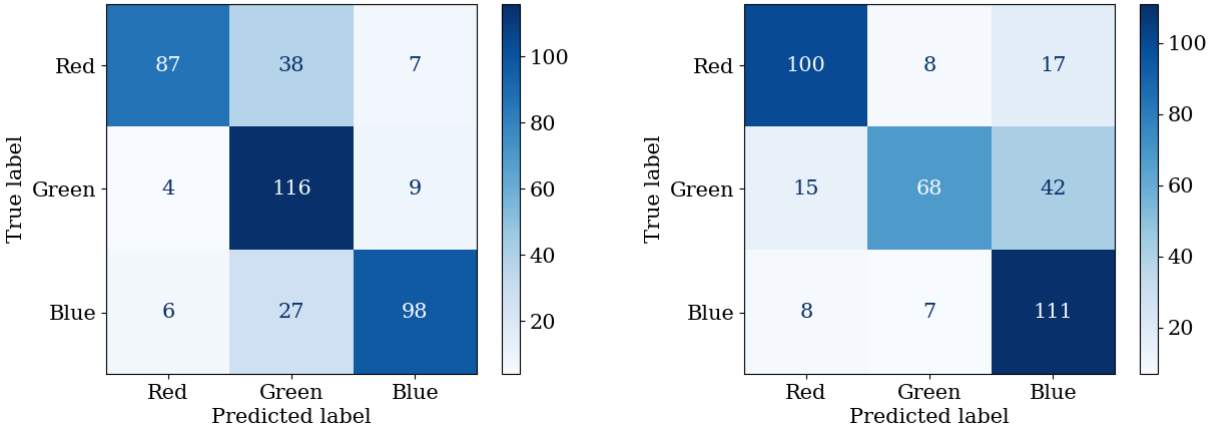

(a) Training on session 1, testing on session 2.

(b) Training on session 1, testing on session 2.

Figure B.15: Session to session classifying for subject 13.

Subject 14

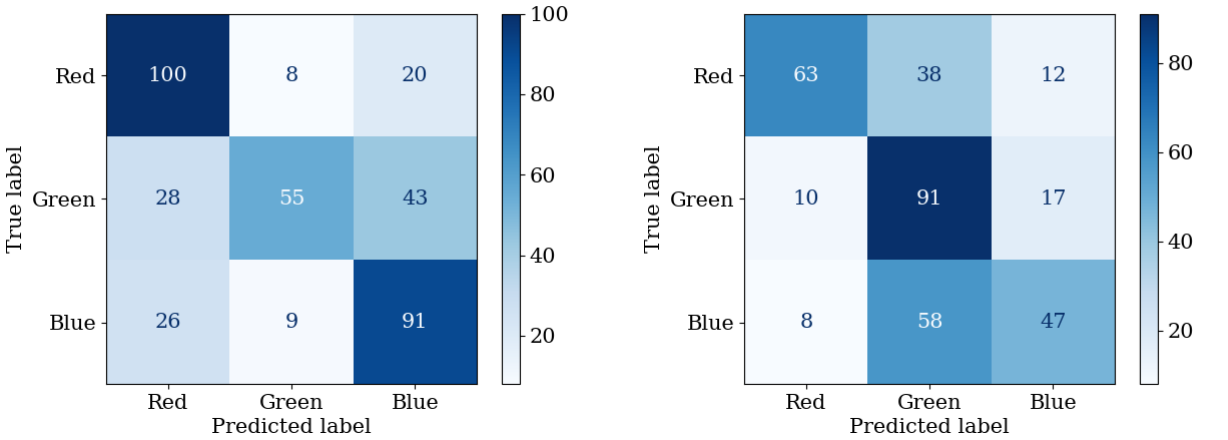

(a) Training on session 1, testing on session 2.

(b) Training on session 1, testing on session 2.

Figure B.16: Session to session classifying for subject 14.

Subject 18

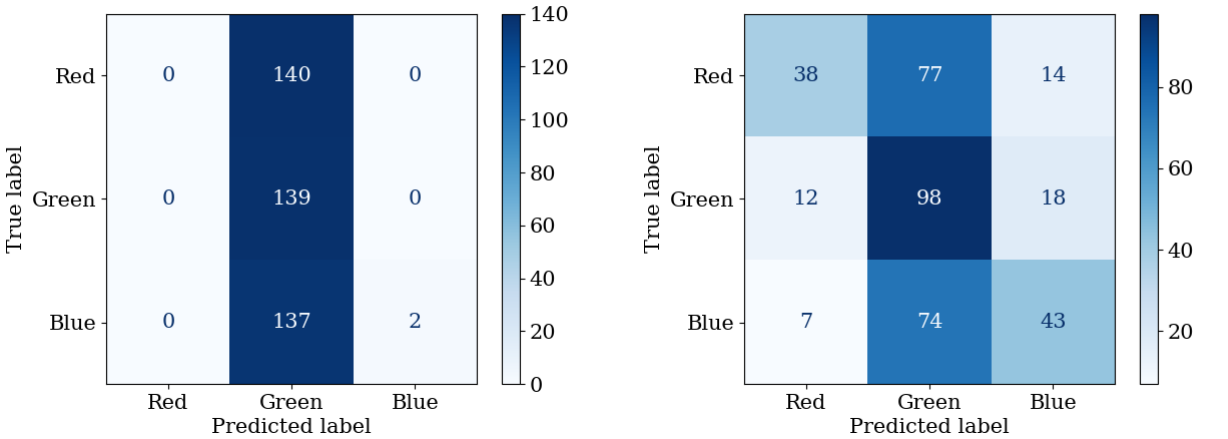

(a) Training on session 1, testing on session 2.

(b) Training on session 1, testing on session 2.

Figure B.17: Session to session classifying for subject 18.

Subject 26

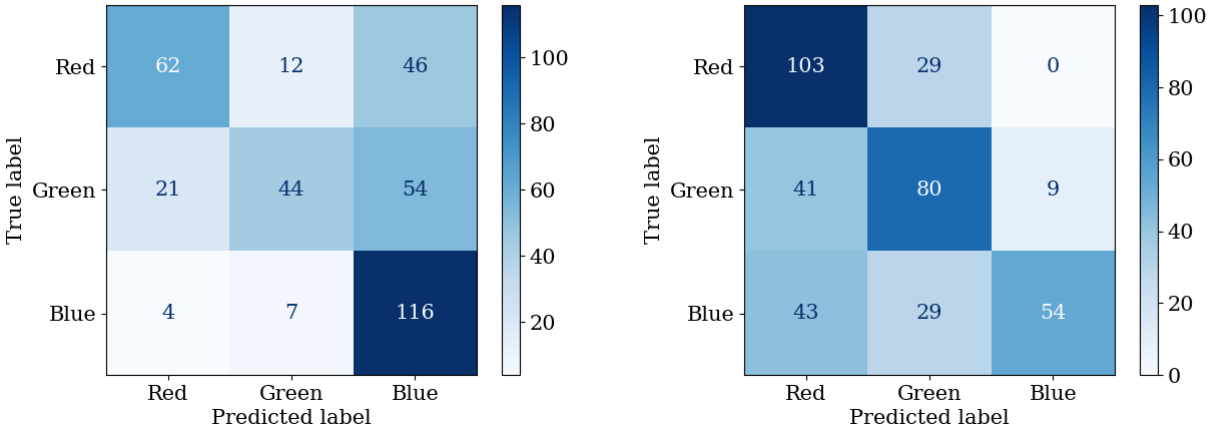

(a) Training on session 1, testing on session 2.

(b) Training on session 1, testing on session 2.

Figure B.18: Session to session classifying for subject 26.

B.3 ROC curves for all subjects

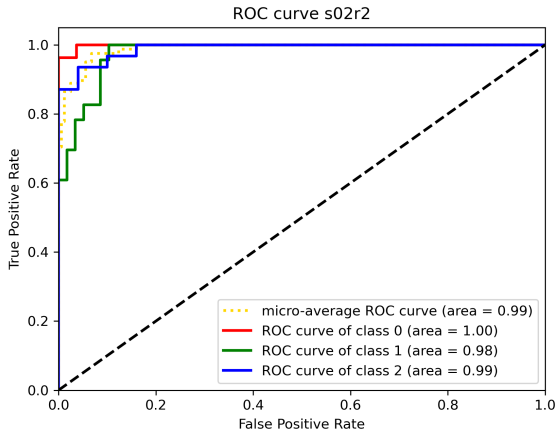

(a) Subject 2 session 2

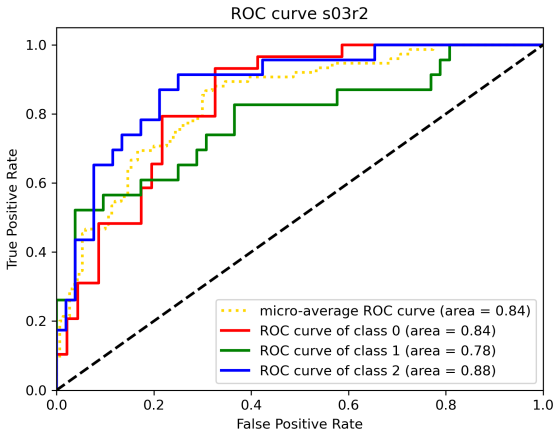

(b) Subject 3 session 2

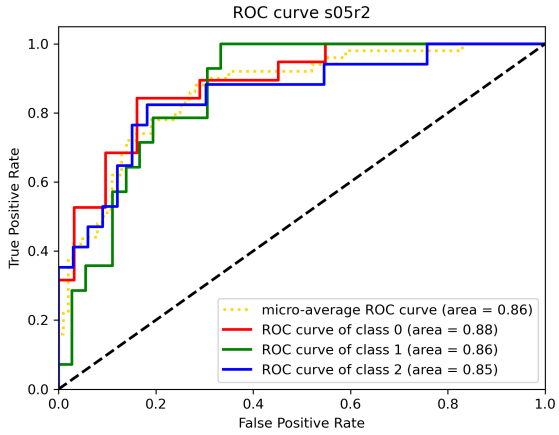

(c) Subject 5 session 2

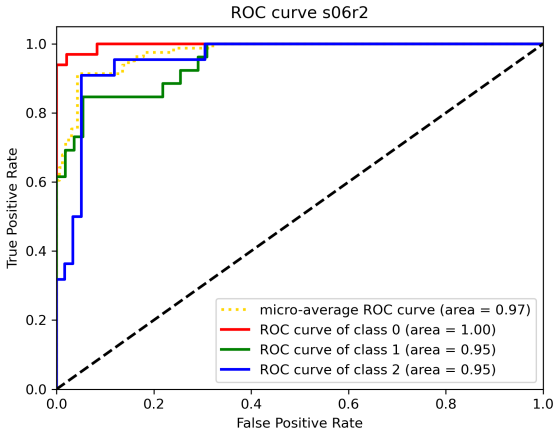

(d) Subject 6 session 2

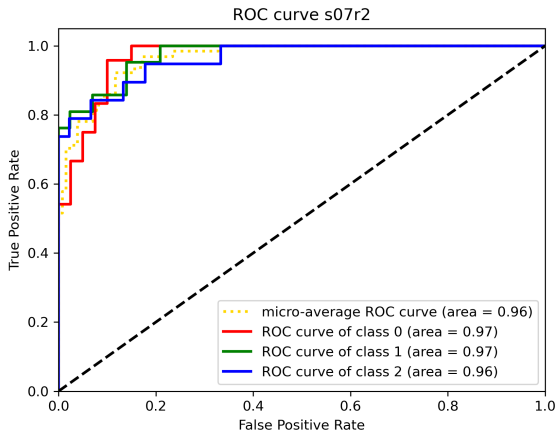

(e) Subject 7 session 2

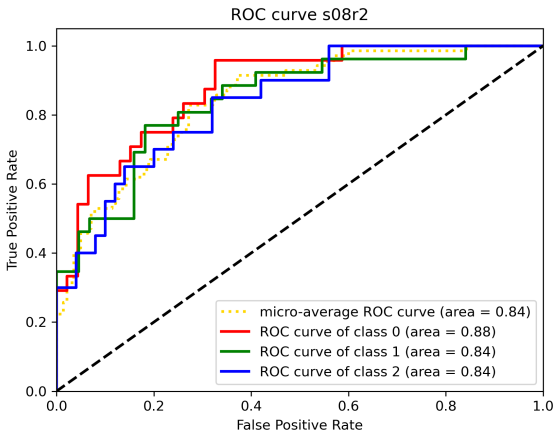

(f) Subject 8 session 2

Figure B.19: ROC curves for subjects 2, 3, 5, 6, 7 and 8.

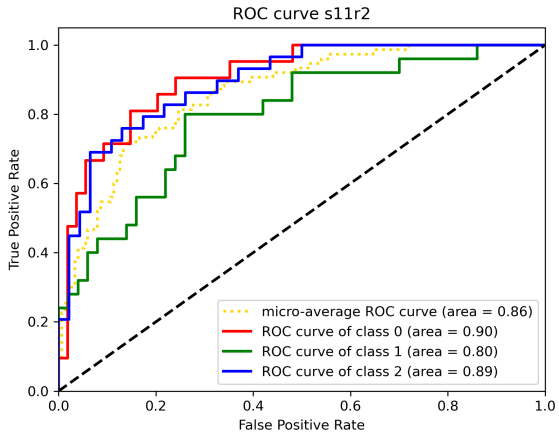

(a) Subject 11 session 02

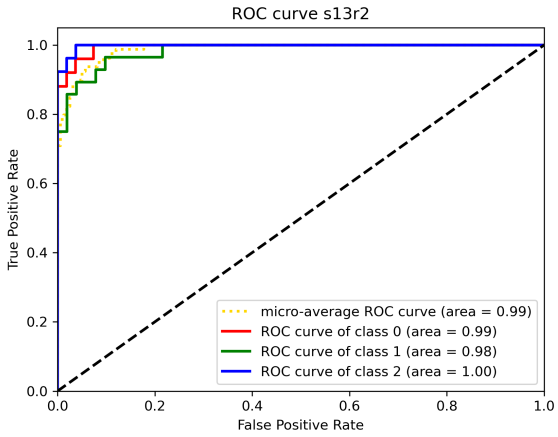

(b) Subject 13 session 02

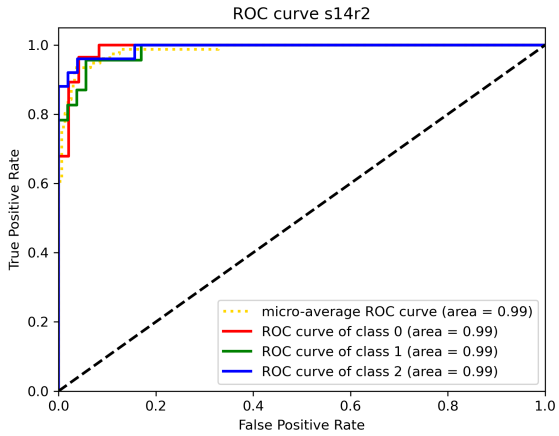

(c) Subject 14 session 02

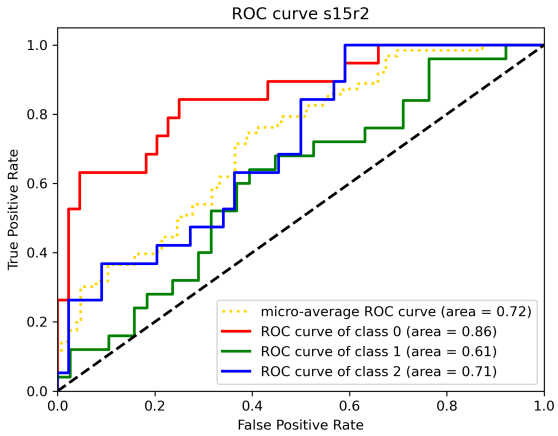

(d) Subject 15 session 02

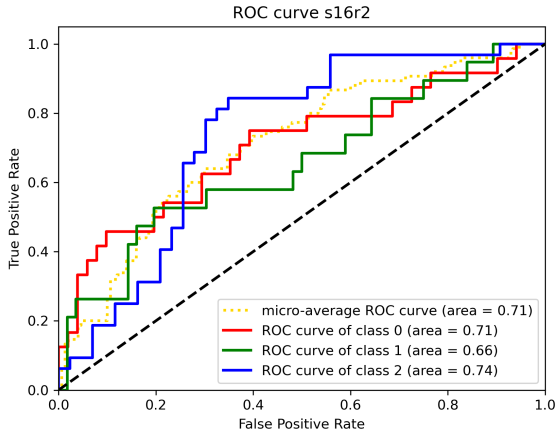

(e) Subject 16 session 02

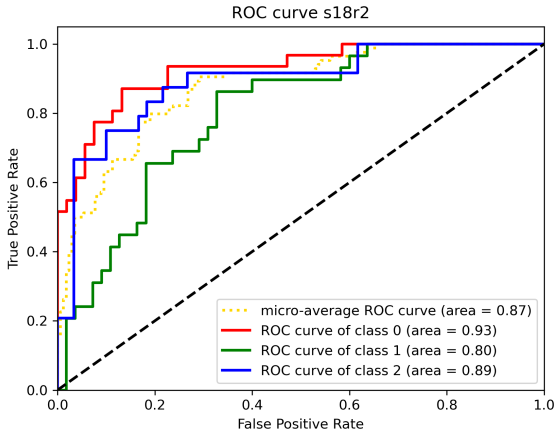

(f) Subject 18 session 02

Figure B.20: ROC curves for subjects 11, 13, 14, 15, 16 and 18.

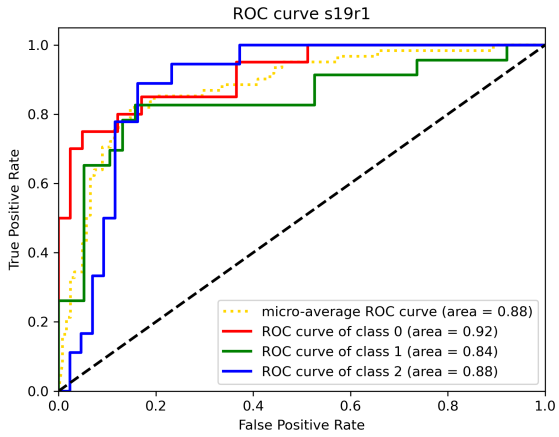

(a) Subject 19 session 01

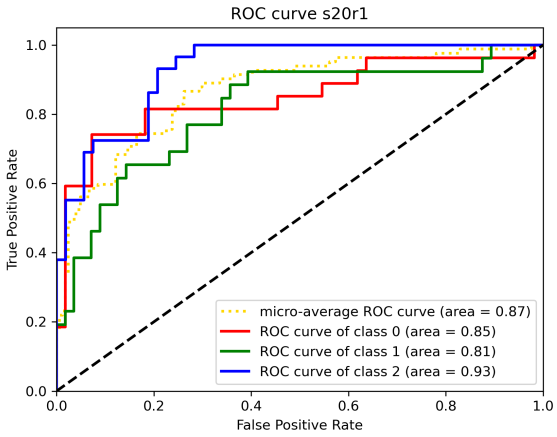

(b) Subject 20 session 01

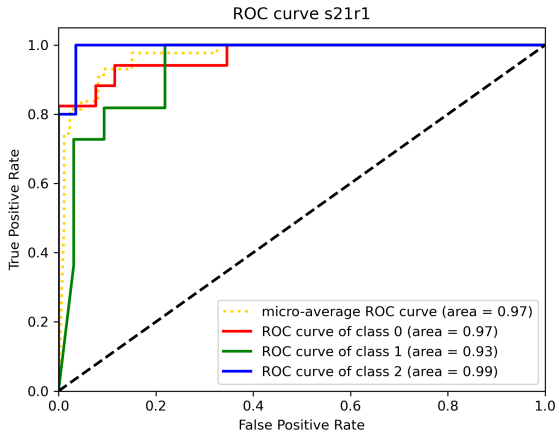

(c) Subject 21 session 01

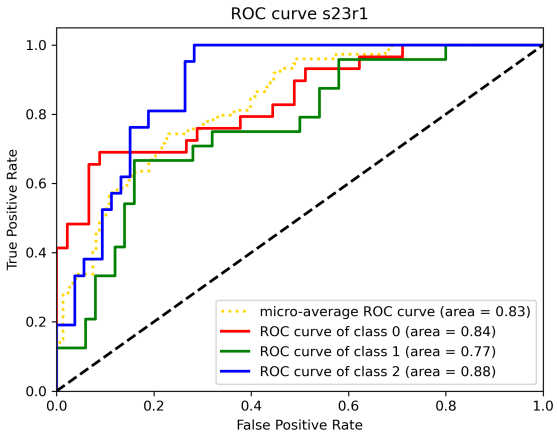

(d) Subject 23 session 01

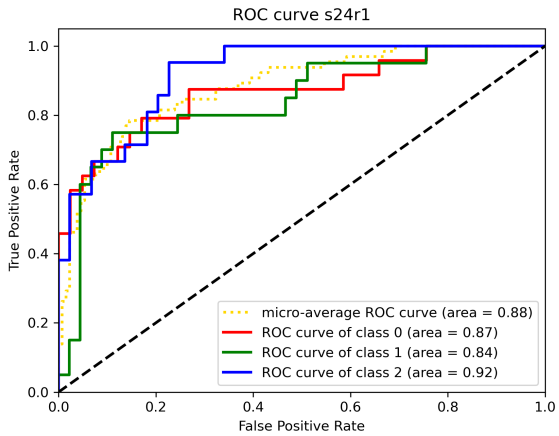

(e) Subject 24 session 01

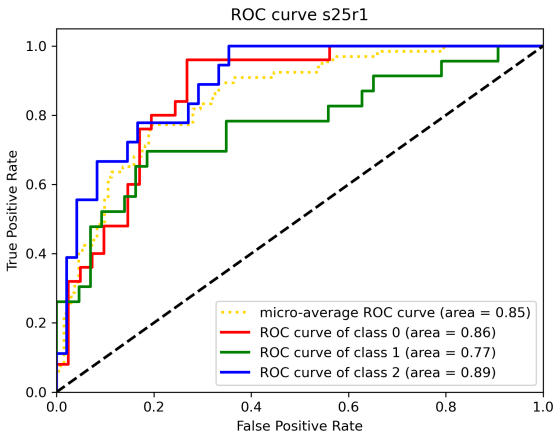

(f) Subject 25 session 01

Figure B.21: ROC curves for subjects 19, 20, 21, 23, 24 and 25.

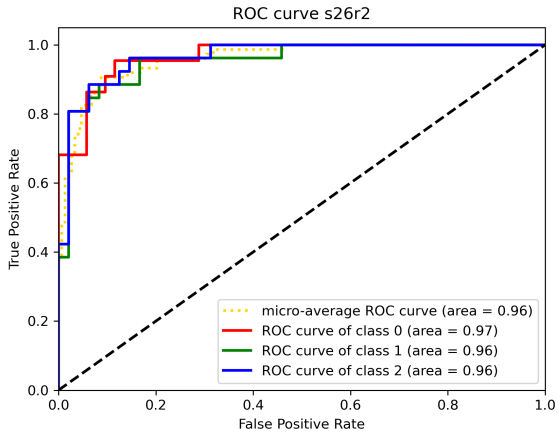

(a) Subject 26 session 02

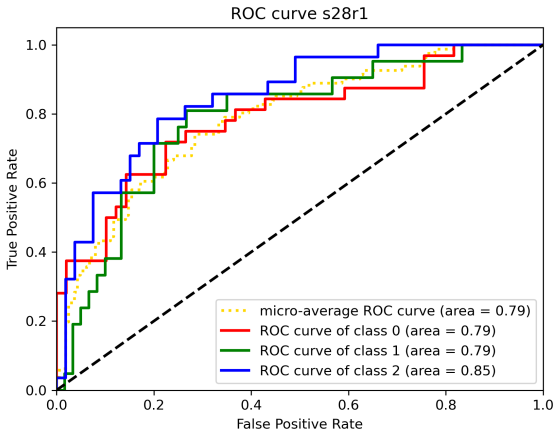

(b) Subject 28 session 01

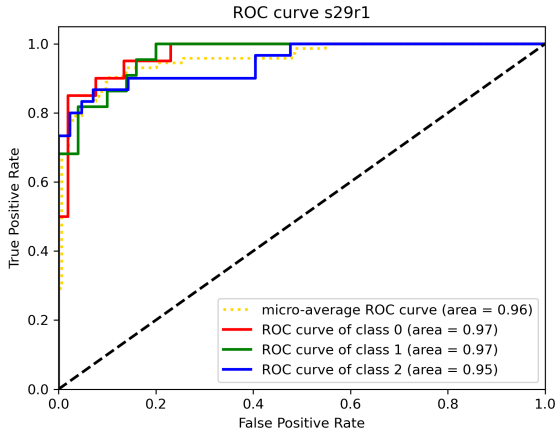

(c) Subject 29 session 01

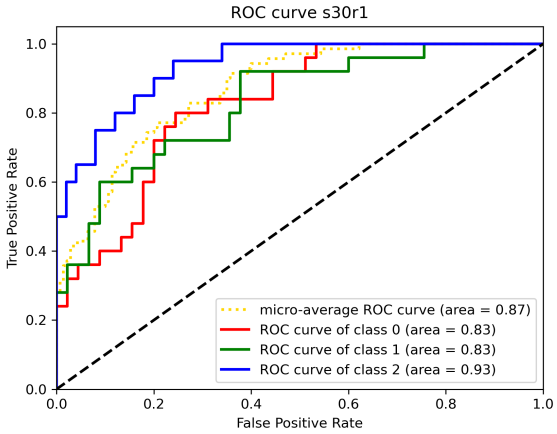

(d) Subject 30 session 01

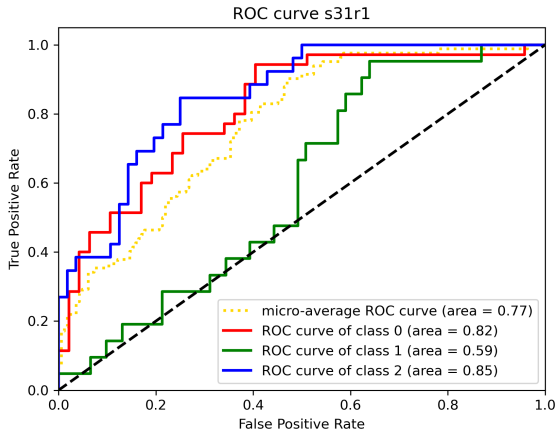

(e) Subject 31 session 01

Figure B.22: ROC curves for subjects 26, 28, 29, 30 and 31.

Appendix C

Paper

Searching for unique neural descriptors of primary colours in EEG signals: a classification study

Sara L. Ludvigsen*, Emma H. Buøen *, Andres Soler, and Marta Molinas

Norwegian University of Science and Technology (NTNU)
Department of Engineering Cybernetics
{sarall, emmahb}@stud.ntnu.no, {andres.f.soler.guevara, marta.molinas}@ntnu.no

Abstract. Identifying unique descriptors for primary colours in EEG signals will open the way to Brain-Computer Interface systems that can control devices by exposure to primary colours. This study is aimed to identify such unique descriptors in visually-evoked potentials (VEPs) elicited in response to the exposure to primary colours (RGB: red, green, and blue) from 31 subjects. For that, we first created a classification model with integrated transfer learning that can be suitable for an online setting. The obtained average accuracy of the final model over 23 subjects was 74,48% for the RGB colours, with 14 subjects above the average level and the maximum accuracy of 93,42%. When cross-session transfer learning was evaluated, 71% of the subjects tested showed an average variation of 5.0% in the accuracy comparing with the source set.

Keywords: RGB colours · Riemannian classifier · Transfer learning

1 Introduction

Electroencephalography (EEG) signals are obtained from electrodes placed on the scalp recording the macroscopic neural activity. It is a non-intrusive method for recording brain signals, and in BCI systems it can be used by individuals with extreme motor disabilities to manipulate their surroundings. Colour recognition is a novel approach in this area, but has the advantage of being easily applied to control the surroundings. A smart home using colour cues to turn on and off light, open doors, etc. is an example of how to provide more freedom for individuals in their everyday life.
Previous attempts have been made for RGB colour recognition. In [4], the authors identified the EEG signatures produced by the visual exposure to RGB colours. They observed that the difference in frequency response is a good classification signature. In [10] the intrinsic mode functions (IMFs) for Empirical mode decomposition (EMD) were used to identify features in the brain signals that describe the colour activity. The IMFs were used as input to classifiers such as Random Forest and Naive Bayes. Convolutional Neural Networks (CNNs) were

* Equal contribution

also tried, but not with IMFs as input. Colour vs. none-colour was classified with an accuracy of up to 99% using EMD. The maximum accuracy obtained classifying between RGB colours was 63%, and the maximum average accuracy of 46% using CNNs. A similar attempt was conducted in [9] characterising the signals using discrete wavelet transform and EMD separately. The goal was to classify idle state versus colour exposure. Support vector machine and random forest were used as classifiers. The most consistent result was obtained using EMD-based features, classifying with an 92.3% accuracy. Another experiment was presented in [5], where a headband with 4 EEG dry electrodes (AF7, AF8, TP9, TP10) was used on eight subjects. The EEG signals were transformed using Morlet transformation and forward feature selection. It achieved an average accuracy of 72,0%, and the highest accuracy of 80,6% when classifying between the RGB colours with a random forest classifier.
The scope of this work is to present a method that can be used in an online setting. The focus was therefore to find a methodology that is both fast and accurate in classifying among the RGB colours. EMD and Independent Component Analysis are time consuming operations, and were therefore not evaluated. The decision to use a Morlet wavelet to transform the data was made based on the analysis in Section 2.4. This technique was found advantageous to extract the peaks of several frequencies in the range 2-23 Hz as features. Recording EEG data requires expertise and time. If transfer learning is successful, it allows the reuse of data from previous recordings. Transfer learning across sessions was tested, it was done based on the Riemannian geometry classifiers that have been found suitable for transfer learning [6].

2 Materials and Methods

2.1 Data recording and protocol

The data used in this paper was recorded at the Aalto NeuroImaging facility at Aalto University (Finland). It was recorded using wet EEG electrodes in a high-end 3-layered magnetically shielded room. MEG measurements were recorded simultaneously, but not used in the results presented in this work. 64 electrodes were located on the head, four of which were EOG channels. Two of the EOG channels were placed on the front part of the head, one bipolar EOG channel was placed on the forehead, and below the left eye. The rest of the 60 channels were EEG channels located across the scalp. The placement was done using the international 10/10 system using a 64-channel cap from ANTNeuro, in `https://www.ant-neuro.com/products/waveguard/electrode-layouts` the 64 channel cap layout can be found.
For all electrodes, the impedance was kept below 5k Ohm before recording. The subjects were placed in front of a screen that altered between presenting a RGB colour and a grey screen. The RGB colours were presented in a randomised order for 1.3 seconds each, and the grey screen was presented in a varying length of time to prevent adaptation of the brain. For each subject, at least 140 epochs of each colour were recorded. The subject also had three breaks during the recording,

lasting one minute each. All the colours were presented in full-screen mode, and only during grey colour was a cross presented in the middle to keep the eyes of the subjects focused in the same area. Additionally, the subjects were asked to avoid blinking in the colours and try to blink only during grey.

2.2 Dataset

In total, 31 subjects were recorded. For the first recording of subjects 1-18 and subject 26, two of the occipital channels, Oz and O2, were flat. Therefore a second session with all the channels registering was recorded for these participants. The second session was no later than a week after the first session. The remaining 12 subjects participated only in one session. The following requirements were defined to include the subject in the dataset for classification.

1. None of the channels placed over the visual cortex is flat.
2. The subject had a correct behaviour during recording (e.g. looked at the screen, and kept its eyes open)
3. After pre-processing the data (see section 2.3), and removing bad epochs, at least 60 epochs of each colour remains.

This resulted in the dataset consisting of 23 subjects in Table 1.

2.3 Data pre-processing

The data was filtered between 0.1 - 40Hz using a band-pass filter, the baseline for each epoch was chosen to be from -100 to 0ms before stimuli were presented, and the data was re-referenced to the common average over all channels. All epochs containing a signal with an amplitude larger than 120μV in the EEG channels and 150μV in the EOG channels were rejected as bad epochs in order to remove artifacts such as blinks and muscular movement from the dataset. Additionally, the subjects were manually inspected for bad channels that were removed if found. The absolute value of the sample with the lowest value in an epoch was added to all samples in the epoch in order to shift the epoch above zero. If the lowest value was positive, it was subtracted from all samples in the epoch. As a final part of the pre-processing, the epochs were cropped to only contain the data between 50 and 450 ms after stimuli for feature extraction. All parameters used in pre-processing are listed in Table 2

2.4 Analysis of Visual Evoked Potentials

The Visual Evoked Potentials (VEP) were extracted and visually inspected for each participant before shifting the epoch above zero. An example of a VEP is shown in fig. 1 where the plots correspond to the VEP of red colour from subject 2 session 2. Figure 1a shows the evoked response of all channels with corresponding topological-plots for the peaks at 82, 122, and 212ms. It can be seen that there are positive peaks in the nearest channels to the visual cortex, as well as negative

Table 1: The dataset used in this project

Subject	Session	Red epochs	Green epochs	Blue epochs
02	2	134	135	135
03	2	129	124	120
05	2	83	81	82
06	2	134	137	133
07	2	108	110	102
08	2	119	116	115
11	2	122	127	123
13	2	132	129	131
14	2	128	126	126
15	2	103	108	101
16	2	118	126	129
18	2	140	139	139
19	1	114	96	94
20	1	135	137	136
21	1	76	66	69
23	1	125	125	120
24	1	106	113	106
25	1	116	104	108
26	2	120	119	127
28	1	136	136	133
29	1	120	121	117
30	1	117	118	115
31	1	139	135	133

peaks in the frontal channels. The strongest peaks were found in the channels at the occipital and parietal regions. This strong activation in those regions was seen for most colours in most subjects. It was, therefore, decided to only use channels P7, PO7, O1, POz, Oz, PO8, P8, and O2 when classifying. Figure 1b presents the VEPs of channel Oz of red colour. The black line represents the evoked of all red epochs, and the image above is the power plot of the activity evoked by red stimuli. There is an identifiable trend for the first 300ms of the signals, where the peaks were found consistent throughout all epochs. These time ranges where the peaks are presented, were selected as the time region of interest for extracting features for classification. The features were extracted by transforming the EEG data with a Morlet wavelet of several frequencies, which is further explained in Section 2.5.

2.5 Feature Extraction

Only eight channels were used for feature extraction and classification. The channels are listed in Table 2. The preprocessed data in each channel was decomposed using a continuous wavelet transform (CWT) with a 0.5 cycles Morlet wavelet as the mother wavelet. The correlation between the signal and wavelet was cal-

Table 2: Parameters

Filter	0.1 - 40 Hz
Reject criteria	EEG: 120e-6, EOG: 150e-6
Baseline	-0.1 - 0.0 sec
Crop	0.05 - 0.45 sec
Channels	P7, PO7, O1, POz, Oz, PO8, P8, O2
Frequencies (Hz) used in CWT	2,5,8,11,14,17,20,23
Number of cyclet in morlet wavelet	0.5

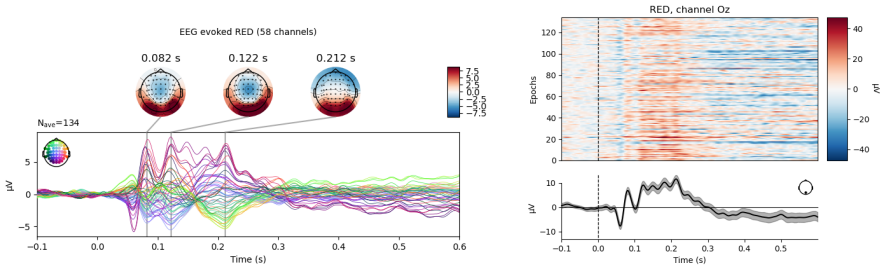

(a) Butterfly plot of the VEPs of red epochs for all channels

(b) VEPs of red epochs on channel Oz

Fig. 1: VEPs of subject 2 session 2

culated as follows.

$$CWT(a,b) = \frac{1}{|a|^{1/2}} \int_{-\infty}^{\infty} x(t)\psi(\frac{t-b}{a})dt \tag{1}$$

The decomposition was done using a built-in function in the MNE python library [7]. This function calculates the Morlet wavelet as follows.

$$\text{oscillation} = \exp(2j\pi ft) \tag{2} \qquad \text{gaussian envelope} = \exp(-t^2/(2\sigma^2)) \tag{3}$$

$$w(t,f) = \text{oscillation} * \text{gaussian envelope} \tag{4}$$

With the normalisation factor given by

$$A = (\sqrt{0.5}\|w\|)^{\frac{-1}{2}} \tag{5}$$

$$w(t,f) = A\exp(2j\pi ft)\exp(-t^2/(2\sigma^2)) \tag{6}$$

The frequencies used are specified in table 2. Each frequency decomposition in each channel was used as an input for a covariance matrix. Resulting in a 64x64 matrix (eq. (9)). Where the covariance is defined as

$$Cov(X,Y) = E[(X - E[X])(Y - E[Y])] \tag{7} \qquad E[X] = \int_{-\infty}^{\infty} xf(x) \tag{8}$$

$$\mathbf{CVM} = \begin{bmatrix} Cov((ch_1, 2Hz), (ch_1, 2Hz)) & \dots & Cov((ch_1, 2Hz), (ch_8, 23Hz)) \\ Cov((ch_1, 5Hz), (ch_1, 2Hz)) & \dots & Cov((ch_1, 5Hz), (ch_8, 23Hz)) \\ \vdots & \ddots & \vdots \\ Cov((ch_2, 2Hz), (ch_1, 2Hz)) & \dots & Cov((ch_2, 2Hz), (ch_8, 23Hz)) \\ Cov((ch_2, 5Hz), (ch_1, 2Hz)) & \dots & Cov((ch_2, 5Hz), (ch_8, 23Hz)) \\ \vdots & \ddots & \vdots \\ Cov((ch_8, 23Hz), (ch_1, 2Hz)) & \dots & Cov((ch_8, 23Hz), (ch_8, 23Hz)) \end{bmatrix} \tag{9}$$

2.6 Classification

The Minimum Distance to Mean with geodesic filtering (FgMDM) Riemannian classifier [3] was used, due to its robustness to noise [2] and its generalisation capabilities [6].
In [6], the Riemannian distance (δ_G) was defined as the length of the geodesic between two symmetric positive definite matrices, $\mathbf{C}_1$ and $\mathbf{C}_2$, on a Riemannian manifold:

$$\delta_G(\mathbf{C}_1, \mathbf{C}_2) = \left\| \text{Log}(\mathbf{C}_1^{-1/2} \mathbf{C}_2 \mathbf{C}_1^{-1/2}) \right\|_F \tag{10}$$

where $\text{Log}(\cdot)$ is the matrix logarithm. The Riemannian distance is invariant under congruence and invariant under inversion, which means that

$$\delta_G(\mathbf{X}\mathbf{C}_1\mathbf{X}^T, \mathbf{X}\mathbf{C}_2\mathbf{X}^T) = \delta_G(\mathbf{C}_1, \mathbf{C}_2) = \delta_G(\mathbf{C}_1^{-1}, \mathbf{C}_2^{-1}) \tag{11}$$

All the accuracy values presented were calculated by using 10-Fold cross-validation, where 90% of the dataset was used for training, and 10% for testing.

2.7 Transfer Learning

A challenge in BCI systems is to accurately classify one session data based on data from another session. This is due to the changes in impedance and electrode positioning is likely to vary each time the subject participates in a session.
The EEG signal, $\mathbf{x}(t)$, can be written as a linear combination of the sources of the signal, $\mathbf{s}(t)$:

$$\mathbf{x}(t) = \mathbf{A}\mathbf{s}(t), \tag{12}$$

where $\mathbf{A}$ is the mixing matrix [6]. The mixing matrix $\mathbf{A}$ is dependent upon the impedance and electrode placement. Let the covariance matrices $\mathbf{C}_i = \mathbf{A}\mathbf{S}_i\mathbf{A}^T$ and $\mathbf{C}_j = \mathbf{A}\mathbf{S}_j\mathbf{A}^T$ be representing class i and j, taken from the same session and subject. Let $\mathbf{Q}_i = \tilde{\mathbf{A}}\mathbf{S}_i\tilde{\mathbf{A}}^T$ and $\mathbf{Q}_j = \tilde{\mathbf{A}}\mathbf{S}_j\tilde{\mathbf{A}}^T$ be the covariance matrices taken from another session, with the same subject. Note that $\mathbf{A} \neq \tilde{\mathbf{A}}^T$, because the impedance level and electrode placement varies from session to session. These changes cause a shift in the EEG recording, which makes transfer learning difficult. Due to the congruence invariance property of the Riemannian distance

between a pair of symmetric positive definite matrices, the distance between the covariance matrices in the source space are equal for both sessions, as shown in[6]:

$$\delta_G(\mathbf{C}_i, \mathbf{C}_j) = \delta_G(\mathbf{Q}_i, \mathbf{Q}_j) \tag{13}$$

The methods described in this section were implemented and tested in python by using `pyriemann`[1], `scikit-learn`[8] and `mne`[7] libraries.

3 Results

The accuracy of the classification in the results is described as a number between 0 and 1, with 1 as the highest accuracy. The standard deviation of the accuracy is included as "std" in the tables. All results were obtained when classifying between the three classes {Red, Green and Blue}.

3.1 RGB classification

The RGB classification results are presented in table 3, where the results correspond to the subjects in table 1 that fulfilled all the criteria set section 2.2. The average obtained across participants was 74,48% with a standard deviation of 7,5%, where more than 60% of the subjects obtained an accuracy value over the average. Where subject 14 obtained the highest accuracy of 93,42% and subject 31 the lowest with 54,02%. All the subjects obtained scores over the chance level. In addition, table 4 shows the classification accuracy of all subjects with two sessions, where the channels Oz and O2 are excluded, as these channels were flat in session 1 for all subjects. The subjects still had to fulfill criteria 2) and 3) explained in section 2.2.

3.2 Cross-session transfer learning

Cross session transfer learning was evaluated for all subjects in table 4 where both sessions had an accuracy above 60%. The subjects and results for transfer learning are presented in table 5. Average accuracy was computed considering both sessions for the subject in table 4, and the same procedure was done for standard deviation. The column marked "s1 - s2" represents the accuracy obtained when session 1 is used for training, and session 2 is used for testing. Vice versa for the column marked "s2 - s1". "diff" is the difference between the average accuracy of both sessions, and the best performance for transfer learning.

4 Discussion and Conclusion

The results obtained show that using the correlation of the wavelet decomposition with the FgMDM Riemannian classifier for the VEP allowed to separate the colours in most of the subjects. All subjects scored above the chance level 33%, with the accuracy of the lowest performing subject at 54.04%. The average

Table 3: Result of RGB classification of subjects that fulfil all criteria.

Subject	FgMDM	std
s14r2	0,9342	0,056747
s02r2	0,9255	0,050247
s13r2	0,9208	0,021501
s21r1	0,8959	0,05084
s06r2	0,8515	0,050616
s29r1	0,8294	0,065617
s30r1	0,8158	0,0963
s26r2	0,8023	0,088092
s07r2	0,7813	0,108253
s19r1	0,7632	0,050098
s24r1	0,7564	0,085264
s11r2	0,7550	0,092997
s18r2	0,7512	0,09483
s23r1	0,7459	0,109585
s05r2	0,7318	0,084454
s20r1	0,7104	0,077408
s25r1	0,6705	0,110448
s08r2	0,6514	0,064902
s03r2	0,6351	0,07554
s28r1	0,5754	0,067562
s15r2	0,5451	0,096332
s16r2	0,5410	0,065429
s31r1	0,5404	0,061623
Average	**0,7448**	**0,0750**

Table 4: Results of RGB classification of all subjects with two sessions. Not including channel Oz and O2.

Subject	FgMDM	std
s02r1	0,8417	0,0493
s02r2	0,8142	0,0213
s03r1	0,5647	0,0561
s03r2	0,5526	0,0976
s04r1	0,5139	0,0780
s06r1	0,7625	0,0740
s06r2	0,7398	0,0489
s07r1	0,6493	0,1020
s07r2	0,7156	0,0963
s08r1	0,5471	0,0546
s08r2	0,6400	0,0769
s11r1	0,5857	0,0528
s11r2	0,6447	0,0987
s13r1	0,8188	0,0714
s13r2	0,8722	0,0680
s14r1	0,7125	0,0731
s14r2	0,7289	0,1085
s15r1	0,4232	0,0569
s15r2	0,5030	0,0626
s16r1	0,5209	0,0926
s16r2	0,4925	0,0786
s18r1	0,6379	0,0485
s18r2	0,7154	0,0713
s26r1	0,6439	0,0681
s26r2	0,6203	0,0487

accuracy of 74.48%, which is significantly above the chance level. It clearly states that the features presented can be used to separate the responses of the RGB colours. By analysing the accuracy we can identify that from the subjects that scored at approximately 55%[1], the classifier might have been able to recognise at least *one* of the colours, and was guessing between the three classes on the remaining epochs. Similarly, the subjects that scored at approximately 77%[2], the classifier might have been able to recognise *two* of the colours, and guessing at the remaining 33% of the epochs.

The transfer learning test showed that the cross-session model can be used for classifying a different session. Five out of seven subjects obtained a difference lower than 7% when comparing training and testing between sessions with the use of the same session for training and testing. Even with the limited number of subjects with two sessions, we consider that the model is not guessing when

[1] Accuracy $= 33\% + \frac{1}{3}66\% = 55\%$
[2] Accuracy $= 66\% + \frac{1}{3}33\% = 77\%$

Table 5: Results of cross-section transfer learning.

Subject	Avr. accuracy	Avr. std	s1 - s2	s2 - s1	diff.
02	0,8216	0,0471	0,8119	0,7825	0,0097
06	0,7487	0,0644	0,5571	0,5118	0,1916
07	0,6734	0,1010	0,6000	0,5138	0,0734
13	0,8416	0,0710	0,7679	0,7402	0,0737
14	0,7234	0,09825	0,6474	0,5843	0,0760
18	0,6765	0,0574	0,3373	0,4698	0,2067
26	0,6322	0,0605	0,6066	0,6108	0,0214

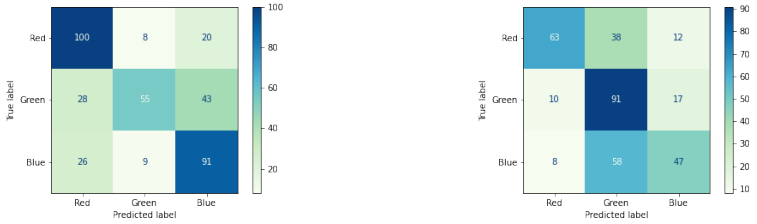

(a) Source = session 1, target = session 2. (b) Source = session 2, target = session 1.

Fig. 2: Session to session classifying for subject 14.

classifying a session based on the training on the other. We consider that this aspect should be explored with more subjects in future works. When looking at the confusion matrix in fig. 2a, it can be seen the classifier performed better at separating red and blue, while in fig. 2b the classifier performed better when separating green. If training on both session 1 and session 2, testing on a session 3 might actually increase performance. Hence, transfer learning using more sessions should be explored as well. It is especially interesting that not any modification of the signal is needed when using a Riemannian FgMDM classifier for testing across-session, making it very convenient for offline modelling and online testing. From the features presented in this paper, the FgMDM classifier does separate between colours using EEG electrodes in a BCI model. It should be easy enough to apply in an online setting, and it also shows promising for applying cross-session transfer learning.

The accuracy obtained when classifying RGB-colours in this paper are higher than the accuracy obtained in [10] and [5] with an average accuracy of 46% and 70,2% respectively. However, the equipment for recording this dataset used gel based electrodes and impedance was controlled, contrary to [10] and [5], where dry electrodes were used.

Bibliography

[1] Barachant, A., King, J.R.: pyriemann v0.2.2 (Jun 2015). https://doi.org/10.5281/zenodo.18982

[2] Barachant, A., Bonnet, S., Congedo, M., Jutten, C.: Riemannian geometry applied to bci classification. In: Vigneron, V., Zarzoso, V., Moreau, E., Gribonval, R., Vincent, E. (eds.) Latent Variable Analysis and Signal Separation. pp. 629–636. Springer Berlin Heidelberg, Berlin, Heidelberg (2010)

[3] Barachant, A., Bonnet, S., Congedo, M., Jutten, C.: Classification of covariance matrices using a riemannian-based kernel for bci applications. Neurocomputing **112**, 172 – 178 (2013). https://doi.org/https://doi.org/10.1016/j.neucom.2012.12.039, advances in artificial neural networks, machine learning, and computational intelligence

[4] Bjørge, L.E., Emaus, T.: Identification of EEG-based signature produced by visual exposure to the primary colours RGB. Ph.D. thesis, NTNU (07 2017)

[5] Chaudhary, M., Mukhopadhyay, S., Litoiu, M., Sergio, L., Adams, M.: Understanding brain dynamics for color perception using wearable eeg headband. Proceedings of 30th Annual International Conference on Computer Science and Software Engineering 2020 (08 2020)

[6] Congedo, M., Barachant, A., Bhatia, R.: Riemannian geometry for EEG-based brain-computer interfaces; a primer and a review. Brain-Computer Interfaces **4**(3), 155–174 (2017). https://doi.org/10.1080/2326263X.2017.1297192

[7] Gramfort, A., Luessi, M., Larson, E., Engemann, D.A., Strohmeier, D., Brodbeck, C., Goj, R., Jas, M., Brooks, T., Parkkonen, L., Hämäläinen, M.S.: MEG and EEG data analysis with MNE-Python. Frontiers in Neuroscience **7**(267), 1–13 (2013). https://doi.org/10.3389/fnins.2013.00267

[8] Pedregosa, F., Varoquaux, G., Gramfort, A., Michel, V., Thirion, B., Grisel, O., Blondel, M., Prettenhofer, P., Weiss, R., Dubourg, V., Vanderplas, J., Passos, A., Cournapeau, D., Brucher, M., Perrot, M., Duchesnay, E.: Scikit-learn: Machine learning in Python. Journal of Machine Learning Research **12**, 2825–2830 (2011)

[9] Torres-García, A., Moctezuma, L., Molinas, M.: Assessing the impact of idle state type on the identification of rgb color exposure for bci (02 2020). https://doi.org/10.5220/0008923101870194

[10] Åsly, S.: Supervised learning for classification of EEG signals evoked by visual exposure to RGB colors. Ph.D. thesis, NTNU (06 2019). https://doi.org/10.13140/RG.2.2.13412.12165

Emma H. Buøen & Sara L. Ludvigsen

The Augmented Human

NTNU

Norwegian University of
Science and Technology